MEASUREMENTS AND MODELING OF NON-PREMIXED TUBULAR FLAMES: STRUCTURE, EXTINCTION AND INSTABILITY

By

Shengteng Hu

Dissertation

Submitted to the Faculty of the

Graduate School of Vanderbilt University

in partial fulfillment of the requirements

for the degree of

DOCTOR OF PHILOSOPHY

in

Mechanical Engineering

December, 2007

Nashville, Tennessee

Approved:

Robert W. Pitz

Joseph A. Wehrmeyer

John W. Williamson

Deyu Li

Kenneth A. Debelak

To my beloved wife, Qingyang Shang, infinitely supportive

ACKNOWLEDGEMENTS

I am grateful to all of those who made this dissertation possible. First and foremost, I would like to express my sincere gratitude to my advisor, Dr. Pitz, for his guidance and help during this work. Appreciation is also expressed to other members of my dissertation committee, especially Dr. Joseph Wehrmeyer for his assistance with the experiments. Valuable help from fellow graduate students Dr. Zhongxian Cheng, Dr. Peiyong Wang, and Yu Wang is also highly appreciated. I would also like to thank the support from my wife Qingyang during this study.

Financial support of this work came from NASA (Grant No: NNC04AA14A with John Brooker as the technical monitor) and NSF (CTS-0314704).

TABLE OF CONTENTS

Page

LIST OF TABLES

LIST OF FIGURES

LIST OF SYMBOLS

a_P	Planck mean absorption coefficient
A	focal area of the laser beam
A_{21}	spontaneous emission rate constant
B_{12}	Einstein coefficient for absorption
c	speed of light
C_p	specific heat
$C_{T,i}$	calibration factor, function of both T and species i
d	characteristic length
D_h	hydraulic diameter
$D_{i,j}$	multi-component diffusion coefficient
D_i^T	thermal diffusion coefficient
D_I	Damköhler numbers of the first kind
D_{II}	Damköhler numbers of the second kind
E	activation energy
E_l	laser energy
f_1^0	ground-state population fraction
F	power of the fluorescence signal
Fr	Froude number

g	acceleration of gravity
G	camera gain in terms of counts per photon
h	Planck's constant
h_i	enthalpy per unit mass of species i
H	outer nozzle height
I_ν	incident laser irradiance per unit frequency interval
J	rotational quantum number; constant pressure eigenvalue
k	stretch rate; Boltzmann constant
K	interference factor
K_{Q_i}	quenching rate coefficient for species i
L	length of the sample volume; separation distance of the opposed jets
L_e	Lewis number
m	mass flux
n	total number density
n_i	number density of the i^{th} species
N_1^0	population at the ground state
P	pressure
Q	CCD camera quantum efficiency; heat release per unit mass of oxidizer consumed
Q_{21}	collisional quenching rate constant
$\sqrt{Q}$	normalized pressure eigenvalue

R	nozzle radius; universal gas constant
Re	Reynolds number
r	radial coordinate
R_s	location of the stagnation surface
S_L	laminar burning velocity
T	temperature
v	vibrational quantum number
U	axial velocity
U_{by}	buoyancy induced convection velocity
V	radial velocity
V_i'	diffusion velocity of species i
W	averaged molecular mass
W_j	molecular mass of the j^{th} species
X_i	mole fraction of species i
Y_i	mass fraction of species i
z	axial coordinate
Z	mixture fraction
α	thermal diffusivity, initial mixture strength
β	Zel'dovich number
ϕ	equivalence ratio

γ	specific heat ratio, incomplete gamma function
η	collection efficiency
λ	wavelength
μ	viscosity; reduced mass of the colliding species
ν	incident laser frequency
ν_i	Stokes frequency of the i^{th} species; stoichiometric coefficient of the i^{th} species
ρ	density
σ	Stefan-Boltzmann constant
σ_i	Raman cross section of the i^{th} species
σ_{Q_i}	quenching cross section of the i^{th} species
τ_{fl}	characteristic flow time
τ_{df}	characteristic diffusion time
τ_{ch}	characteristic chemical time
υ	kinematic viscosity
ϖ_i	mass reaction rate per unit volume of species i
Ω	solid angle of the collection optics
ξ_i	camera counts of species i
ψ	stream function

Subscript

cal	calibration flame

ext	extinction
1	inner nozzle
2	outer nozzle
∞	ambient condition
o , O	oxidizer stream
f , F	fuel stream; flame location

CHAPTER I

INTRODUCTION

Motivation

Non-premixed combustion is of great importance due to the wide practical applications such as diesel engines, gas turbines, and industrial furnaces. New areas of application continue to emerge, e.g. in direct-injection spark-ignition (DISI) engines, fuel and air enter the piston chamber without premixing. Both experimental and modeling research needs have only grown larger in recent years. In turbulent combustion modeling, the laminar flamelet model plays an important role (Peters 1984). The underlying concept is that the reaction zones of a flame are thin and the flow turbulence does not alter its structure from the corresponding laminar flames subjected to the same scalar dissipation. As a result, the turbulent flame can be modeled as an ensemble of laminar non-premixed flamelets. Pre-calculated libraries of quantities such as species composition, temperature and reaction rates as functions of mixture fraction and stoichiometric scalar dissipation rate using detailed chemical reaction mechanisms and molecular diffusion formulation are used in the description of the chemistry-turbulence interactions. Choosing mixture fraction and scalar dissipation as the independent variables is somewhat convenient but often times, not sufficient. The flamelets inside a turbulent flame are inevitably curved due to the influence of the turbulent eddies with various sizes. Strong variations of the scalar dissipation across the

flamelet, which are likely caused by the coupled effects of local flame curvature and molecular preferential diffusion, exist in turbulent flames (Bilger 2000). Therefore, studies on the interaction between flame curvature and chemical reaction are needed in addition to the flow and chemistry interaction.

On the other hand, local curvature coupled with preferential diffusion may also lead to local extinction and re-ignition that are also important in both turbulent combustion modeling and fire safety. Although evidences of the effects of curvature on flame extinction have been reported (Takagi et al. 1996b; Finke and Grünefeld 2000), the previous experimental work suffers from the fact that the curvature across the flame under investigation was not constant, which makes the data interpretation ambiguous. An opposed tubular burner can overcome this difficulty by producing a flame with uniform curvature. A recent study (Hu et al. 2006a; Wang et al. 2006a) showed that the flame surface of the non-premixed tubular flame started to develop cellular structures at the highly-stretched, near-extinction conditions for fuels with non-unity Lewis number (Lewis number is defined as the ratio of the overall thermal diffusivity and the molecular diffusivity of the mixture), which can be attributed to the combined effects of curvature and Lewis number. This kind of flame instability is closely related to the extinction and re-ignition in turbulent flames and is worth further investigation.

It is well recognized that many important combustion phenomena are kinetically controlled. Reduction of engine development costs, improved predictions of the environmental impact of combustion processes, as well as the improved assessment of any

industrial process making use of chemical kinetics, are only possible with accurate chemical kinetics modeling. One step toward gaining a better understanding of these issues is to improve the accuracy of detailed chemical mechanisms. There is constant interest in the development of detailed chemical reaction mechanisms. Simultaneous parameter optimization targeting experimental data (Smith et al. 2000) is often the standard procedure of obtaining a detailed chemical mechanism when the rate constant for each individual reaction is not readily available from the literature. The need for a wide variety of experimental data is important. Previously, no experiments on opposed tubular, non-premixed flames have been conducted. This omission is part of the motivation that triggered the research carried out herein. Detailed, accurate measurement of major species concentration and temperature of the non-premixed tubular flames with good spatial resolution would provide a valuable set of data in optimizing the reaction mechanisms.

The objectives of this research are: 1) to conduct Raman scattering and laser-induced fluorescence measurements of temperature and major species concentrations for opposed tubular flames using hydrogen, methane and propane fuels, 2) to compare the measured flame structure to simulation results with detailed chemistry and complex molecular transport models, and 3) to investigate the extinction and instability characteristics of non-premixed tubular flames with different Lewis numbers generated by various fuels and diluents. The role of curvature in laminar, non-premixed flames is the main focus throughout the study. This work can be beneficial to the understanding of curvature effects in turbulent modeling, contribute to the overall research in detailed chemical reaction

mechanisms, and improve our knowledge on extinction and stability of non-premixed flames.

Background

In turbulent flame modeling, the laminar flamelet model has been popular among many researchers due to its simplicity. The first systematic description was provided by (Peters 1984), where the scalar dissipation was introduced as an independent variable to include the coupled effects of non-equilibrium and turbulence in non-premixed flames, which are not treated in the classical conserved scalar approach. The turbulent flame is modeled as an ensemble of laminar non-premixed flamelets, which are represented by pre-calculated libraries of quantities such as species composition, temperature and reaction rates as functions of mixture fraction and stoichiometric scalar dissipation rate using detailed chemical reaction mechanisms and molecular diffusion formulation. A probabilistic description of the occurrence of such structures is assumed in the model. Many contributions have been made during the course of its maturity, which include the effects of radiative heat transfer (Marracino and Lentini 1997; Coelho et al. 2003), differential diffusion (Pitsch and Peters 1998), extinction and reignition (Pitsch et al. 2003) and scalar dissipation rate fluctuation (Wang and Chen 2005). The flamelet approach has been applied to turbulent jet diffusion flames (Haworth et al. 1988; Sanders and Lamers 1994; Pitsch 2000; Coelho and Peters 2001), modeling of NO (Heyl and Bockhorn 2001) and soot (Pitsch et al. 2000) formation, as well as more practical combustion devices like a gas turbine

(Riesmeier et al. 2004) and DI diesel engines (Hasse and Peters 2005; Kim et al. 2006).

Flamelet libraries are often times pre-calculated using laminar opposed-jet flame as the model flame, e.g. (Sanders et al. 2000), where the use of mixture fraction and stoichiometric scalar dissipation rate as the independent variable may be somewhat justified because of the planar nature of the flame surface. However, in practical turbulent flames, the flame surfaces are almost exclusively curved due to the influence of the turbulent eddies with various sizes, which questions the use of a planar flame model. Strong variations of the scalar dissipation across the flamelet, which are likely caused by the coupled effects of local flame curvature and molecular preferential diffusion, exist in turbulent flames (Bilger 2000). Most recently, the influence of curvature on autoignition was studied in a corrugated counter flow mixing field using n-heptane versus air (Kortschik et al. 2005). LIF images indicated that elevated concentrations of formaldehyde concave toward the air side were in favor of autoignition, which is also confirmed by the numerical calculations. Based on the experimental findings, the authors derived an explicit flamelet formulation to account for molecular transport normal to the direction of the mixture fraction gradient, which is identified as the curvature effects.

Despite the evidence that curvature effects in turbulent combustion should not be neglected (Hilbert et al. 2004), studies of such effects on other aspects of a non-premixed flame, e.g. the interaction between flame curvature and chemical reaction, flame structure, flame extinction and instability, remain very limited. Contributions in this area are needed to aid the overall combustion research.

Flame Structure

How the real elementary chemistry affects the flame structure has been the main focus of laminar flame research for three decades (Williams 2000). Extensive experimental, theoretical and numerical studies have been devoted to this area. Since the inception of the Burke-Schumann flame sheet model (Glassman 1996), considerable theoretical work has been done toward better understanding the structure and extinction of the diffusion flames. In (Liñán 1974)'s benchmark study on the model problem of opposed-jet combustion using large activation energy asymptotics, the characteristic S curve was demonstrated for maximum temperature plotted in terms of Damköhler number (ratio of the characteristic flow time to the chemical time). From the curve, four regimes were identified, namely nearly frozen ignition regime, partial burning regime, premixed flame regime and near-equilibrium diffusion controlled regime. The large activation energy asymptotic analysis was expanded to study the diffusion flame structure with general Lewis numbers (Law and Chung 1982), where effective freestream concentrations were defined. According to the analysis, the system effectively experiences a reduction (increase) in the freestream concentration of the corresponding reactant and therefore lower (higher) flame temperature if $L_e > 1$ ($L_e < 1$). In a later effort (Cuenot and Poinsot 1996), asymptotic solutions for the temperature, mass fractions and velocity profiles as functions of the passive scalar and scalar dissipation rate were derived for both the infinitely fast chemistry and finite rate chemistry cases considering variable Lewis numbers. The Lewis effects were

essentially incorporated in the definition of the passive scalar.

In terms of experimental study, measurement of the velocity, temperature and species concentrations presents more detailed information of the flames, and therefore helps to identify the key features. Another important aspect of structural study of flames is to facilitate the development of detailed chemical reaction mechanisms, the benefit of which is twofold. On one hand, it serves as a member of the targeting experimental data for optimizing the mechanisms (Smith et al. 2000); on the other hand, it can also be used to test the validity of an existing mechanism (Trees et al. 1995).

Before the emergence of laser based techniques, thermocouples were widely used to measure temperature in flames, and the sampling probe method has been the main technique for species concentration measurement in flames. They are still very useful for flames with heavy hydrocarbon molecules or in large systems like engines, furnaces, etc. (Fristrom and Westenberg 1965)

In an early structural study of non-premixed flames (Tsuji and Yamaoka 1969), major species concentrations were measured for propane/methane-air flames using a sampling probe with gas chromatography in the forward stagnation region of a porous cylinder. A substantial amount of oxygen leakage was diagnosed on the fuel side of the flame for various fuel injection rates and stagnation velocity gradients. Temperature and velocity profiles were also obtained with a thermocouple and the particle tracking technique. Using a one-dimensional assumption, they correlated the measured scalar profiles to heat-release rate and reaction rate of individual species (Tsuji and Yamaoka 1971). A small valley on

the fuel side of the heat-release-rate profile was attributed to fuel pyrolysis effects. The observation of such a phenomenon is only possible with structural studies. The experimental data were used later on in a collaborative effort to test the validity of the similarity simplification of the problem as well as the different theoretical solution techniques (Dixon-Lewis et al. 1984). Generally good agreement had been reached between the experimental data and the simulation results.

Structural studies of laminar two-dimensional methane/air non-premixed flames on a Wolfhard-Parker slot burner (Figure 1) were conducted using sampling probe (major species), laser absorption (OH and CO), laser-induced fluorescence (O and CH), multiphoton ionization (H and CH_3) and thermocouple (T) techniques (Norton et al. 1993), where attention was drawn on radical species as well as major stable species. Comparison with the numerical simulation of an axisymmetric coflow flame (Smooke et al. 1990) was carried out in the mixture fraction frame with matching scalar dissipation rate, where care in defining the mixture fraction and scalar dissipation rate has been taken to legitimize such a cross comparison. Good agreement was found for the major radical species OH, H and O, while for the hydrocarbon radicals CH and CH_3 some disagreement was observed.

Despite the ability to monitor relatively large amount of species at one time, the sampling probe technique generally possesses large uncertainties (>10%), and disturbs the flow and combustion process. As a result, the usage of this technique in the study of flame structure sees only very limited application. On the other hand, due to its non-intrusive nature and high accuracy, more and more studies using laser based diagnostic techniques

see more and more applications in flame studies.

In a recent study (Smooke et al. 1990), two-dimensional images of major species and temperature of a laminar, axisymmetric, methane-air diffusion flame in an unconfined coflow burner were obtained using the spontaneous Raman spectroscopy technique. Comparison between the experimental data and numerical calculation using a C_2 mechanism demonstrated qualitatively good agreement. The importance of the bleaching effects of the H radical by hydrocarbon species was very well revealed, and the OH and CO_2 concentration were therefore found to peak only after the disappearance of methane.

In the one-dimensional, non-premixed flame category, laminar opposed-jet planar flames subject to flame stretch due to aerodynamic straining are widely used to study flame chemistry due to its relative ease in configuration. They are also used to provide the basic elements in the flamelet library. A schematic of the burner is shown in Figure 2, where fuel and oxidizer from the opposing nozzles meet and formed a stagnation plane. Laser-based measurements of the flame have been reported previously, and these studies generally compare their experimental findings with numerical simulations using detailed reaction mechanisms and transport data. Studies on hydrogen/nitrogen-air opposed-jet flame were conducted previously (Trees et al. 1995; Brown et al. 1997), where UV Raman scattering was used in the measurement. Measurements of the major species concentration (H_2, O_2, H_2O and N_2) were made at two conditions, one close to and the other far from extinction. The experimental data effectively validated the numerical model and the

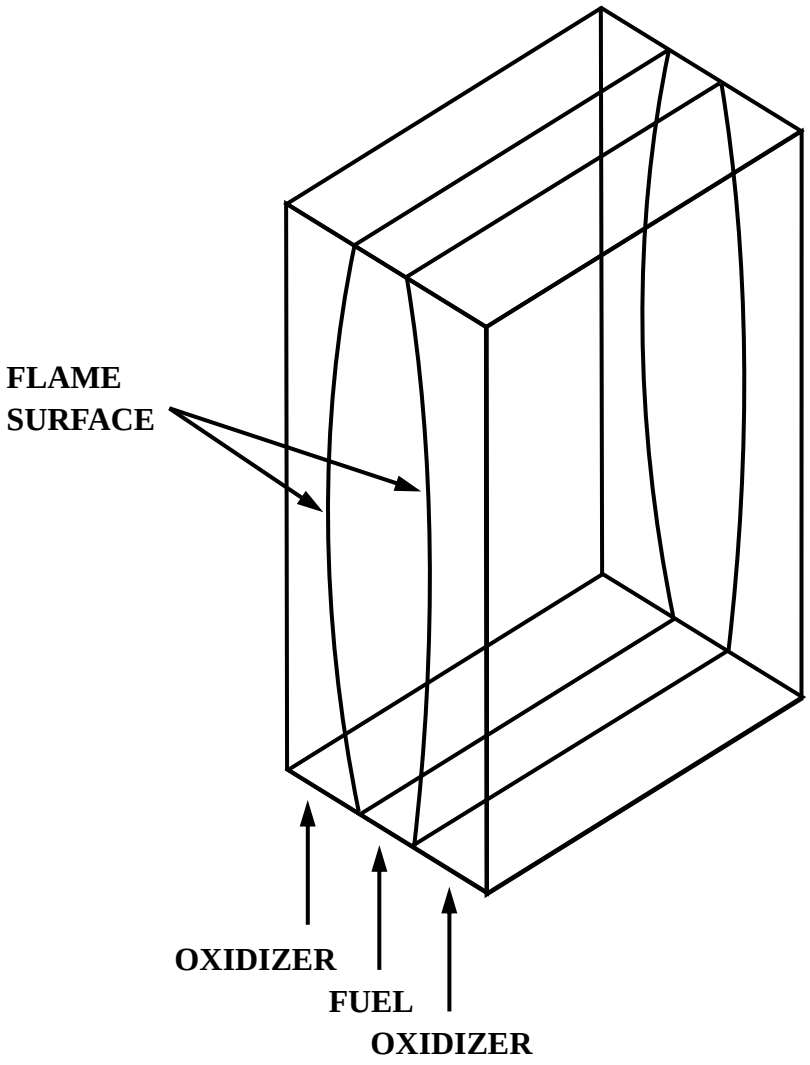

Figure 1 Schematic diagram of the Wolfhard-Parker slot burner

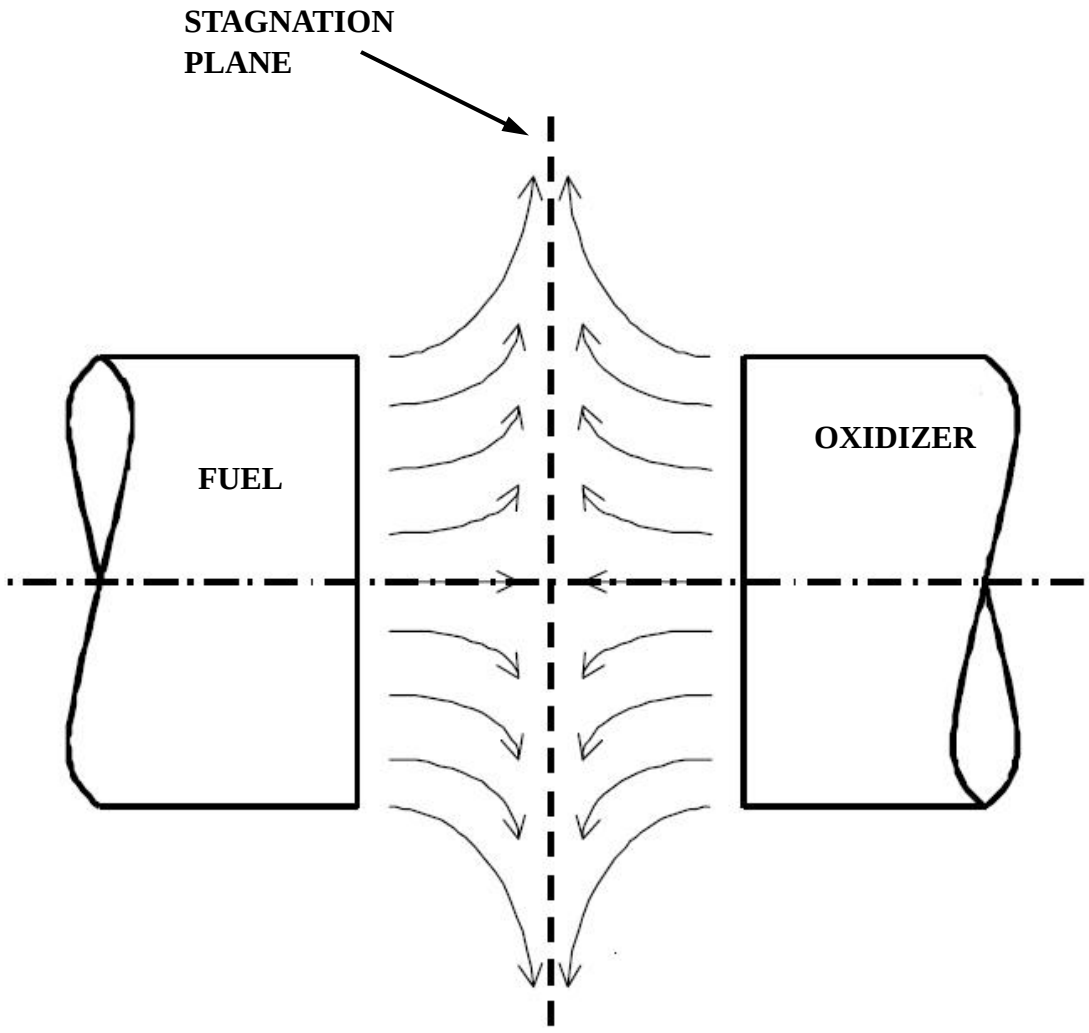

Figure 2 Schematic of the opposed-jet burner

detailed chemical kinetics mechanism employed through the good agreement achieved between them. The hydrogen opposed-jet flame was also examined by (Wehrmeyer et al. 1996) with a focus on the differential diffusion effects. Various fuel dilutions and various strain rates were studied to demonstrate this effect.

Similar effort using visible Raman scattering was carried out on methane (Sung et al. 1995) flames in the opposed-jet burner. After validation of the numerical model and reaction mechanisms, the authors then used the computational tool to examine the structural response of diffusion flames to strain rate variations. According to their findings, diffusion flame thickness scales inversely with the square root of strain rate, while deviation from this scaling was found at the near-extinction conditions. A secondary heat-release peak on the oxidizer side was found in methane-air flames and the key reaction responsible for it was identified. Special focus was put on the endothermic heat absorption on the oxidizer side. It was found that the small dent on the heat-release profile (Tsuji and Yamaoka 1971) can be suppressed by increasing the stoichiometric mixture fraction of the system, and the mechanism leading to this was also discussed.

The opposed-jet configurations eliminate the effects of flame curvature, thereby reducing the effects of nonunity Lewis number. Such studies were focused mainly on the Damköhler number effects. To study the curvature effects, the toroidal vortices formed outside a hydrogen-air jet diffusion flame surface were investigated numerically with detailed chemistry and transport data (Katta et al. 1994; Katta and Roquemore 1995). Nonunity Lewis number was found to be responsible for the increased (decreased) flame

temperature in the bulging (squeezing) section of the flame. The flame curvature was argued to be partially responsible for the effect on flame temperature when coupled with the preferential diffusion effects. The vortex-induced stretching/compressing effect was further investigated in another study (Katta and Roquemore 1995). By introducing the vortices from either the fuel or the air side, hydrogen-air diffusion flames with opposite stretching effects were formed. The flame temperature was found to increase when flame was compressed by the air-side vortex or stretched by the fuel-side vortex. It was pointed out that curvature coupled with preferential diffusion was accountable for this phenomenon.

Although studies on the jet diffusion flame offers insights into the effects of non-uniform flow field and flame curvature, which in turn amplify the effects of nonunity Lewis number, it is difficult to isolate each of them. Detailed structural measurement from the experimental point of view has also been shown to be difficult due to the intrinsic oscillation induced by buoyancy. Although the important features of the non-premixed flames related to flame stretch can be very well investigated using the opposed-jet burner, it inevitably lacks the capability of studying curvature-related flame phenomena. Opposed tubular flames can overcome all the above difficulties without losing the simplicity of the flow. A schematic of the burner is shown in Figure 3. The important features of the opposed tubular burner can be summarized as: 1) Curvature is de-coupled from flame stretch in the sense that their directions are orthogonal to each other. 2) Curvature throughout the flame front is uniform because the diameter of the flame tube is constant at a given condition. 3)

The flow field is simple and all quantities can be described as functions of radial location only, which is preferred by both experimentalists and modelers. 4) Both concave and convex curvature can be easily established under well-controlled conditions. Such flames deserve more attention and are the main focus of this study.

Extinction

Flame extinction is important for both turbulent combustion (Williams 2000) and fire safety (Williams 1981). Based on the mechanism, extinction of non-premixed flame can be roughly categorized into four different types (Williams 2000). Due to increase of the velocity gradient at the vicinity of the flame surface, the residence time of the reactants is decreased and extinction in this manner can be called *extinction by strain*. In non-premixed combustion, excessive dilution of one of the reactants can increase the chemical reaction time and ultimately lead to extinction, which can be called *extinction by dilution*. In some cases, where the flame surface is pushed very close to a non-adiabatic wall, heat loss starts to prevail and flame temperature decreases. As a consequence, the chemical reaction time decreases and eventually leads to extinction, which can be called *extinction by convective heat transfer*. Under certain conditions, e.g. opposed-jet flame at low strain rate and with the absence of buoyancy, the flame thickness becomes large, and radiative heat loss from the large high temperature zone starts to dominate. Similar to that of the convective heat losses, the decrease in flame temperature reduces the chemical reaction time and produces *extinction by radiation*. The review here is focused on the first two types of extinction.

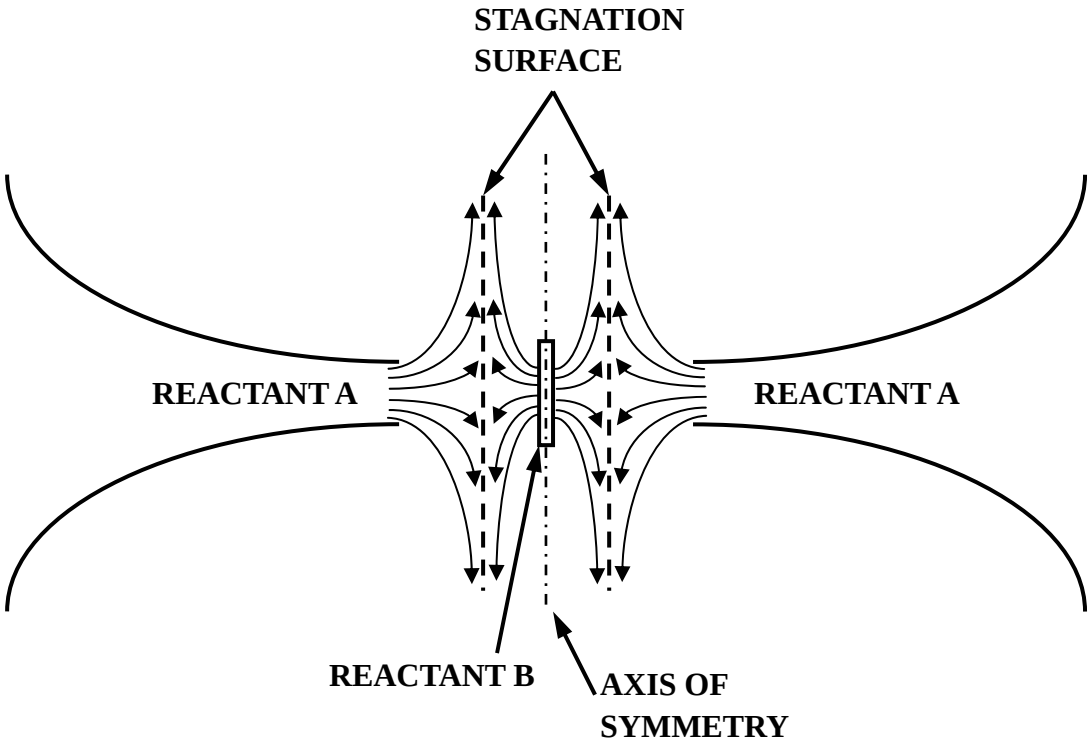

Figure 3 Schematic of the opposed tubular burner

The counterflow diffusion flame in the forward stagnation region of a porous cylinder immersed in a uniform air stream was one of the earliest studies on the extinction of non-premixed flames (Tsuji and Yamaoka 1966). The existence of a critical stagnation velocity gradient (i.e. strain rate), beyond which the flame can never be established, was reported. It was argued that the chemical limitation on the combustion rate in the flame zone was responsible for flame extinction at the critical stagnation velocity gradient. A more comprehensive study (Ishizuka and Tsuji 1981) using the same type of burner was carried out later on, where the blow-off limit in terms of either the critical fuel or the critical oxygen concentration was reported. It was concluded that the controlling factor for the non-premixed flame under limiting conditions is the limit flame temperature. A striped pattern, which is commonly described as cellular instability, was observed for flames established by hydrogen-nitrogen against air, where the flame resided in the oxidizer side of the stagnation point. The authors attributed this phenomenon to the preferential diffusion of H_2 relative to O_2 and claimed that it closely resembled a similar discovery in premixed flames. A detailed review of the extinction study on flames generated by this type of burner was given by Tsuji (Tsuji 1982). A study focused on the effect of air preheating and dilution of one of the reactants on the critical strain rate using the Tsuji-type burner was reported recently (Riechelmann et al. 2002). The critical strain rates of methane-air flame with either fuel or air diluted with various inert diluents were presented for air preheated to temperature as high as 1500 K. They found flame extinction always occurs at a finite strain rate even though the air temperature was raised well above the auto-ignition temperature.

There are many extinction measurements of non-premixed flames utilizing opposed-jet burners. Two opposing jets with fine screens installed at the exits were employed to study the extinction of diffusion flames burning nitrogen diluted methane and propane against diluted air (Puri and Seshadri 1986). Data were made available for the extinction limits in both the limiting fuel concentration and limiting oxidizer concentration cases. A set of experiments (Chen and Sohrab 1991) were performed to determine the critical minimum values of the fuel (oxidizer) concentrations at extinction for different values of the oxidizer (fuel) concentrations and various jet velocities in the opposed-jet burner using methane or butane mixed in nitrogen burning against oxygen/nitrogen. A comprehensive study (Pellett et al. 1998) on the strain-induced extinction of H_2/N_2-air flames using opposed-jet burners with both convergent and straight-tube nozzles of various sizes was performed. Extinction strain rate was measured for different fuel dilution ratios and compared with numerical simulations. Experiments in both microgravity (Maruta et al. 1998) and normal gravity (Bundy et al. 2003) conditions have also shown that the extinction strain rate of the counterflow non-premixed diffusion flames are double-valued, i.e. two kinds of extinction exist at a given fuel concentration. Radiative heat loss was responsible for the flame extinction at low strain rate. The study on the extinction of counterflowing non-premixed flame in a high pressure environment (Law 1988b; Sato 1991) revealed the pressure dependence of the extinction stretch rate for various fuels burning against air. The extinction stretch rate of methane was found to be constant at pressures below 2 MPa, beyond which its value decreases with pressure. The experimental results

were then used to extract the pressure exponent characterizing the dependence of the so-called apparent flame strength on pressure.

The theoretical study on the extinction of the diffusion flames was first carried out using large activation energy asymptotics (Liñán 1974). The tangent at the upper branch of the characteristic S-curve represents the extinction condition. The critical Damköhler number was expressed explicitly as a function of the initial conditions and the activation energy. Additional theoretical work (Krishnamurthy et al. 1976) removed some of the restrictive approximations in Liñán's original work, which include the requirement on diffusion-flame regime by introducing a corresponding correction in the calculation procedure, the assumption of constant density by using ideal-gas law with constant pressure, and the assumption of constant transport coefficients by introducing temperature dependant values. An extinction criterion was derived and summarized (Williams 1981). The large activation energy asymptotic analysis was further extended to diffusion flame extinction with radiative heat loss (Sohrab et al. 1982) and general Lewis numbers (Chung and Law 1983; Kim and Williams 1997). In all these studies, the extinction criterion are all of the same form as that of (Liñán 1974) with the only difference being the appropriate correction coefficients. A quantitative comparison of the extinction limit between the theoretical prediction and experiment was put forth by (Chen and Sohrab 1991). Despite the assumption of a one-step overall irreversible reaction, reasonable agreement was achieved. The calculated extinction limits of either fuel or oxidizer with non-unity Lewis numbers suggested that the molecular diffusivity of the deficient component had substantial effects

when the stretch rates were very small.

Numerical investigation of the extinction of diffusion flames with detailed chemistry started in the 1980's. An extinction prediction on the Tsuji type burner using complex chemistry and detailed formulation of the transport fluxes was performed through the collaborated efforts of five research groups (Dixon-Lewis et al. 1984). Extinction strain rate was predicted and compared well with the measured values of (Tsuji and Yamaoka 1969; Tsuji 1982), where thermal quenching effects were minimal. The use of extinction scalar dissipation rate defined at the stoichiometric mixture fraction to characterize the general flame quenching situations in turbulent combustion was enforced by their calculation. An opposed-jet methanol-air diffusion flame was studied using different reaction mechanisms (Seshadri et al. 1989). The key reactions responsible for extinction were identified through comparisons of the reaction rates at near-extinction conditions; the rate coefficients of which were found to greatly affect the calculated extinction stretch rate. The influence of boundary conditions on the prediction of the extinction of the methane-air-nitrogen opposed-jet diffusion flames was studied numerically (Chelliah et al. 1990). Comparing with experimental results, the authors demonstrated that the performance of most counterflow burners was more closely described by imposing the plug-flow boundary condition rather than the potential-flow condition. The importance of the temperature of the oxidizer stream on extinction of strained hydrogen-air diffusion flames was numerically investigated with detailed chemistry (Darabiha and Candel 1992). They showed the existence of a critical initial temperature of the oxidizer stream beyond which

flame extinction does not occur. The validity of the fast chemistry assumption in the asymptotics analysis at near-extinction conditions was confirmed by the calculation.

Despite the extent in experimental and numerical studies on the opposed-jet, non-premixed flames, efforts using opposed tubular burner are yet to be made. Such investigations are needed to understand how curvature affects flame extinction.

Instability

Flames at near extinction conditions often exhibit instability, which leads to cellular structure and/or oscillation. Cellular instability of non-premixed flames have been reported by several researchers using various types of burners. One of the earliest studies was reported by (Dongworth and Melvin 1976), where a Wolfhard-Parker burner was used. Flames produced by hydrogen/nitrogen-air exhibited cellular structure at a certain fuel dilution ratio. The authors postulated that inter-lancing of non-premixed stream and premixed stream of fuel and oxidizer through inter-stream diffusion at the flame base produced non-uniform distribution of fuel at the flame base, and were therefore responsible for the occurrence of cellularity, although the factors determining the size of the cells was not clearly identified. Cellular instability and flame extinction using a slot-jet burner were systematically studied by (Chen et al. 1992), where hydrogen, methane and propane diluted with a variety of inert diluents were used. Based on the experimental result, they proposed that a near-extinction condition and sufficiently low Lewis number of the defi-

cient reactant stream ($L_e \leqslant 0.8$) were the two requirements for flame to exhibit cellular instability. The Lewis number (diffusive-thermal) effect in a manner similar to that of premixed flames was argued to be the driving force instead of the effects of preferential diffusion. The diffusive-thermal instability of non-premixed flames was further investigated in a counterflow slot jet burner at low Lewis number (Kaiser et al. 2000). Tube-like flames generated by the balance between flame weakening due to strain and intensification due to curvature was reported for the H_2/N_2-air flames. Flame tubes of various states were observed under various flow configurations.

Theoretical work on the diffusional-thermal instability of diffusion flames was first done by (Kim et al. 1996), where activation-energy asymptotics was applied to the model of a one-dimensional convective diffusion flame. Attention was focused on striped patterns formed in near-extinction flames with Lewis numbers less than unity, under which conditions the reactants with high diffusivity diffuse into the strong segments of the reaction sheet, and the regions in between become deficient in reactant and are subject to local quenching that leads to the striped patterns. According to the analysis, the cell or stripe sizes are of the same order with the size of the convective-diffusive zone. An explicit equation on calculating the characteristic size was postulated, and the estimated values correspond well with the early experiments (Dongworth and Melvin 1976; Ishizuka and Tsuji 1981; Chen et al. 1992).

The above theory on the diffusional-thermal instability was expanded and generalized by a series of subsequent studies (Kim 1997; Kim and Lee 1999). The analysis demon-

strated that besides the possibility of cellular instability for Lewis numbers less than unity, pulsating instability is possible for Lewis numbers much greater than unity (Kim 1997). An effective Lewis number was introduced to facilitate the study of the effects of unequal Lewis numbers for fuel and oxidizer, the threshold of which was obtained for both large and small Lewis number cases (Kim and Lee 1999). A traveling instability was also proposed to occur in a small range of Lewis numbers, and oscillating instability were found to be accessible only for flames burning heavy hydrocarbon fuels or diluted by extremely light inert gases. The nonlinear dynamics of striped diffusion flames is investigated numerically in (Lee and Kim 2000; 2002), where the extension of the flammability limit beyond the static extinction condition of a one-dimensional flame was discovered in the former and transition Damköhler numbers between different striped patterns were calculated in the later.

Curvature Effects

While research on extinction of the non-premixed flames subject to the effects of flame stretch and non-unity Lewis number abounds, experimental studies on the effects of curvature are less numerous. This is mainly because of the difficulties in establishing a simple geometry that will allow detailed investigations. However, the importance of the curvature effects is not to be neglected. In turbulent combustion, the strained flamelet may have concave or convex curvature and may be affected by preferential diffusion when the Lewis number is substantially different from unity (Takagi et al. 1996b). Despite the dif-

ficulties, efforts, including studies on the tip-opening of Burke-Schumann flames and perturbed opposed-jet flames, have been made to investigate the curvature effects on mainly flame extinction.

Experiments on the tip-opening (flame extinction at the tip) of Burke-Schumann diffusion flames were conducted by Ishizuka et al. (Ishizuka 1982; Ishizuka and Sakai 1986), where flames generated by H_2/C_3H_8 diluted with He, N_2, Ar, CO_2 and H_2/CH_4 diluted with N_2 burning against air were investigated separately. Both studies concluded that while preferential diffusion was the dominant factor of causing the tip-opening, strong flame curvature also made some contribution. Cellular structures similar to that of (Dongworth and Melvin 1976) were observed at the flame base for fuel dilution ratio within certain ranges. Subsequent numerical investigation of this flame, taking into account detailed chemical kinetics and multicomponent diffusion confirmed the role of preferential diffusion on the tip-opening phenomenon (Takagi and Xu 1996). The effect of curvature was argued to have minor effects of the overall flame temperature distribution in this flame (Takagi et al. 1996a). A combined theoretical and experimental study (Im et al. 1990) on the tip-opening phenomenon was conducted later. According to asymptotic analysis of the flame structure in the tip region, they discovered that increasing the extent of flame curvature (reducing the radii of curvature) enhanced the burning intensity for unity Lewis number flames through the Damköhler number influence (longer residence time). As a result, tip opening can only be achieved by using a fuel mixture of Lewis number less than unity when the Lewis number effect overrides the flame intensifying

effect due to the tip curvature. Their experiments on diffusion flames using $H_2/N_2/CO_2$-O_2/N_2 ($L_e < 1$) as reactants supported their arguments of the sub-unity Lewis number case, but explanation of the near-unity Lewis number case using experiments with C_2H_2/N_2-O_2/N_2 ($L_e \approx 1$) mixture was questionable.

Experiments on the transient interaction between a vortex and a strained diffusion flame were first conducted by (Rolon et al. 1995). using a nozzle-type opposed-jet flame perturbed by a cylindrical tube installed along the axis of one of the nozzles. They discovered local extinction in the perturbed flame and suggested that the unsteady extinction strain rate was greater than the steady state extinction strain rate due to flame stretch alone. Similar experiments using hydrogen/nitrogen-air was carried out by Takagi et al., where the flame was perturbed by a steadily impinging micro jet (Takagi et al. 1996b). The experiments found out that when the micro jet issues fuel from the fuel side (concave curvature), the flame is easily quenched along the axis of symmetry locally, but the flame strained from the air side (convex curvature) hardly extinguishes. Their laser Rayleigh scattering measurement detected higher flame temperature in the later case. Together with numerical simulation, they argued that these phenomenon were the result of flame curvature in relation to preferential diffusion, where hydrogen fuel is more diluted by nitrogen in the first case and more concentrated in the second case than the original fuel concentration without impinging jet. The same experimental setup was used later to study the transient local extinction and re-ignition behavior with a transient impinging micro jet (Yoshida and Takagi 1998). The flame can survive under very high local stretch when micro jet impinges

from the air side where the steady flame cannot exist. Re-ignition was observed and the flame temperature was discovered to be significantly higher than that of the original flame. All these behaviors were attributed to the combined effects of preferential diffusion and flame curvature.

Two types of transient flame extinction patterns, namely point quenching and annular quenching were reported in a OH LIF and numerical study of interaction of the transient vortex and opposed-jet flame of hydrogen/nitrogen-air (Katta et al. 1998). The point quenching pattern was discovered when the vortex was traveling fast toward the flame surface, and annular quenching when the vortex was traveling slow. The combined effects of preferential diffusion and flame curvature were argued to be the reason of the annular quenching, although this was contrary to other researchers discovery that convex curvature would increase the flame intensity for hydrogen-air flame. Similar annular quenching was observed by separate experiments using simultaneous PLIF/PIV to investigate vortex induced extinction in H_2-air counterflow diffusion flames (Thevenin et al. 2000; Meyer et al. 2004), where OH PLIF images of high temporal resolution were obtained. From the PIV data, velocity gradient normal to the flame surface across the centerline and the annulus was compared. The result indicated that the local strain rate may not be the controlling parameter in the initiation of the annular extinction. An assessment of the radii of curvature at the two locations by the authors demonstrated that curvature induced fuel-rich condition was responsible for the onset of the annular extinction. However, this argument was again contradictory to other studies (e.g. Takagi et al.).

A curved diffusion flame established in the wake of a bluff-body in an opposed jet burner was studied in a attempt to separate the influence of flame stretch and curvature (Finke and Grünefeld 2000). Despite the non-uniform curvature at the flame front, the authors inferred the radius of curvature from the OH LIF images of the flames, and flame extinction limits of H_2/N_2-O_2/N_2, D_2/N_2-O_2/N_2 or H_2/He-O_2/He mixture as a function of the radius of curvature and fuel-oxidizer concentration were presented. For H_2/N_2-O_2/N_2 flame, two kinds of extinction phenomena were observed, global extinction when flame was concave toward the oxidizer stream and local annular extinction when convex. In both cases, the limiting O_2 concentration was found decreasing with increasing radius of curvature. While for the convex flame case this was reasonable since the curvature was expected to weaken the flame through preferential diffusion, the authors argued that the strain rate increase in the concave flame case over-compensated the flame strengthening due to curvature. Additional experiments using either D_2 as the fuel or He as the diluent exhibited smaller separation of limiting O_2 concentration between convex and concave curved flames, which supporting the argument that preferential diffusion combined with curvature was the dominating factor concerning the extinction behavior. Study by (Santoro and Gomez 2002) using methanol found that extinction required vortices of larger circulation if generated from the oxidizer side comparing to the fuel side. This was attributed to the stretching of the vortex approaching the stagnation plane.

A recent study (Lee et al. 2000) using direct numerical simulations of opposed-jet H_2-air diffusion flame-vortex interactions supported the observations by Takagi et al. that

is, when the reaction zone is convex towards the air stream, the flame weakens and extinguishes locally in some cases; when the opposite curvature is produced, a region of increased reactivity is observed. It was further shown that depending on the direction of the curvature, the flame may either extinguish locally at a scalar dissipation rate smaller than or intensify to produce higher temperature at a scalar dissipation rate larger than that of the corresponding steady, one-dimensional flat diffusion flame, i.e. the common use of a single extinction scalar dissipation rate in turbulent diffusion flame simulations are questionable.

In summary, curvature has only minor effects on the tip-opening of the Burke-Schumann flame, where the effects of preferential diffusion dominants. In the flame/vortex interaction, curvature plays a more important role, but studies were qualitative in nature and focused more on the extinction phenomena due to the non-uniform curvature along the flame surface and the transient nature of the problem under investigation in some cases. On the contrary, opposed tubular flames have the advantages to allow more detailed quantitative study of non-premixed flame subject to the influences of both uniform stretch and uniform curvature, and therefore deserve more attention.

Tubular Flame

Due to its relative simplicity, the tubular premixed flame was first introduced more than three decades ago. In (Ishizuka 1984) work, the tubular flame was established in a swirl type burner with a rotating flow field, in which fuel/air mixture was ejected tangentially from an inlet slit into the combustion chamber. Combustion products were ejected

from the two ends of the burner, and therefore the tubular-shaped flame was stretched along the axis of rotation. Tubular premixed flames of lean hydrogen/air and methane/air with uniform flame fronts were successfully established, while much difficulty was met when trying to produce a lean propane/air flame with uniform flame front due to the Lewis number effect. This effect was further elaborated in a subsequent study (Ishizuka 1989), where rich mixtures of methane/air and propane/air were investigated. It was discovered that these two mixtures behaved oppositely in terms of the uniformity of the flame front. In addition, different types of flame regions formed in the swirl type burner were mapped based on the injection velocity and equivalence ratio. Structural measurement of lean methane/air flame on the swirl type burner was conducted using thermocouple and sampling probe with gas chromatography (Sakai and Ishizuka 1991). It was shown that the combustion field was separated by the luminous flame zone into two regions: an outer unburned gas region and an inner burned gas region. The flame structure at large diameters was very similar to that of planar premixed flame. However, as the extinction limit was approached, the effects of curvature and incomplete reaction were responsible for flame extinction. A review of the tubular premixed flames was put forth by (Ishizuka 1993), where the effects of Lewis number and various patterns of instability were summarized. A new concept to describe the turbulent combustion as an ensemble of tubular flamelets was discussed. The effects of rotation on the stability and structure of the tubular flame was investigated experimentally using OH laser-induced fluorescence technique (Yamamoto et al. 1994). According to the experiment, radial OH concentration took different shapes

when the intensity of rotation was varied and the lean concentration limit was decreased with increasing rotation intensity. The enhanced stability by rotation was attributed to a mechanism like the excess enthalpy flame.

A tubular premixed flame formed by mixtures ejected from the radially, inwardly converging nozzle was first investigated by (Kobayashi and Kitano 1989). Extinction limits of methane/air and propane/air mixtures with a wide range of equivalence ratios were measured and compared with the counterflow flame results. The extinction diameter was also measured at various equivalence ratios for both fuel types. The difference in the extinction limits was explained by the authors in terms of the Lewis number effects on the flame temperature and preferential diffusion effects on the reactant concentration. Flame curvature was shown to enlarge the former two effects. The flow fields of the stretched cylindrical premixed flame and the counterflow twin flame were measured with stoichiometric methane/air mixtures using LDV technique (Kobayashi and Kitano 1991), where quantitative comparison for the two types of flames was made. The combined effects of flame stretch and curvature were shown to be responsible for the lower velocity gradient of the cylindrical flame at extinction than that of the twin flames.

Non-intrusive laser diagnostics in the premixed tubular flames were not conducted until recently (Mosbacher et al. 2002), when lean hydrogen/air flames (Φ=0.175) at various stretch rates were studied. Temperature and major species concentration profiles with high resolution were obtained using the laser-induced Raman scattering technique in a unique, optical accessible tubular burner. The measured results were compared to the numerical

prediction with detailed reaction mechanisms and transport formulation. Good agreement was found at lower stretch rates, while the discrepancy at high stretch rates was attributed to the effects of turbulence. Measurement of tubular hydrocarbon premixed flames using the laser-induced Raman scattering technique was conducted later by (Hu et al. 2006b). With careful arrangement of the injection flow, the burner was able to operate at higher flow rate without the contamination of the turbulence. The hydrogen flame experiments with Φ=0.175 were repeated and a condition closer to extinction limit (Φ=0.152) was measured as well. Comparison between experimental data and numerical prediction demonstrated good agreement, which validated the performance of the tubular burner as well as the numerical model. Temperature and major species concentration distributions of methane/air and propane/air premixed flame were measured subsequently and compared with numerical simulation using detailed chemical reaction mechanism. The effects of curvature were discussed based on the peak flame temperature comparison of tubular flames and opposed-jet planar flames.

Theoretical study on tubular premixed flames started with activation energy asymptotics (Mikolaitis 1984a; 1984b), where it was concluded that the flame curvature can only amplify the effects of stretch on flame speed and cannot affect the flame speed in a non-stretched situation. The effects of Lewis number on the tubular flame extinction was also studied using activation energy asymptotics (Takeno et al. 1986). The flame temperature at extinction was found to decrease with increasing Lewis number and was greater

than the adiabatic flame temperature when L_e < 1. The extinction behavior of the tubular flame was different from that of the planar flame due to the effects of curvature, which provides the increased cooling. The influence of variable density (Nishioka and Takeno 1988) and heat loss (Kitano et al. 1989) was studied with special interest on the extinction behavior. Activation energy asymptotics was also used in (Libby et al. 1989) to analyze the structure and extinction characteristics of a premixed flame in a right circular cylinder enclosing a stretching vortex line. It was shown that the circulation motion did not influence the flame structure, but the stretch of the vortex affected the structure and extinction of the flame. An analytic solution of the flow field of the tubular flames was obtained in a recent study (Wang et al. 2006b) to show that the stretch rate of the tubular premixed flame was better represented by $\pi V/R$, where V is the exit velocity and R is the radius of the nozzle. This study provided a viable way to draw comparisons between tubular flames and flames of other geometry, where the flames are characterized by a single parameter.

Numerical simulation of the tubular premixed flames with the use of complex chemistry and detailed transport formulation was conducted as a collaborating effort to test the model and the detailed mechanisms (Dixon-Lewis et al. 1990). The computed extinction limit for the stoichiometric methane-air flame was more sensitive to the details of the reaction kinetic scheme than the flame diameter. The numerical calculation was used to predict the extinction limit of methane/air and propane/air flame (Smooke and Giovangigli 1990) and compared with the experimental data of (Kobayashi and Kitano 1989). Excellent agreement was obtained between the calculated and measured results, although significant

difference was found when the tubular flame results were compared with the corresponding twin counterflow flames. The effects of varying circumferential velocity was investigated for a tubular methane-air mixture formed in a stretched vortex flow (Yamamoto et al. 1996). With increased circumferential velocity, the concentration of the lighter (heavier) species in the center increased (decreased), which resulted in changes in reaction rates and flame temperature. The authors attributed this phenomenon to the pressure gradient due to the pressure drop near the center induced by the rotation, which yielded the mass transport by the pressure diffusion. The effects of curvature on a tubular methane/air premixed flame was studied with detailed chemistry under weakly stretched conditions near lean extinction limit (Ju et al. 1998). Extinction under this condition was induced by radiation heat loss. It was found that flame curvature can extend this extinction limit.

Early tubular non-premixed flames were investigated by Tsuji et al. in a series of studies on flames generated by in the forward stagnation region of a porous cylindrical burner opposed to a uniform oxidizer stream (Tsuji and Yamaoka 1967; 1969; 1971; Tsuji 1982). Tubular partially-premixed flames were also studied by the same group (Yamaoka and Tsuji 1977; Tsuji and Yamaoka 1982). Despite the great achievement on the understanding of the counterflow diffusion flames from these researches, the curvature effects were generally neglected due in part to the large tube diameters used. In order for curvature to dominant or at least have the same order of effects as others, the radius of curvature of the opposed tubular flame needs to be small. An opposed tubular burner has to be used.

Time Scale Analysis

A time scale analysis can provide practical guidance in experimental considerations and is carried out in this section. Damköhler number defined as the ratio of the characteristic flow time over chemical reaction time (Williams 1985) is often used in the discussion of the flow/reaction interaction. Damköhler numbers of the first and second kind are

$$D_I = \tau_{fl} / \tau_{ch} , \qquad D_{II} = \tau_{df} / \tau_{ch} \tag{1.1}$$

where τ_{fl}, τ_{df} and τ_{ch} are characteristic flow, diffusion and chemical times, respectively. In opposed tubular flames, flow time, τ_{fl} can be estimated as $(R_2 - R_1)/(V_F + V_O)$. While the overall diffusion time can be given as $\tau_{df} = (R_2 - R_1)^2 / \alpha$, diffusion time due to radius of curvature is better evaluated by $\tau_{df,cv} = R_f^2 / \alpha$ where subscript f denotes flame location. The chemical time can be obtained from the premixed flame analogy, i.e. the properties of a stoichiometric mixture of the fuel and oxidizer at the same pressure and initial temperature, through this relation $\tau_{ch} = \alpha / S_L^2$ where the laminar burning velocity S_L can be very well determined via simulation means. The effects of buoyancy can be represented by the characteristic buoyancy time defined as $\tau_{by} = d / U_{by}$ where $U_{by} = \left[gd(\Delta\rho/\rho)^{1/2} \right]^{1/2}$. Because $\Delta\rho/\rho \approx 1$ for flames, the expression for the characteristic buoyancy time reduces to $\tau_{by} = (d/g)^{1/2}$. The Froude number, which represents the relative intensity of the forced and buoyancy induced flow, can be calculated as $Fr = (\tau_{by} / \tau_{fl})^2$. Large Froude number indicates the flame is momentum-controlled, in other words, the buoyancy effect is unimportant. For optically thin radiation, the characteristic radiation time can be estimated by $\tau_{rd} = [\gamma/(\gamma-1)]\{P/[4a_P\sigma(T_f^4 - T_\infty^4)]\}$ where T_∞ is the ambient temperature.

For the near extinction flames studied in Chapter IV, two sets of time scales evaluated

using the above expressions are shown in Table 1, one for the 15% H_2/N_2-air flame and one for the 26% CH_4/N_2-air flame. For the hydrogen flame, the $k = 60$ s^{-1} case is selected where $S_L = 0.048$ m/s calculated from PREMIX program of the Chemkin package, $T_f \approx 1200$ K, $V_O = 0.21$ m/s and $V_F = 0.19$ m/s. For the methane flame, the $k = 166$ s^{-1} case is selected where $S_L = 0.094$ m/s, $T_f \approx 1770$ K, $V_O = 0.58$ m/s and $V_F = 0.52$ m/s. In both cases, $\alpha \approx 1.0 \times 10^{-4}$ m^2/s, $a_P = 0.8$ m^{-1}, $R_2 = 0.015$ m, $R_1 = 0.003$ m, $\gamma \approx 1.35$, $T_\infty \approx 300$ K, $P = 1$ atm and $R_f = 0.0065$ m.

Table 1 Time scales for $k = 60$ s^{-1}, 15% H_2/N_2-air and $k = 166$ s^{-1}, 26% CH_4/N_2-air opposed tubular flames (time scales given in seconds)

Time Scale	H_2/N_2-air	CH_4/N_2-air
Chemical time (τ_{ch})	0.043	0.011
Flow time (τ_{fl})	0.030	0.011
Diffusion time ($\tau_{df,cv}$)	0.423	0.423
Buoyancy time (τ_{by})	0.055	0.055
Radiation time (τ_{rd})	1.043	0.22
D_I	0.698	1
D_{II}	9.84	38.5
Fr	3.36	25

Several observations can be made on the basis of these estimates:

1. The flame and flow interaction is important for these flames because τ_{ch} is on the same order of τ_{fl}.

2. The buoyant convection is important for flames at low stretch rate conditions where Fr is close to unity and negligible for flames with high stretch rates where $Fr >> 1$.
3. Curvature has only secondary effect on these flames because $\tau_{df,cv} > \tau_{ck}$. To have a dominant curvature effects, the curvature induced diffusion time needs to be reduced, which means tubular flames with small radius of curvature is preferred.
4. Radiation effects are negligible for flames with moderate or high stretch rates because $\tau_{rd} >> \tau_{ck}$.

The main focus of this study is the effects of curvature on flames. From the above observations, the following should be considered:

1. The chemical time needs to be increased to promote the effects of curvature on tubular flames. This can be done by increasing the fuel dilution ratio and/or diluting the oxidizer stream.
2. The flow time can not be increased to much higher than that of the hydrogen case in Table 1, because otherwise the buoyancy effect will complicate the flow condition. The flow velocities at the nozzle boundaries are recommended to be greater than 0.20 m/s.
3. The radius of curvature is restricted by the size of the inner nozzle, and the curvature induced diffusion time cannot be reduced by much. An alternative way to study the curvature effects is to conduct a cross-comparison by keeping the flow time constant and change the diffusion time by changing the radius of curvature.

Organization

In pursuit of the research goals, Chapter II gives a brief background theory of the spontaneous Raman scattering technique together with the visible Raman scattering system utilized in this study, which includes a frequency-doubled Nd:YAG laser, a light delivering and collection system, a spectrometer and a data acquisition system. The calibration procedure for the Raman spectroscopy is described subsequently. A discussion of the uncertainty evaluation is also given.

Chapter III shows the experimental and simulation results of tubular non-premixed flames of nitrogen diluted hydrogen versus air. Temperature and major species concentration profiles of non-premixed tubular concave flames (15% H_2/N_2 vs. air) with stretch rates ranging from $k = 30$ to 242 s^{-1} are measured using Raman spectroscopy and compared with numerical simulation. Flame extinction and flame instability at the near extinction conditions are investigated in a first attempt. The effects of curvature on non-premixed flames are discussed.

In Chapter IV, structural measurements of hydrocarbon flames are conducted using the laser-induced Raman scattering method. Temperature and major species concentrations are recorded for flames produced by 30% CH_4/N_2 and 15% C_3H_8/N_2 burning against air. Numerical simulations of these flames with detailed chemistry produce good agreement between the measured and simulated results. The effects of curvature are further revealed by comparing the numerical results of the tubular flames with those of the opposed-jet

planar flames.

In Chapter V, extinction of the opposed tubular flames generated by burning inert-gases-diluted H_2, CH_4 or C_3H_8 with air is investigated for both concave and convex curved cases. Data are made available in terms of the initial mixture strength at various stretch rates. N_2, He, Ar or CO_2 diluent is used. The onset conditions of the cellular instability are recorded. The effects of curvature on both flame extinction and cellularity are further discussed. Finally, the conclusions and future work are summarized in Chapter VI.

CHAPTER II

EXPERIMENTAL SYSTEMS AND CALIBRATION

Raman Scattering System

Background Theory

Raman scattering is widely applied in combustion diagnostics (Eckbreth 1996). Lasers generating visible and ultraviolet light are typically employed. Raman scattering is the inelastic scattering of light from molecules and is instantaneous in nature. If a molecule gains energy from the incident light, the resulting lower frequency shift is termed Stokes Raman scattering; the opposite is termed anti-Stokes Raman scattering. An elastic scattering process, i.e. no energy exchange between the molecule and light, is termed Rayleigh scattering. Depending on the nature of the energy exchange between the light and the molecules, Raman scattering can also be termed rotational or vibrational. Pure rotational Raman scattering ($\Delta v = 0$) is not widely used for combustion diagnostics due to its small frequency shifts, which makes interpretation difficult. In vibrational Raman scattering ($\Delta v = \pm 1$), each shift component is associated with three rotational branches: Q($\Delta J = 0$), O($\Delta J = -2$) and S($\Delta J = +2$), which are normally not resolved. As a result, vibrational Raman scattering is often termed vibrational-rotational Raman scattering. The frequency shift of vibrational Raman depends on the vibrational frequency of the molecule and

therefore is species specific, contrary to the Rayleigh scattering. This feature renders Raman scattering well suited for combustion diagnostics.

The three light scattering processes are shown in Figure 4, where the thickness of the arrows represents the relative intensity of each process. Raman scattering is much weaker than Rayleigh scattering. In most cases, Stokes Raman scattering is the stronger one among the two Raman scattering processes, because molecules generally reside in the ground vibrational state. For this reason, most Raman scattering applications use the Stokes shift, and so does this work.

Raman scattering signal is linearly proportional to the species number density. The intensity of the measured Stokes Raman signal can be expressed in terms of the counts on the CCD camera, ξ_i, and is given by:

$$\xi_i = n_i \sigma_i E_l L \Omega \eta Q G f(T) / (h\nu_i) \tag{2.1}$$

where η accounts for the light loss on each surface of the optics, $f(T)$ is the bandwidth factor. The number density, n_i, of each individual species under investigation can be determined from the above relations. The temperature is then determined by evoking the ideal gas law for low speed flames, $T = P/(nk)$ where P is assumed to be the atmospheric pressure, $n = \sum_i n_i$ is the total number density from Raman measurement and k is the Boltzmann constant. Due to the uncertainties in determining some of the coefficients in Eq. 2.1, a calibration procedure, which will be described later, is generally employed to simplify the data interpretation. Because the Raman scattering is generally very weak, in practical combustion situations, only species with high enough concentrations can be

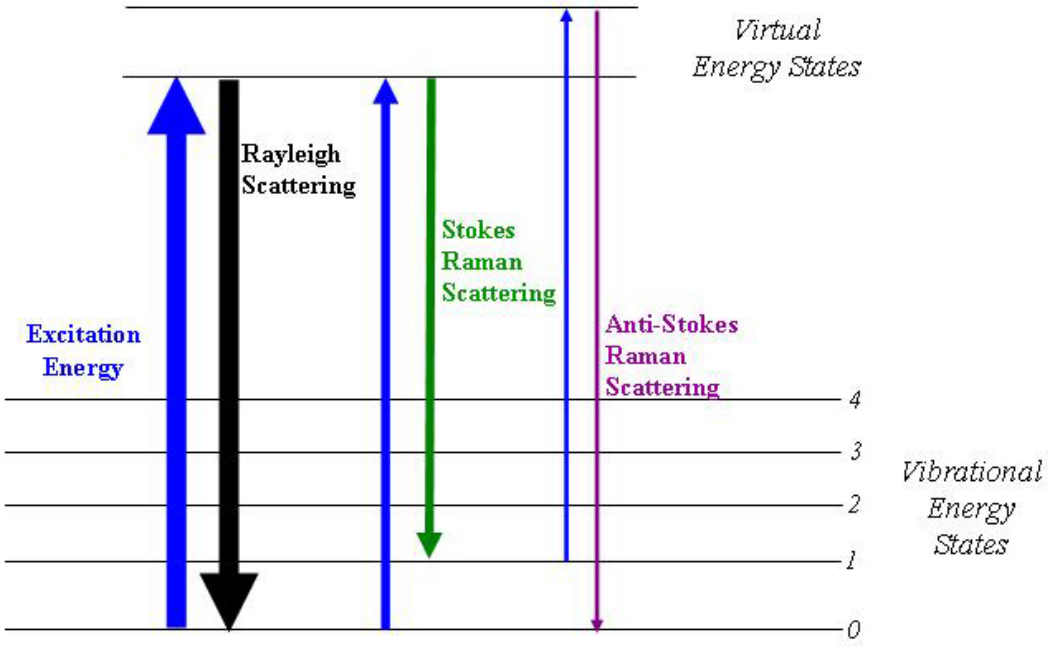

Figure 4 Rayleigh and Raman scattering process

measured. The omitted number densities of the minor species in evaluating the total number density will only generate a small deviation from the actual value and therefore the ideal gas law can still be used.

Experimental Setup

A detailed schematic diagram of the visible Raman system used in the study is shown in Figure 5. The laser source used in the system is the frequency doubled Nd:YAG laser at a repetition rate of 10 Hz. Either a Continuum Powerlite 9010 (~1000 mJ/pulse max.) or Surelite III-10 (~400 mJ/pulse max.) is used with the difference being the pulse energy. The laser beam passes through a rotatable zero order waveplate followed by a thin film plate polarizer mounted at its Brewster angle to enable continuous adjustment of the beam energy. The attenuated beam then goes through a pulse stretcher similar to that depicted by (Kojima and Nguyen 2002). The laser light is split into three sets of beams that are trapped in three optical ring cavities. Each beam experiences a different time delay. A laser pulse of approximately 150 ns long is produced. This allows a pulsed laser with much higher power to be used where laser-induced breakdown is avoided.

A very small portion of the laser beam is sampled by a beam sampler to monitor the pulse to pulse energy fluctuation. Relative energy measurement of every single laser pulse is recorded by the computer to be used in the data reduction process. The laser light is then focused by a 300 mm focal-length lens. The beam diameter is measured to be ~150 μm at the focal point. The scattered Raman light is collected at 90º using a f/2 achromat (3”

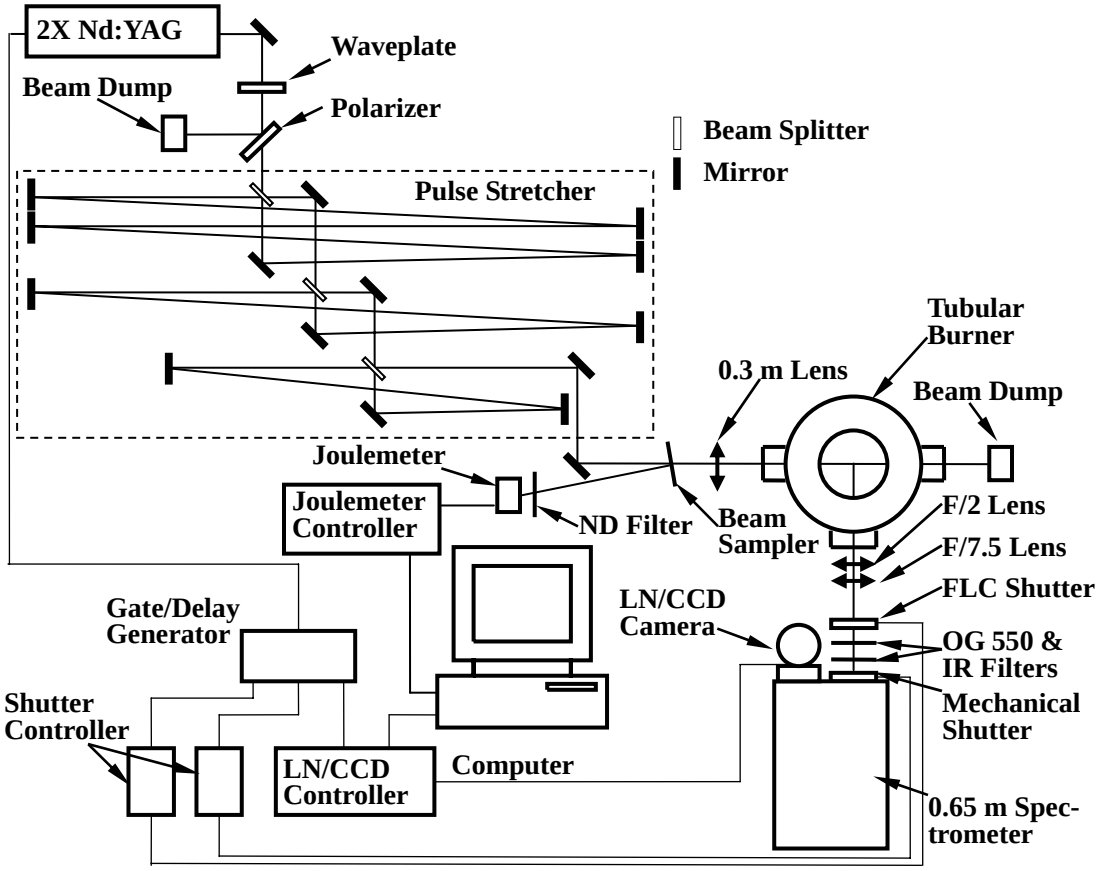

Figure 5 Schematic of the visible Raman scattering system

diameter) focused by a second achromat (f/7.5) onto the entrance slit of the spectrometer. The light is then dispersed by a 600 groove/mm grating and focused to a liquid-nitrogen cooled, back-illuminated CCD camera (1024 × 1024 pixels, Princeton Instrument) by a 0.65 m focusing mirror. The spatially resolved line imaging Raman signal is recorded by the camera. The sample volume (4.27 mm or 4.06 mm) is divided to 13 (or 26) sections, which gives a spatial resolution of 330 (or 156) μm. The ability of the system to resolve this spatial resolution is confirmed by back-illuminating a 6 lines/mm Ronchi grating placed in the sample zone. The laser beam passes 4.5 mm away from the axis of burner symmetry. The location of each data point in the radial direction is calculated based on the separation distance and its position along the laser beam from the point of symmetry.

The CCD camera is gated by a ferroelectric liquid crystal shutter (60 μs) and a mechanical shutter (6.0 ms) to reduce the background flame emission. The Rayleigh scattered light is blocked by an OG-550 filter. The flame illumination in the infrared region is blocked by an infrared filter (750 nm cutoff). 900 single-pulse Raman signals are integrated on the CCD chip to produce one Raman spectrum. The tubular burner is translated 3 or 4 times along the laser beam direction by a translation stage equipped with computer motion control units to cover the entire flame.

Calibration and Uncertainties

To obtain absolute species concentrations without evaluating all the coefficients in Eq. 2.1, the visible Raman system is calibrated using flames with known species concentration.

A multi-element Hencken burner is used for this purpose. The Hencken burner consists of 12.5 mm diameter multi-element matrix of tiny fuel jets inserted into honeycomb oxidizer matrix. A 4.3 mm wide N_2 co-flow annulus shields the flame from the environment to avoid interferences. Well-controlled flows of fuel and oxidizer emerge from the burner surface to form a matrix of tiny jet diffusion flames. At a long enough distance downstream (15 mm typical), the chemical reaction reaches equilibrium, the condition of which can be determined from adiabatic equilibrium calculations. The EQUIL package in the commercial software Chemkin is used for such calculations.

Common combustion products of hydrogen/hydrocarbon-air flames within the detection limit of the Raman scattering technique include H_2, H_2O, N_2, O_2, CO_2, CO, CH_4 and C_3H_8. Their Raman frequency shifts and the emission wavelength excited by the 532 nm Nd:YAG laser are listed in Table 2.

Table 2 Raman frequency shifts and corresponding emission wavelengths of major species for 532 nm laser

Species	**Frequency Shift. (cm^{-1})**	**Wavelength (nm)**
C_3H_8	860	557.51
CO_2 (2ν2)	1285	571.04
CO_2 (ν1)	1388	574.42
O_2	1556	580.01
C_2H_2	1973	594.39
CO	2145	600.53
N_2	2330.7	607.30
C_3H_8	2900	629.00
CH_4	2915	629.64
H_2O	3657	660.50
H_2	4160.2	683.21

Calibration factors, which are functions of temperature and species, are obtained through the calibration procedure and defined as:

$$C_{T,i} = \frac{E_l n_i}{\xi_i} \tag{2.2}$$

where n_i is a function of both temperature and species. The Raman signals in the entire sample volume instead of a single channel are used in obtaining ξ_i in order to minimized the uncertainty. The output mole fraction X_i from the EQUIL program at the given equivalence ratio together with the ideal gas law are used to calculate n_i.

Various calibration flames are utilized in the calibration process. H_2-air flames ($\phi = 0.27 \sim 3.0$) are used to evaluate C_{T,O_2}, C_{T,N_2}, C_{T,H_2O} and C_{T,H_2}. H_2-air-CO_2 flames ($\phi = 0.34 \sim 1.0$) are used to find C_{T,CO_2}. H_2-air-CO ($\phi = 0.36 \sim 2.7$) flames are employed to find $C_{T,CO}$. The calibration factors are typically plotted against temperature for each individual species. Through a second or third order polynomial curve fit, calibration functions, $C_i(T)$, are obtained. Due to small changes in the experimental conditions, the calibration factor curves are slightly different for each set of experiments. As a result, the calibration process is conducted every time before the actual experiment. A typical set of temperature dependent-calibration factors are shown in Figures 6-11.

Flame spectra obtained with laser wavelength at 532 nm have shown that CO_2 signal and O_2 signal partially overlap with each other at some conditions (e.g. Figure 12). To account for this interference, two temperature-dependent interference factors are defined: $K_{O_2-CO_2}(T)$, which represents the ratio of the O_2 signal in the CO_2 channel to the total CO_2

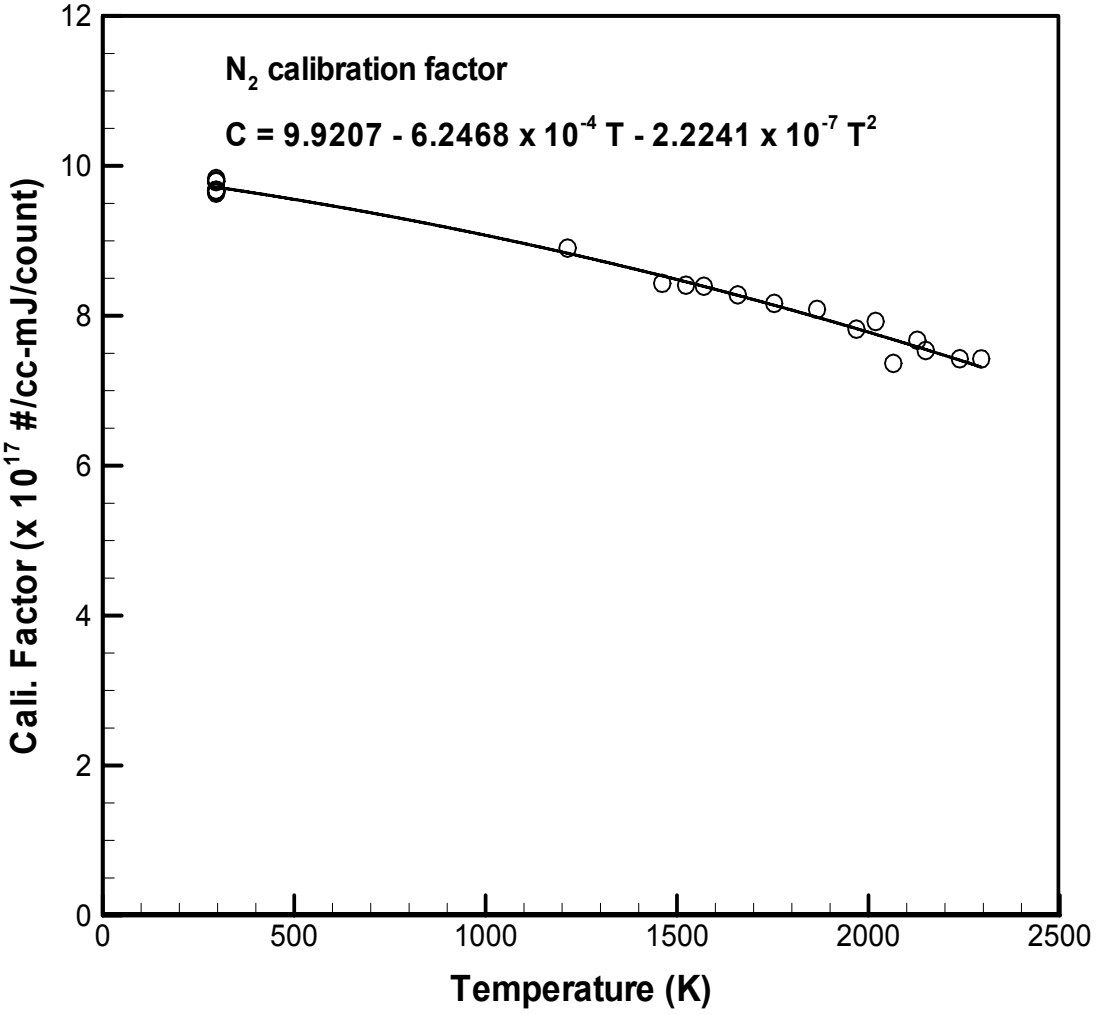

Figure 6 Temperature-dependent calibration factor of N_2

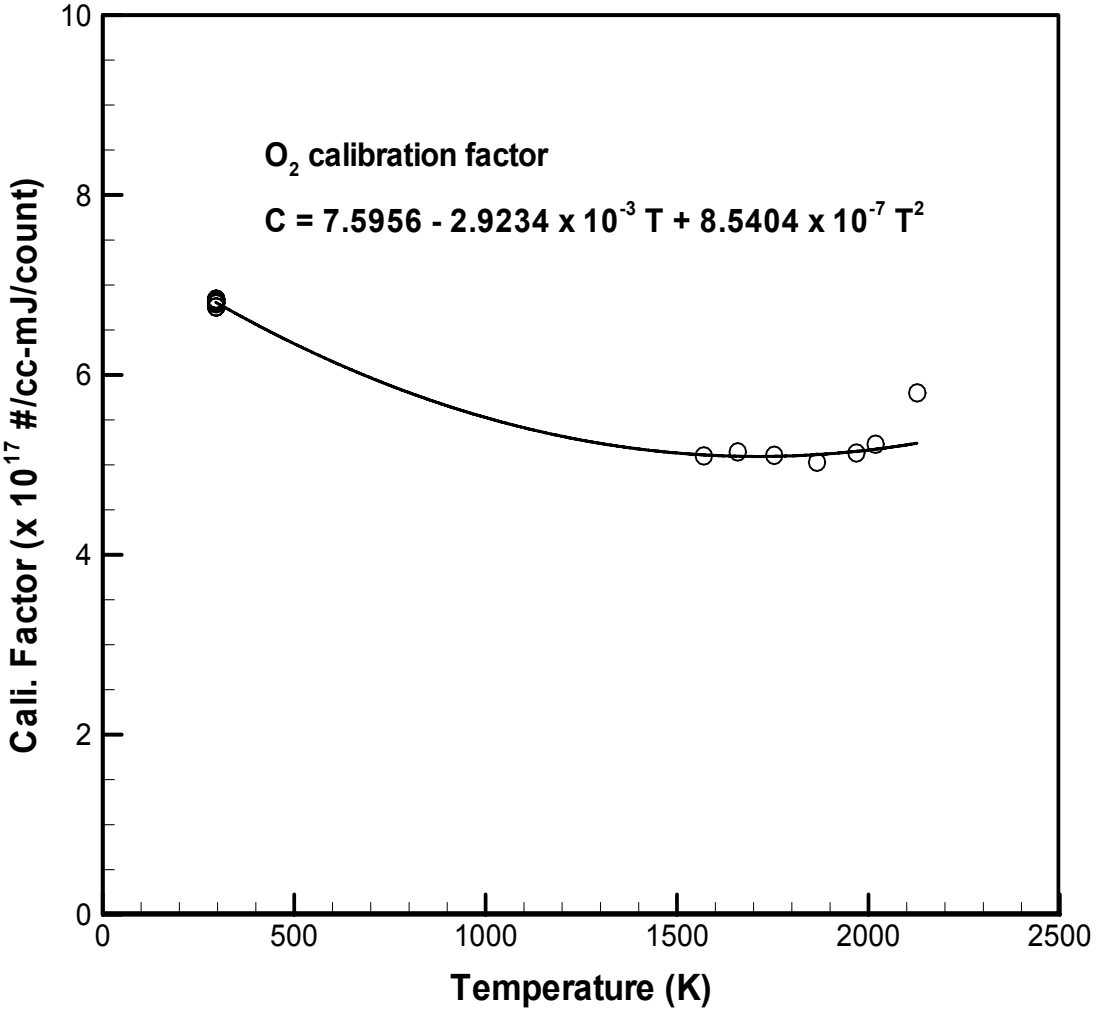

Figure 7 Temperature-dependent calibration factor of O_2

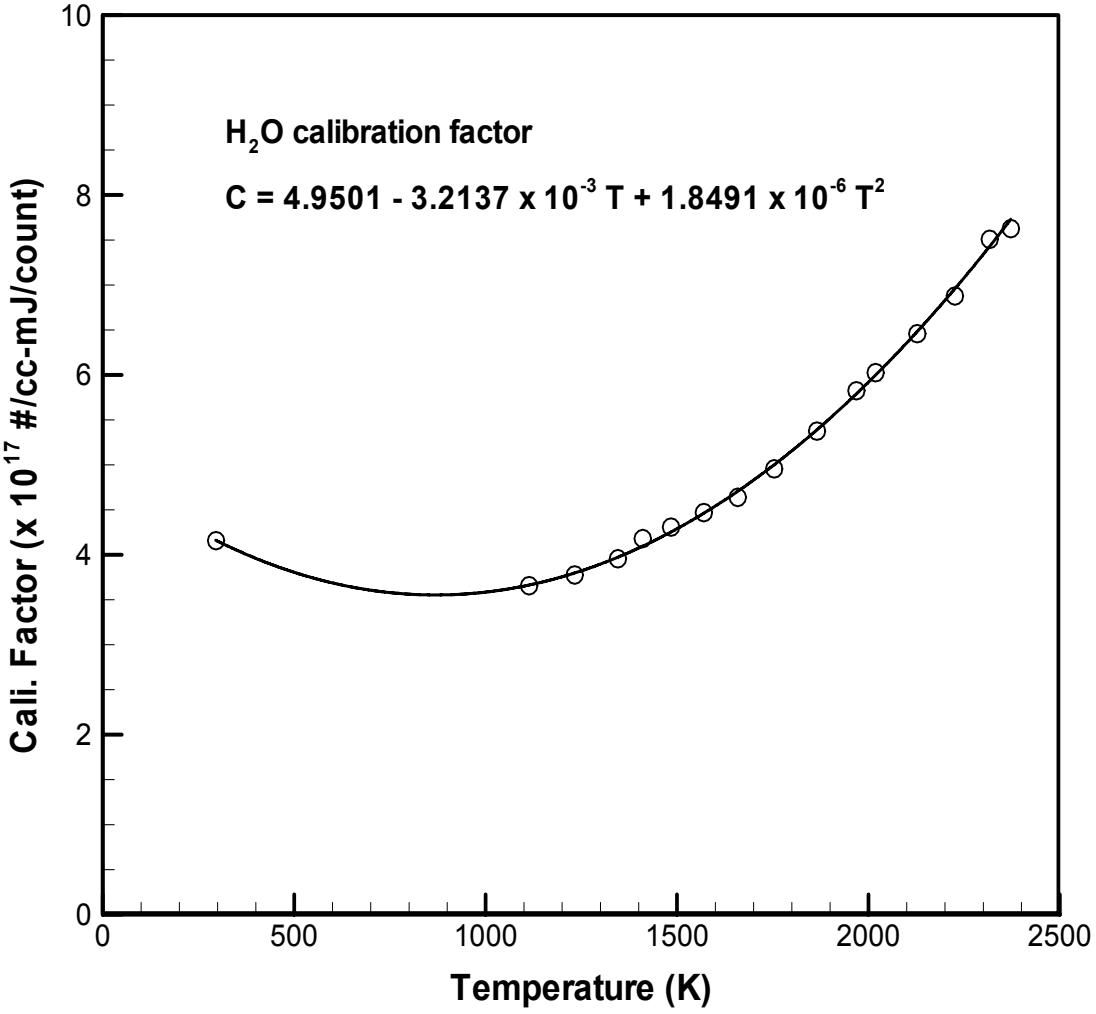

Figure 8 Temperature-dependent calibration factor of H_2O

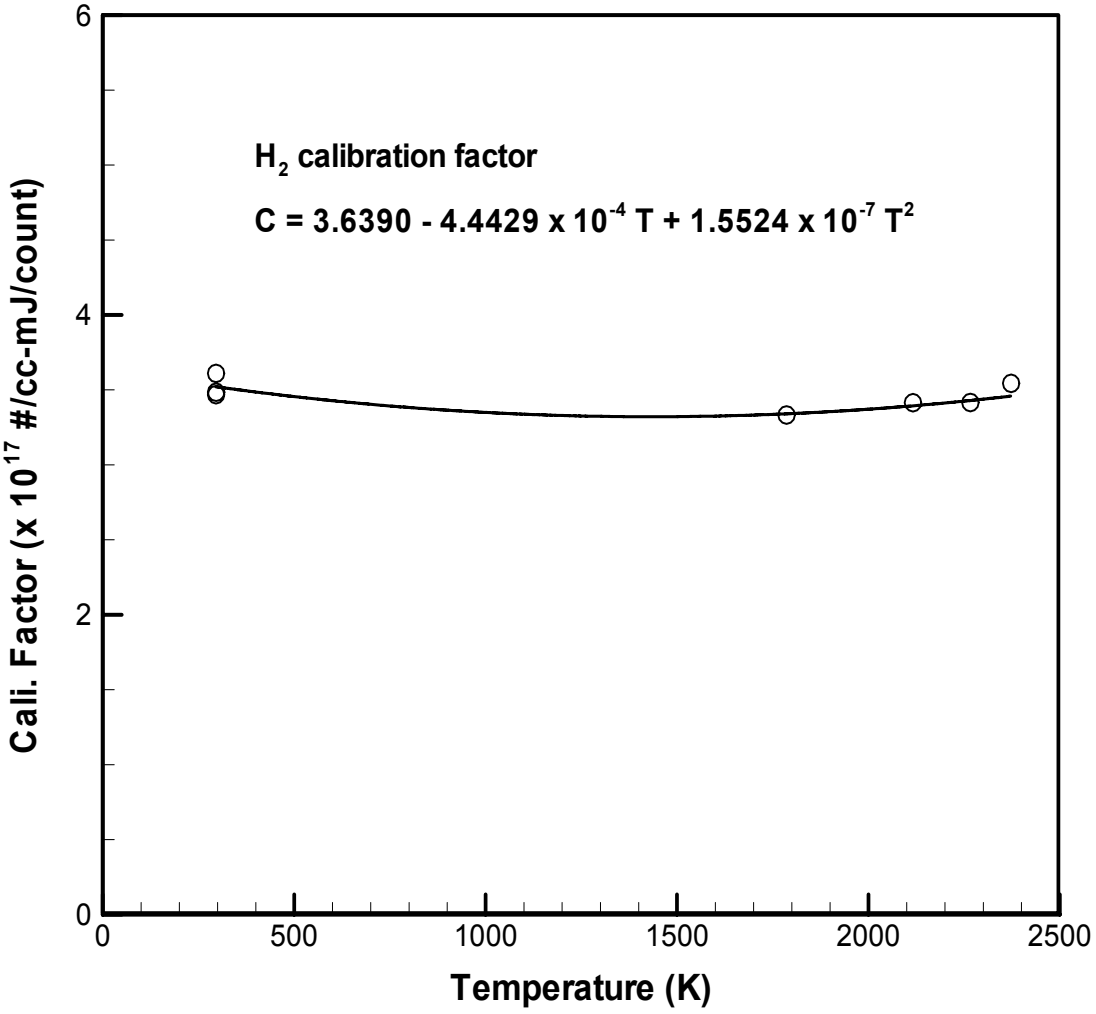

Figure 9 Temperature-dependent calibration factor of H_2

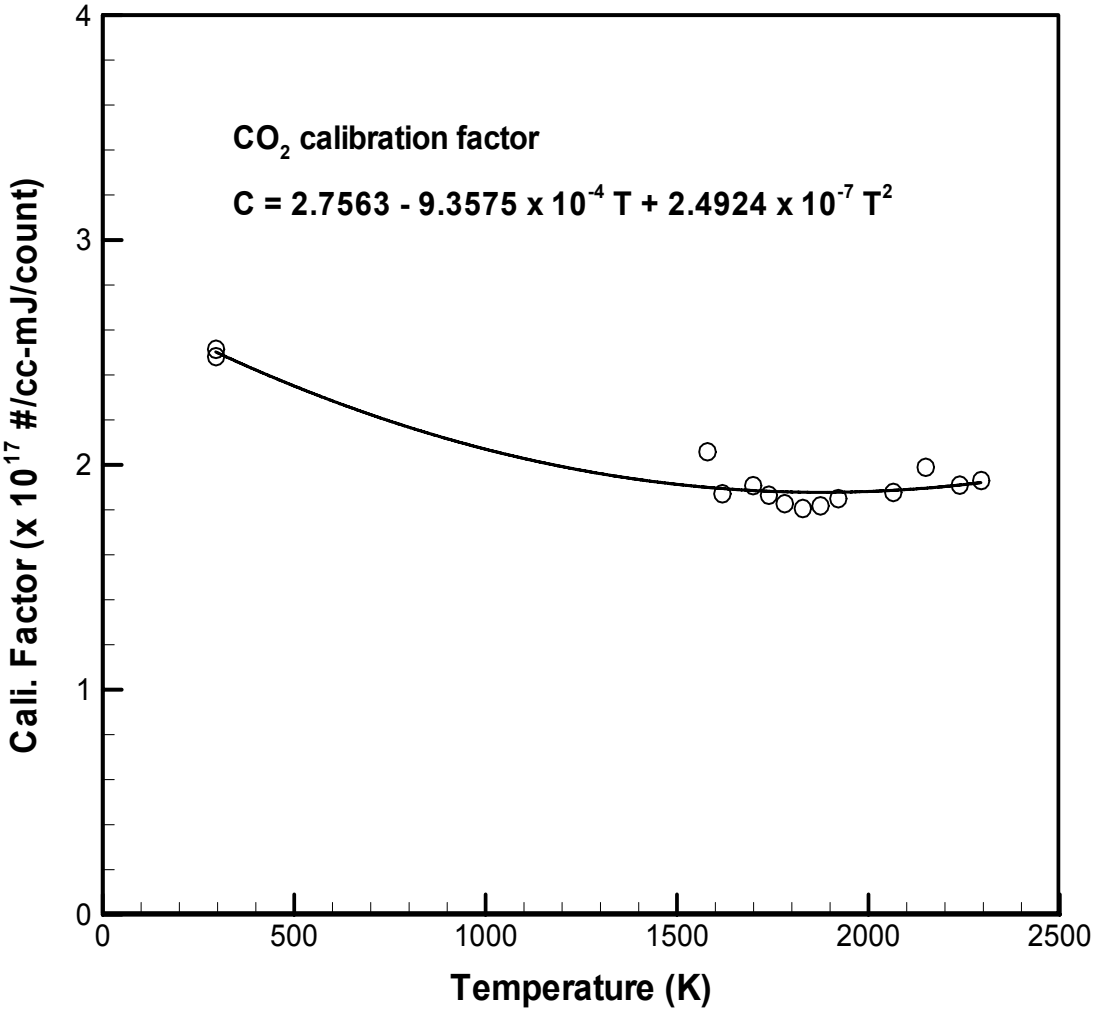

Figure 10 Temperature-dependent calibration factor of CO_2

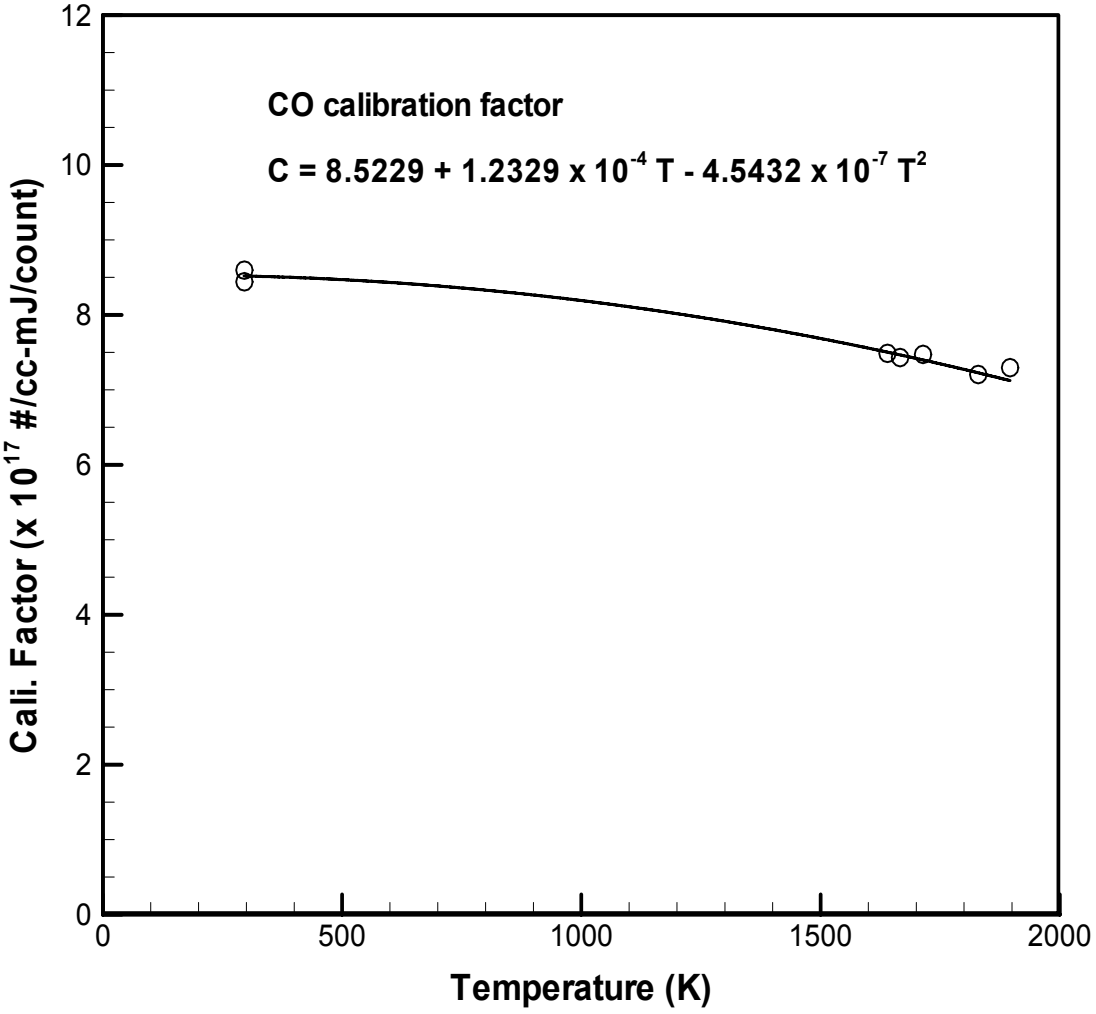

Figure 11 Temperature-dependent calibration factor of CO

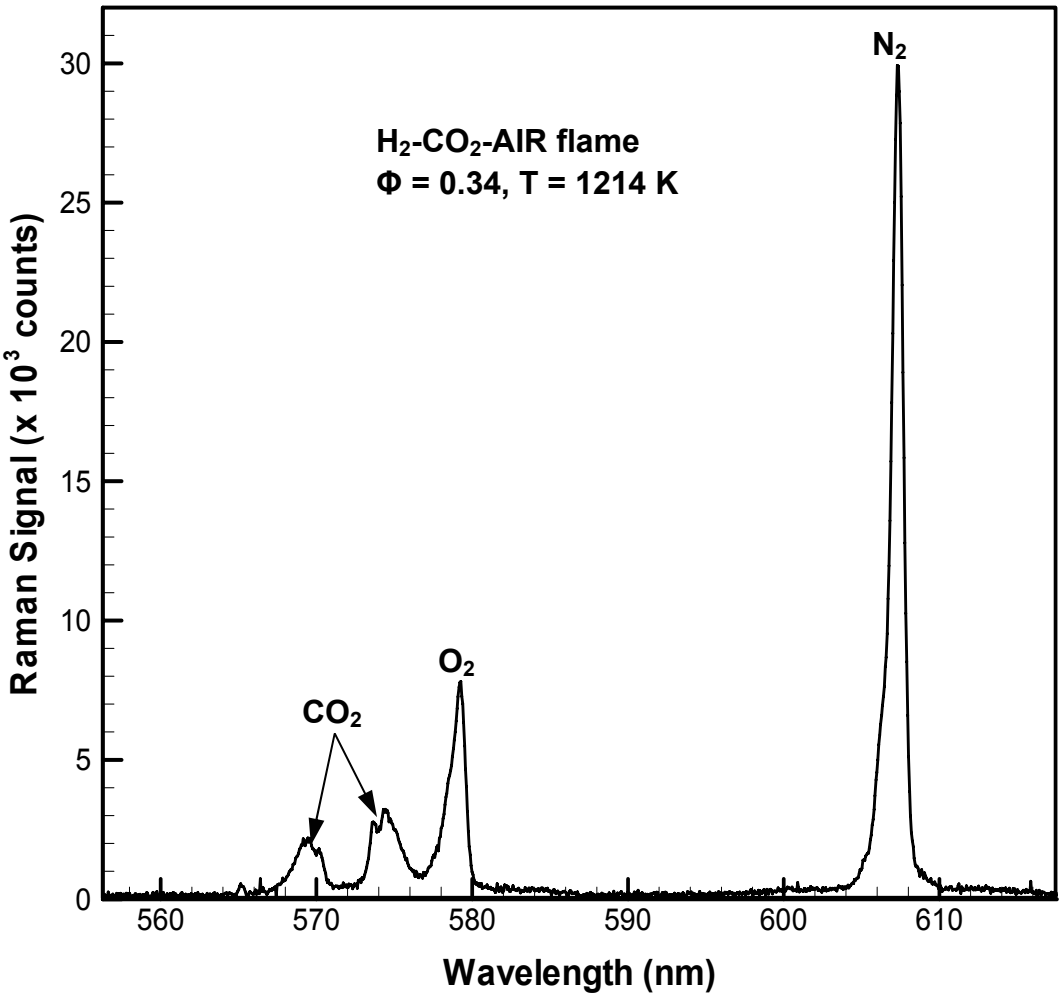

Figure 12 Raman spectra of H_2-CO_2-air flame at ϕ = 0.34 showing the overlap between O_2 and CO_2

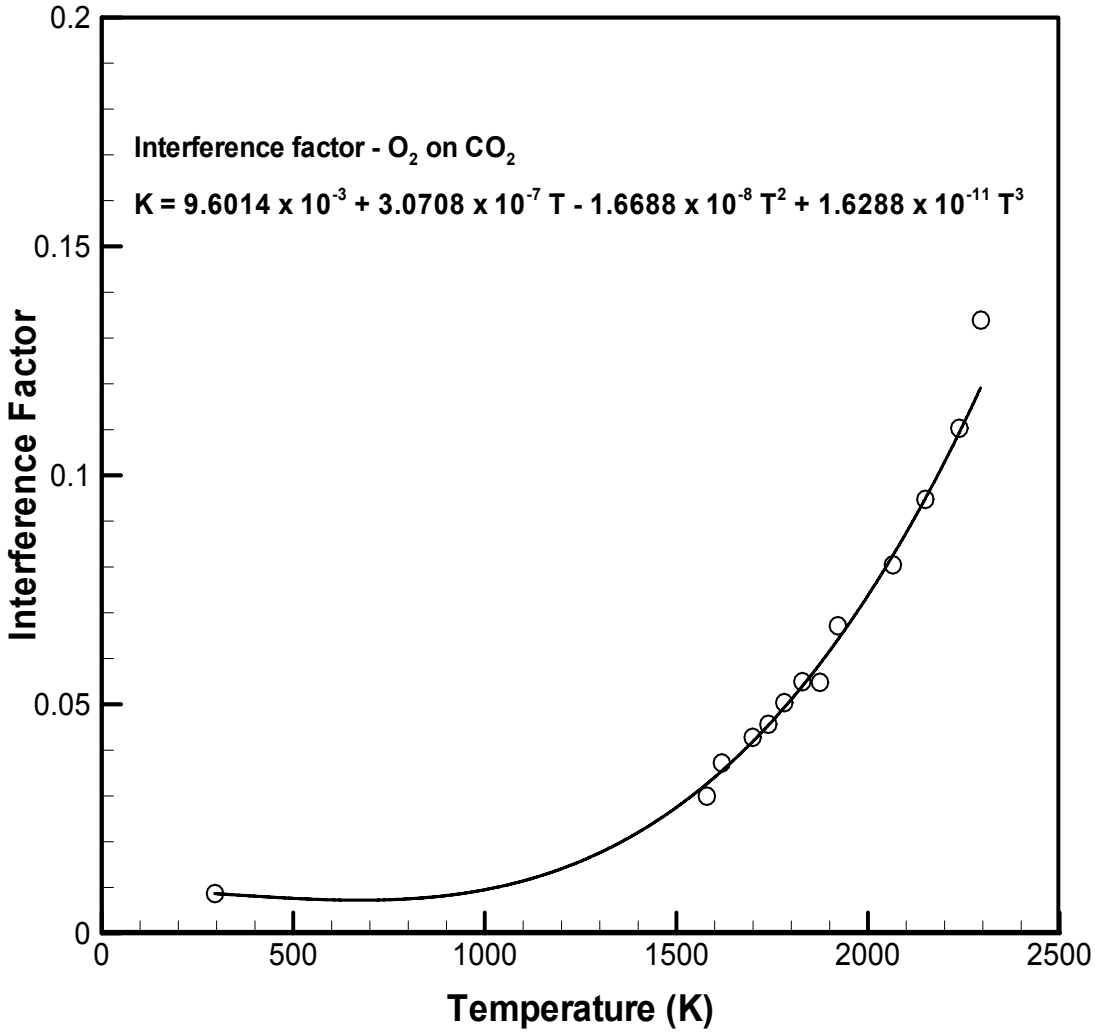

Figure 13 Temperature-dependent interference factor of O_2 on CO_2

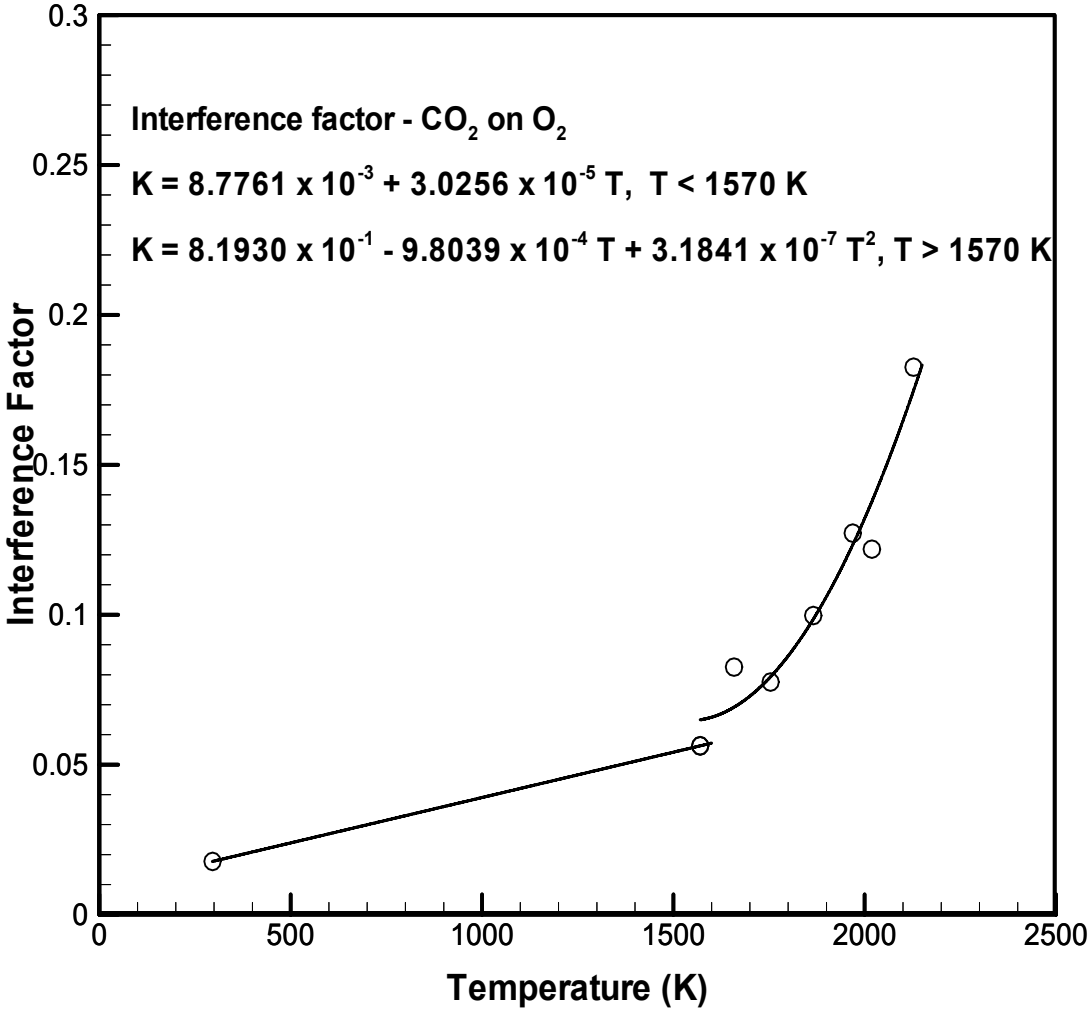

Figure 14 Temperature-dependent interference factor of CO_2 on O_2

signal, and $K_{CO_2-O_2}(T)$, which represents the ratio of the CO_2 signal in the O_2 channel to the total O_2 signal. Figures 13-14 show the interference factors as functions of temperature. In evaluating $K_{CO_2-O_2}(T)$ (Figure 14), a linear fit is used for temperature below 1570 K and second order polynomial fit for temperature above 1570 K.

The calibration factors for CH_4 and C_3H_8 are obtained at room temperature under undiluted and diluted conditions (N_2 is the diluent) due to the difficulty in producing flows with elevated temperature. The temperature dependence of the calibration factors is therefore neglected. This simplification is justified by the good agreement between experimental data and the numerical prediction demonstrated later.

During the experimental data reduction, the number density of the i^{th} species is given by:

$$n_i = C_i(T)\xi_i / E_l \tag{2.3}$$

for H_2, H_2O, N_2, CO, CH_4 and C_3H_8. For O_2 and CO_2, the following expressions are used:

$$n_{CO_2} = C_{CO_2}(T)\left(\xi_{CO_2} - K_{O_2-CO_2}(T)\times \xi_{O_2}\right)/E_l \tag{2.4}$$

$$n_{O_2} = C_{O_2}(T)\left(\xi_{O_2} - K_{CO_2-O_2}(T)\times \xi_{CO_2}\right)/E_l \tag{2.5}$$

Due to the temperature dependence of the calibration factor, an iterative procedure is employed. Starting with a guessed initial temperature, the number densities of each major species are evaluated using Eq. 2.3-2.5. The temperature is then re-evaluated according the ideal gas law and the iteration continues till the temperature difference between two consecutive iterations meets the converging criteria.

The uncertainty of the polynomial fit of the calibration factors is checked by com-

paring the calculated values and the Raman-reduced data. The validity of the data reduction procedure can also be confirmed by such a practice. In Figure 15, the profiles of H_2, H_2O, N_2 and O_2 concentrations and temperature from both the EQUIL calculation and Raman data reduction are plotted as functions of the equivalence ratio. A ± 3% uncertainty is displayed as error bars on the experimental data of the calibration flame. It is shown that the uncertainty estimate of ± 3% accurately captures the experimental uncertainty. The uncertainties of the mass flow meters used in the calibration and experiment are ± 1% of full scale. The accuracy of the temperature measurement is estimated to be less than ± 4% for hydrocarbon flames based on the RMS value of the measured temperature in the product zone.

Since the Raman scattered light is recorded along a line by the camera during the tubular burner experiments and later segmented to sections representing different location points in space, the solid angle regarding to the collection optics changes from point to point. More importantly, sections at different spatial locations are sometimes partially obscured by the burner nozzle to different extents. Such an effect is often termed the shadowing effect. A mathematical estimate of the shadowing effects can not give a satisfactory result and therefore an experimental approach is adopted. During the experiment, the N_2 signal at room temperature condition is recorded for every section along the Raman line and compared with the overall N_2 calibration signal to determine the shadowing factor for each section. The shadowing factor is used in data reduction to interpret the correct Raman signal for each species. A similar effort using the O_2 signal shows that there is no

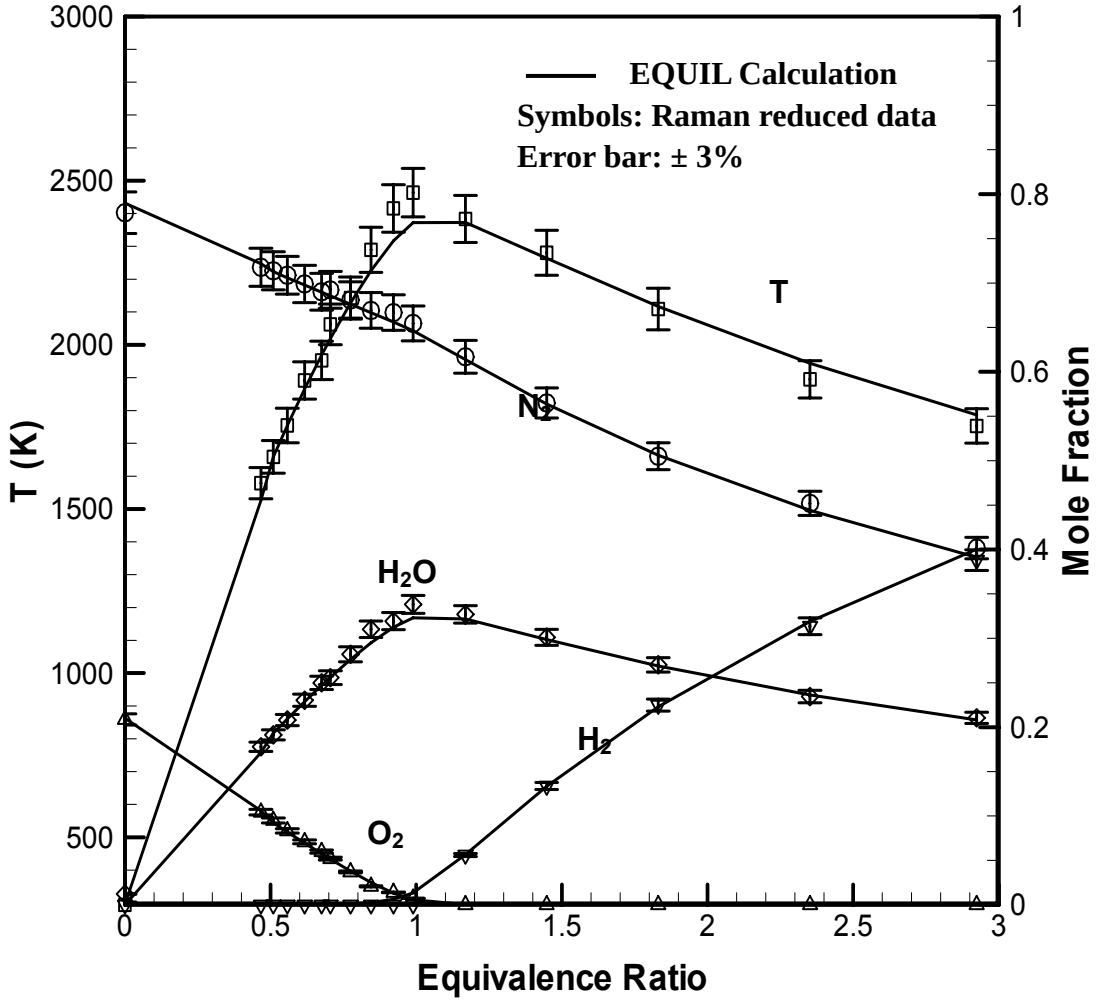

Figure 15 Comparison between calculated and Raman-reduced temperature and major species concentration of H_2-air calibration flames showing the uncertainties

wavelength dependence of the shadowing effect. The N_2 signal is used to account for the shadowing effects throughout this work.

The opposed tubular burner

Burner Configuration

The tubular burner used in a previous study (Mosbacher et al. 2002) is modified by installing a secondary porous nozzle (inner nozzle, 20 mm high, 6.4 mm in dia.) along the center axis that issues one of the reactants outwardly in the radial direction (Figure 16). The other reactant flows inwardly from the outer contoured nozzle (20mm high, 30 mm in diameter). The inward and outward flowing reactants form a stagnation surface and react. The combustion products exit the tubular burner in the axial direction. By changing the exit velocities of the reactants, we can control the flame location, i.e. the curvature that the flame is experiencing. Flows from both the outer nozzle and inner nozzle are accompanied by N_2 co-flows to keep the burner cool and maintain a constant inlet temperature. The burner has three optical ports perpendicular to each other along the periphery to allow flame imaging and laser-based non-intrusive diagnostics.

Governing Equations

A one-dimensional governing equation has been previously derived for the steady opposed tubular flame (Dixon-Lewis et al. 1990; Wang et al. 2006b), where temperature,

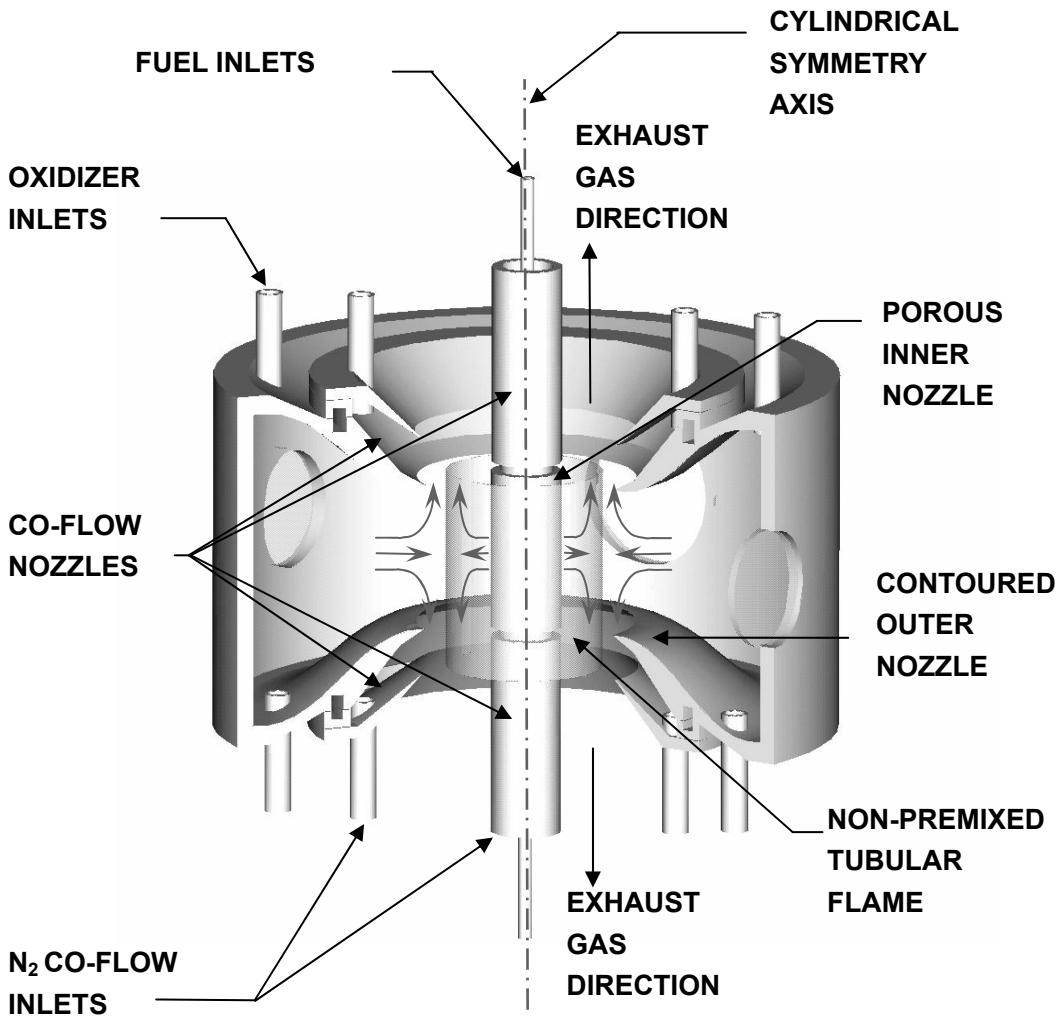

Figure 16 Schematic of the opposed tubular burner

species mass fraction, density and the transport coefficients (viscosity, thermal conductivity and diffusion coefficients) are assumed to be functions of radial coordinates alone. The other assumptions evoked include small Mach number and negligible body force. The complete set of equations is listed below:

The continuity equation

$$\frac{\partial(r\rho U)}{\partial z}+\frac{\partial(r\rho V)}{\partial r}=0 \tag{2.6}$$

is satisfied exactly if a stream function $\psi(z,r)=zf(r)$ is defined so that

$$-\frac{\partial\psi}{\partial r}=r\rho U=-z\frac{df}{dr} \text{ and } \frac{\partial\psi}{\partial z}=r\rho V=f \tag{2.7}$$

where the axial velocity, U is linearly proportional to z and the radial velocity V is a function of r only. The momentum equations in the z and r directions are given, respectively, as

$$f\frac{dF}{dr}=\frac{d}{dr}\left(\mu r\frac{dF}{dr}\right)-r(J+\rho F^2) \tag{2.8}$$

$$\frac{dJ}{dr}=0 \tag{2.9}$$

where $F=-(df/dr)/(\rho r)$ and the constant pressure eigenvalue J is equal to $(1/z)\partial p/\partial z$. The energy and species conservation equations are:

$$\rho C_p V\frac{dT}{dr}+\frac{1}{r}\frac{d}{dr}\left(-r\lambda\frac{dT}{dr}\right)+\rho\frac{dT}{dr}\left(\sum_i C_{pi}Y_iV_i'\right)+\sum_i h_i\varpi_i=0 \tag{2.10}$$

$$\rho V\frac{dY_i}{dr}+\frac{1}{r}\frac{d}{dr}\left(r\rho Y_iV_i'\right)-\varpi_i=0 \tag{2.11}$$

where the diffusion velocities are given by the multicomponent formulation:

$$V_i' = \frac{1}{X_i W} \sum_{j \neq i} W_j D_{i,j} \frac{dX_j}{dr} - \frac{D_i^T}{\rho Y_i} \frac{1}{T} \frac{dT}{dr} \tag{2.12}$$

The boundary conditions are:

$f = R_1 \rho_1 V_1$, $F = 0$, $T = T_1$, $Y_i = Y_{i1}$ at $r = R_1$

$f = R_2 \rho_2 V_2$, $F = 0$, $T = T_2$, $Y_i = Y_{i2}$ at $r = R_2$

A similarity solution for the above governing equations is sought by using a modified OPPDIF program with detailed chemical reaction mechanisms and complex transport formulations (Mosbacher et al. 2002), where the ideal gas law is evoked. Simulation results from the program are used to compare with the experimental data throughout this work.

CHAPTER III

NON-PREMIXED TUBULAR FLAMES: HYDROGEN

Introduction

Premixed, non-premixed, and partially-premixed laminar flames are all subject to the influence of stretch (Seshadri et al. 1985; Law 1988a). Most of the quantitative work has focused on stretched planar flames produced by opposed-jet burners, where the stretch is generated by aerodynamic straining only. Theoretical (Libby et al. 1989), numerical (Smooke and Giovangigli 1990; Nishioka et al. 1991; Ju et al. 1998) as well as experimental (Kobayashi and Kitano 1989; Ishizuka 1993; Ogawa et al. 1998) investigations on tubular flames with constant curvature have been conducted, but were limited to premixed flames. Studies of curvature effects on non-premixed laminar flames were carried out on vortex flames formed by perturbing the flat opposed-jet flame with either a syringe tube (Takagi et al. 1996b; Katta et al. 1998; Yoshida and Takagi 1998; Lee et al. 2000; Yoshida and Takagi 2003) or a bluff body (Finke and Grünefeld 2000) and on the flame tip of the Burke-Schumann flame (Ishizuka 1982; Im et al. 1990; Greenberg and Grodek 2003). These flames all suffered from a non-constant curvature, which makes the effects of curvature hard to identify.

To circumvent these difficulties, an optically-accessible tubular burner with an added nozzle at the center axis as a second, radially-outwardly flowing reactant source is intro-

duced. Non-premixed and partially-premixed flames that feature a controllable curvature can be generated. The detailed flame structure of constant-curved, N_2-diluted H_2 versus air non-premixed tubular flames is studied for the first time using the non-intrusive visible Raman spectroscopy technique. Flame temperature and major species mole fractions are recorded with high spatial resolution. An Oppdif code has been modified to model tubular flames (Mosbacher et al. 2002). Numerical simulation with complex chemistry and detailed transport is carried out to compare with the measurement. This comparison validates the numerical model. We then use the numerical model to show that the flame temperature is greatly affected by curvature.

Comparison between opposed tubular and opposed-jet flames shows that the concave curvature causes the flame temperature to decrease when $L_e < 1$. This is confirmed by our recent numerical studies of the tubular non-premixed flames with a different burner configuration (Wang et al. 2006b). Observation of tubular flame images with different fuel types over a range of Lewis numbers supports the discovery that concave curvature in the fuel promotes reaction when $L_e > 1$ and retards reaction when $L_e < 1$. The opposite will occur for convex curvature in the fuel. The extinction measurements confirm these effects of curvature on the flame temperature and structure.

Stretch Rate

Mathematically, the tubular flame can be formulated into a set of ordinary differential equations (Dixon-Lewis et al. 1990), i.e. the velocity, temperature and species concentra-

tion are all functions of the radial coordinate only. The flame experiences a finite positive stretch in the axial direction. It has been shown by (Seshadri and Williams 1978) that the local stretch rate for the opposed-jet burner is a linear function of the distance from the exit nozzle on either side of the stagnation plane. This stretch rate peaks at the stagnation plane, where the fuel-stream side value can be calculated from:

$$k = \frac{2V_f}{L}(1 + \frac{V_o}{V_f}\sqrt{\frac{\rho_o}{\rho_f}}) \tag{3.1}$$

where L is the separation distance of the two jets. Subscripts o and f denote oxidizer and fuel stream, respectively.

Based on a similar argument, the fuel-stream side stretch rate at the stagnation surface of the non-premixed tubular flame takes the following form (Wang et al. 2006b):

$$k = \pi\frac{V_f}{R_f}(\frac{V_o R_o / (V_f R_f)\sqrt{\rho_o/\rho_f} - 1}{R_o^{\,2}/R_f^{\,2} - 1}) \tag{3.2}$$

This formula applies to fuel issued from the inner nozzle as well as from the outer nozzle. Comparisons of opposed-jet planar and opposed tubular non-premixed flames are carried out subsequently based on the stretch rates defined by the above equations.

Given the geometry of this burner, it is necessary to clarify that for fuel issued from the inner nozzle cases, the flame surface is concave toward the fuel stream. On the other hand, for fuel issued from the outer nozzle cases, the flame surface is convex to the fuel stream. To simplify the discussion, the convex and concave flames are used throughout this paper referring to curvature of the flame front towards the fuel stream.

Results and Discussion

The Raman scattering system described in Chapter II is employed to performed detailed structure study. A set of representative Raman spectra at different radial locations is shown in Figure 17 for 15% H_2/N_2-air flame at $k = 91\ s^{-1}$. Strong laser scattering from the inner nozzle is observed on the upstream side of the beam, so only data on the shadowing side of the inner nozzle are used.

In the first set of experiments, 15% H_2 diluted by 85% N_2 against air flames at various stretch rates are investigated. The exit velocities of the inner and outer nozzle are matched such that the calculated cold flow stagnation surface is located at $R_s = 6.5$ mm. The peak flame temperature location is very close to the stagnation surface for all the stretch rates studied, and therefore the tubular flames produced are experiencing a constant curvature. The near extinction behavior of CH_4 and C_3H_8 diluted in N_2 vs. air flames are also studied. Comparison of the experimental data and numerical simulations reveals the effects of curvature.

The Opposed Tubular Flame

The tubular burner (Mosbacher et al. 2002) is modified by installing a secondary porous nozzle (inner nozzle, 20 mm high, 6.4 mm in dia.) along the center axis that issues one of the reactants outwardly in the radial direction. The other reactant flows inwardly from the outer contoured nozzle (20mm high, 30 mm in diameter). The inward and outward flowing reactants form a stagnation surface and react. The combustion products exit

the tubular burner in the axial direction. By changing the exit velocities of the reactants, we can control the flame location, i.e. the curvature that the flame is experiencing. Flows from both the outer nozzle and inner nozzle are accompanied by N_2 co-flows to keep the burner cool and maintain a constant inlet temperature. The burner has three optical ports perpendicular to each other along the periphery to allow flame imaging and laser-based non-intrusive diagnostics.

At low stretch rates, non-premixed concave flames are produced with 15% H_2/N_2 fuel issued from the inner nozzle. An image of this concave flame at stretch rate k = 105 s^{-1} taken by an IR sensitive ICCD camera is shown in Figure 18. The inset on the top left corner shows the OH* chemiluminescence image. The bright flame front is the emission from electronically excited OH radicals. The flame is very symmetric from left to right and circular when viewed from the top. Although the flame appears to be slightly curved in the axial direction, this curvature is insignificant compared to the curvature in the radial direction and can be neglected. The one-dimensional simplification in (Dixon-Lewis et al. 1990) is applicable to this flame.

However, when the 15% H_2/N_2 fuel is issued from the outer nozzle, no circular convex flames can be formed. The flame surface has several wrinkles around the perimeter for all stretch rates. Because the laser beam passes through these wrinkled flame fronts, Raman-derived flame temperature data show multiple temperature peaks. At the highly wrinkled flame front, the curvature is smaller than 6.5 mm. Cellular structures are observed when viewing from the side window in the radial direction. The 3-D nature of the convex

flame also makes the one-dimensional laser diagnostic less meaningful. As a result, Raman measurement results are only presented for the symmetrical concave flame in the following discussion.

Hydrogen Tubular Flame Structure

Non-premixed tubular concave flames (15% H_2/N_2 vs. air) with stretch rates ranging from k = 30 to 242 s^{-1} are measured using Raman spectroscopy. A comparison of various chemical kinetic mechanisms with the experimental data at stretch rate k = 75 s^{-1} is shown in Figure 19. The mechanisms used are from Mueller et al. (Mueller et al. 1999), Peters et al. (Peters and Rogg 1993) and GRIMech3.0 (Smith et al. 2000). In the calculations, the diffusive velocities are evaluated using either the multi-component or mixing averaged formulation. Thermal diffusion is included in all calculations. The mechanisms from Yetter et al. (Yetter et al. 1991), Li et al. (Li et al. 2003) and Mueller et al. give almost identical results and therefore only calculation from Mueller mechanism is shown. The Peters mechanism gives the highest temperature prediction, while the GRIMech3.0 with mixing-averaged diffusion predicts a narrower reaction zone. The Mueller and GRIMech3.0 mechanisms with multi-component diffusion give almost identical predictions and the lowest peak temperatures. The Peters mechanism using multi-component formulation predicts extinction at this experimental condition. All mechanisms generally agree well with the experimental data (shown as closed circles). The subsequent numerical calculations are all performed using the Mueller mechanism.

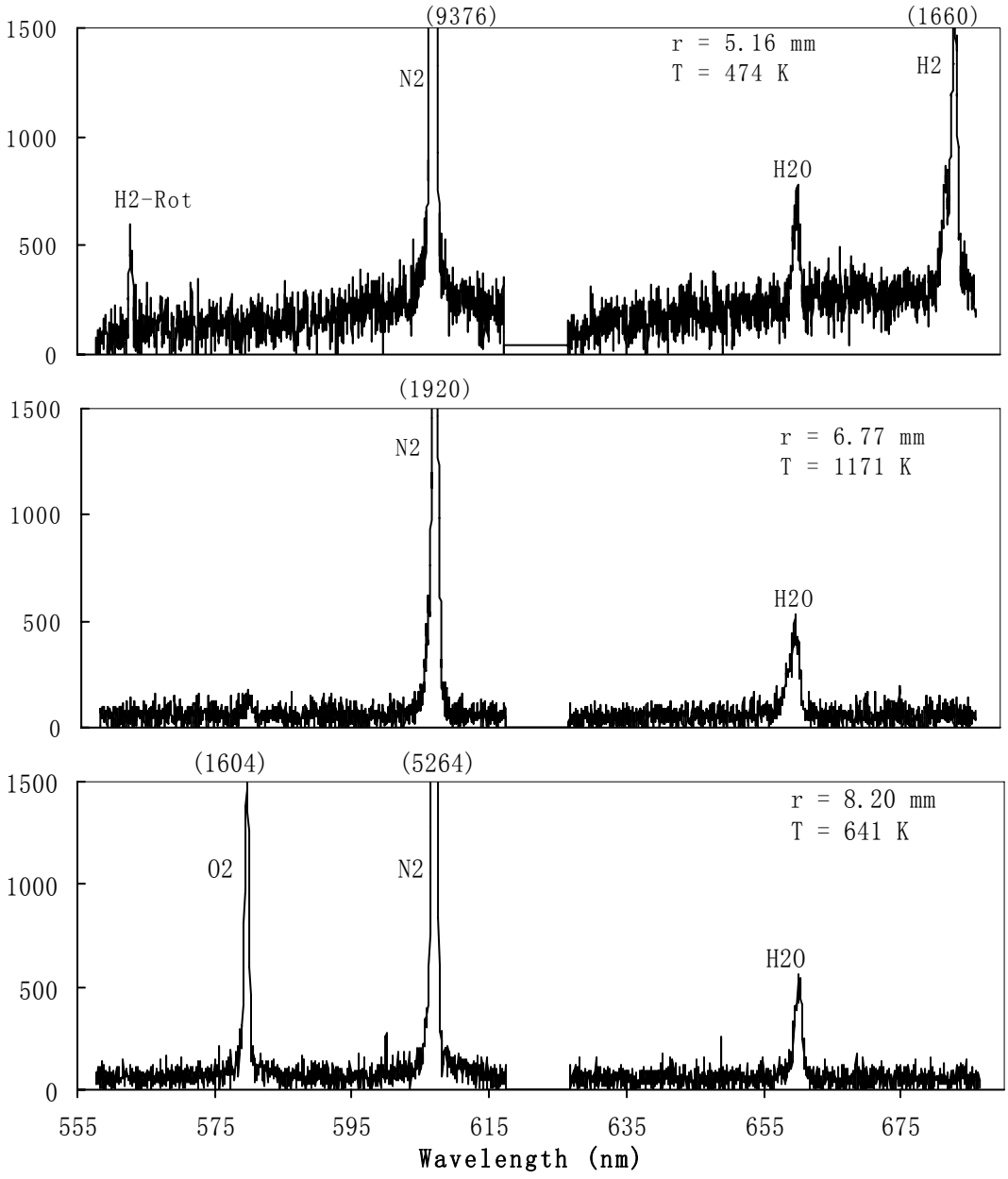

Figure 17 Representative Raman spectra of a k = 91 s^{-1}, 15% H_2/N_2 vs. air non-premixed tubular flame at four radial locations as measured from the symmetry axis.

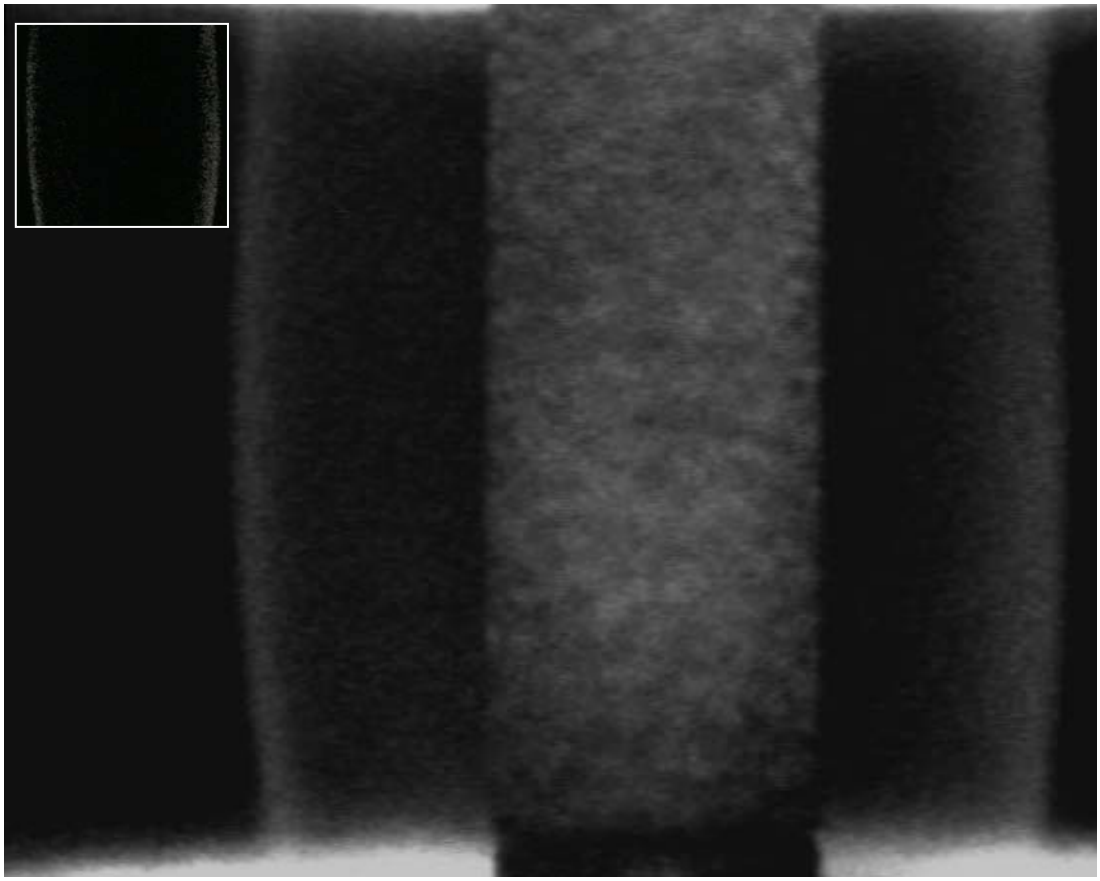

Figure 18 Image of non-premixed tubular flame at k = 105 s^{-1} showing symmetric flame structure. The inset shows the OH* chemiluminescence image of the same flame.

Figures 20-23 show the measured and calculated temperature and major species mole fraction profiles for k from 60 s^{-1} to 104 s^{-1} in radial and mixture fraction coordinates. The mixture fraction Z is defined as (Williams 1985)

$$Z = \frac{X_{o,2}/W_2\nu_o + X_f/W\nu_f - X_o/W\nu_o}{X_{o,2}/W_2\nu_o + X_{f,1}/W_1\nu_f} \tag{3.3}$$

where ν_i is the stoichiometric coefficient of i^{th} species. The stoichiometric mixture fraction Z_{st} is 0.70, obtained by setting the local mole fraction of fuel and oxidizer to zero at the stoichiometric location.

It is seen that the computed profiles agree well with the experimental measurements. The measured flame surface locations, determined by the maximum temperature location, are close to r = 6.8 mm, which indicates that these flames have the same curvature. The broadening of the reaction zone at higher stretch rates is due to the flame fluctuation. An improvement on the burner is needed to further stabilize the flame. At stretch rates lower than 60 s^{-1}, the measured temperature is lower than prediction due to the heat loss to the inner nozzle.

Figure 24 shows the variations of the calculated maximum flame temperature and flame thickness of the tubular and opposed-jet flat flames with stretch rate. The flame thickness is defined as the FWHM (Full Width at Half Maximum) of the temperature profile. The dots shown in the figure are experimental temperature data with an estimated uncertainty of 3%. The corresponding adiabatic flame temperature T_{ad} = 1180 K is shown as the horizontal line in the figure. While both flame temperatures decrease with increasing stretch rate, a

temperature difference of ~100 K is observed between the two flames showing the effects of curvature. For tubular flames with Lewis number less than one, the preferential diffusion coupled with concave curvature causes the flame temperature to decrease. As a result, the tubular flames extinguish at a much lower stretch rate than the opposed-jet flames.

Tubular Flame Extinction

Extinction experiments are conducted on the concave tubular flames using three types of fuel: H_2, CH_4 and C_3H_8. Different N_2 dilution ratios for these fuels are used to avoid extinction. To achieve extinction, the air flow is gradually increased and the fuel flow rate is kept constant. For 15% H_2/N_2, as the stretch rates are increased above 105 s^{-1}, cellular structures are observed at the flame front. The flame automatically changes its orientation of curvature from concave to convex to avoid extinction. Figure 25-(1) shows the image of the tubular flame at stretch rate $k = 210$ s^{-1}, where the cellular structure is identified as the bright and dark regions. Several cells (the number depends on the stretch rate) with openings around the perimeter are observed when viewing the flame in the axial direction. Figure 25-(2) shows the flame emission image taken from the top of the burner, where three flame wings are clearly seen with the fourth one blocked from view by the inner nozzle. One can infer that the convex flame with Lewis number less than one has a higher temperature and thus higher extinction stretch rate. In other words, convex curvature promotes combustion and retards extinction when the Lewis number is less than one. As a

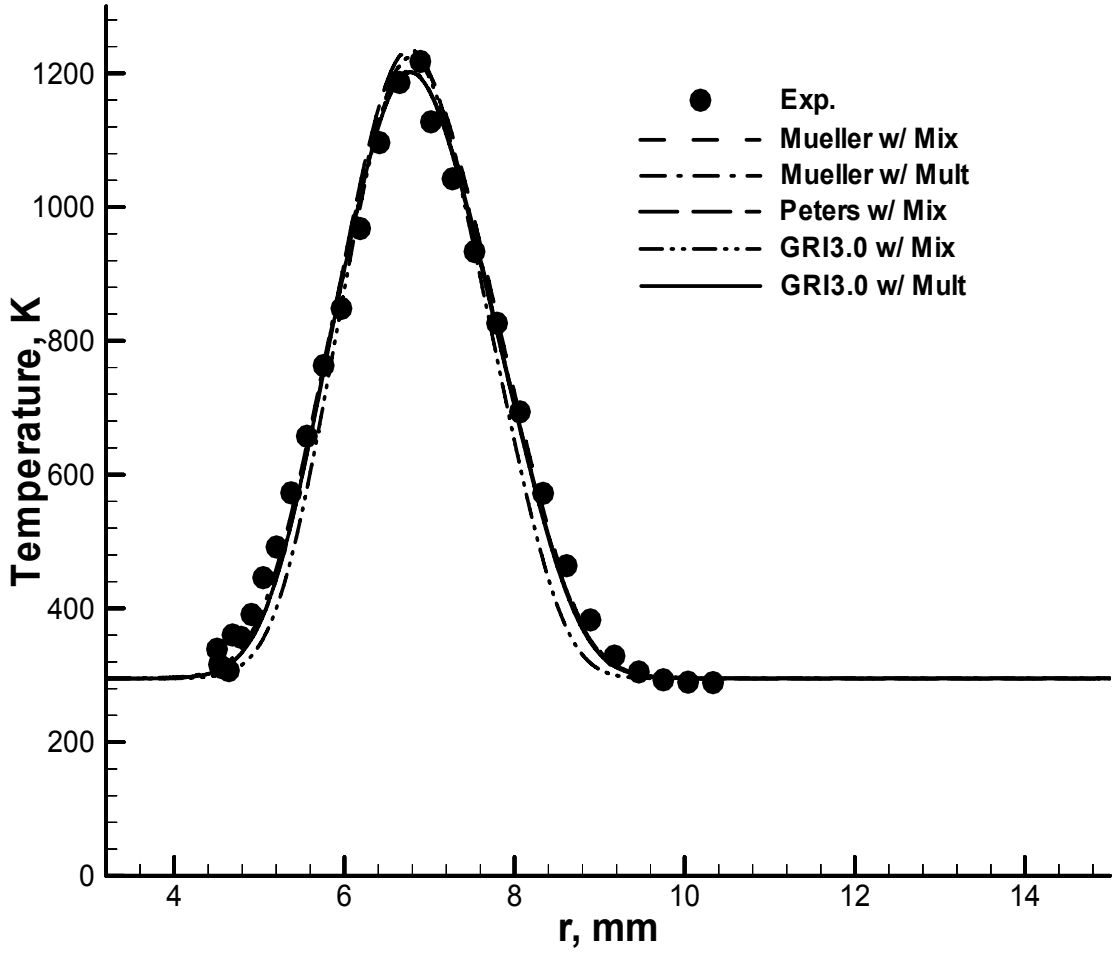

Figure 19 Comparison of Raman-derived data and calculations using different mechanisms of a 15% H_2/N_2 vs. air flame at k = 75 s^{-1}.

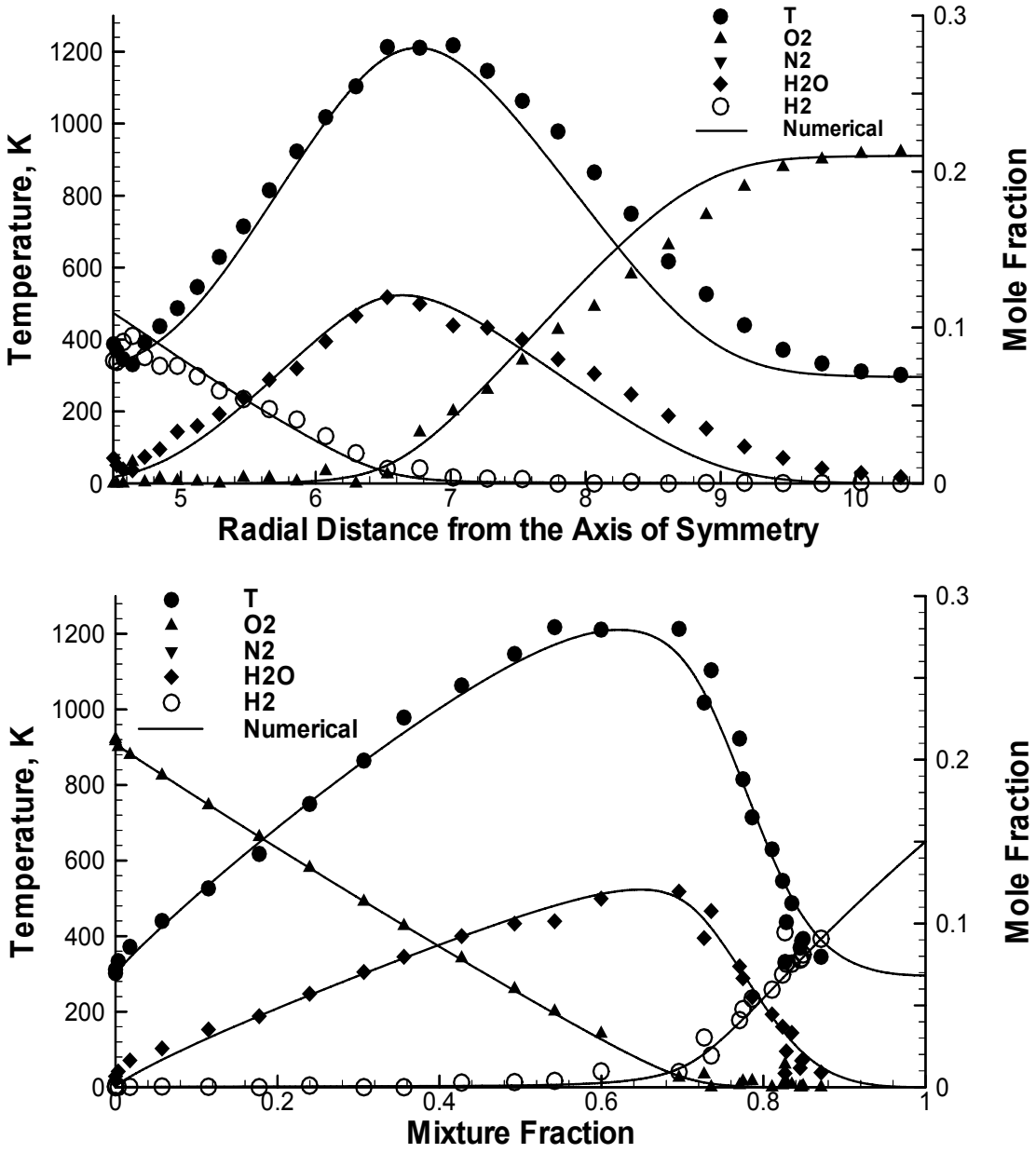

Figure 20 Measured and calculated temperature and major species profiles for a 15% H_2/N_2 vs. air non-premixed flame at k = 60 s^{-1} in both radial and mixture fraction coordinates

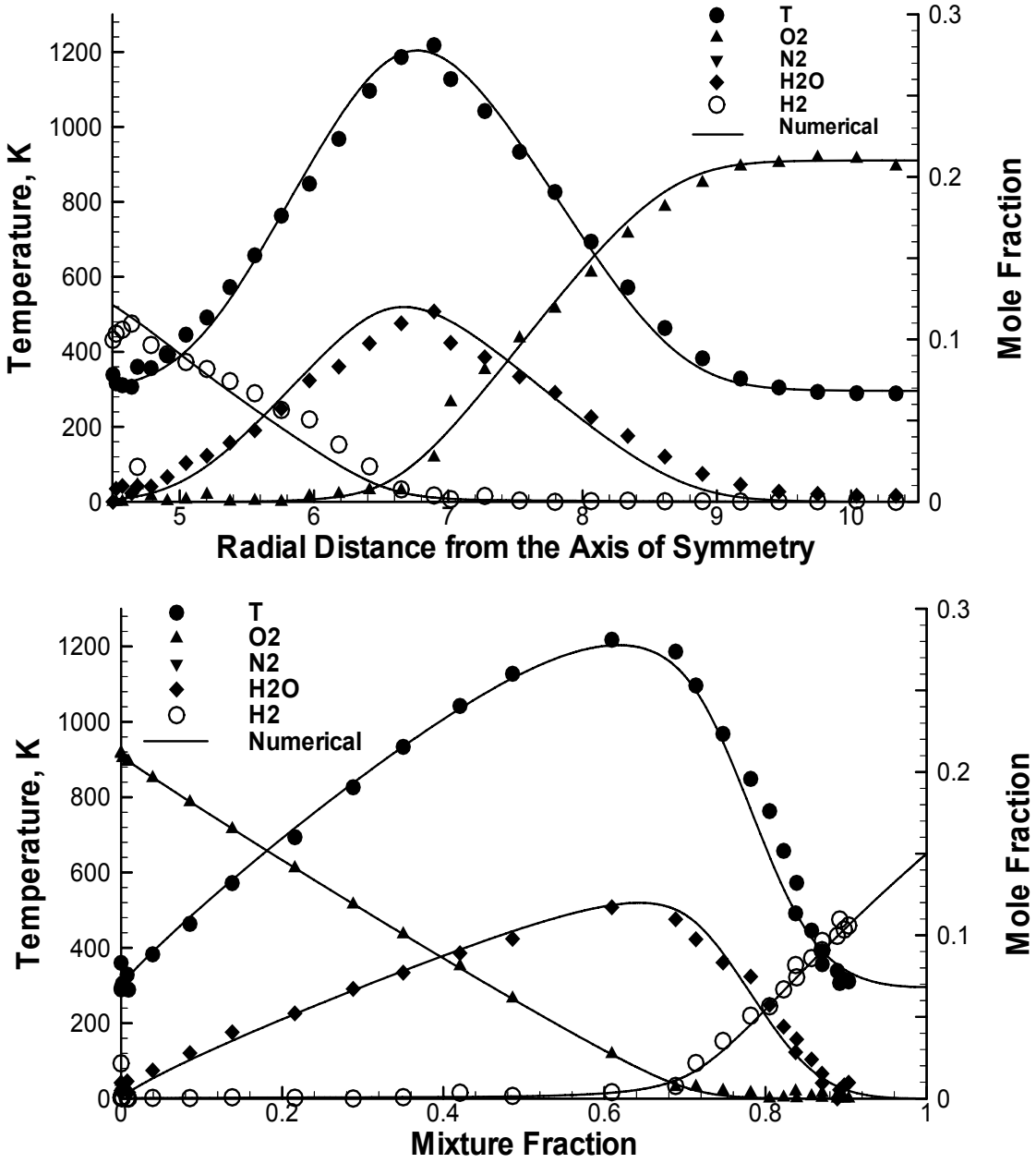

Figure 21 Measured and calculated temperature and major species profiles for a 15% H_2/N_2 vs. air non-premixed flame at k = 75 s^{-1} in both radial and mixture fraction coordinates

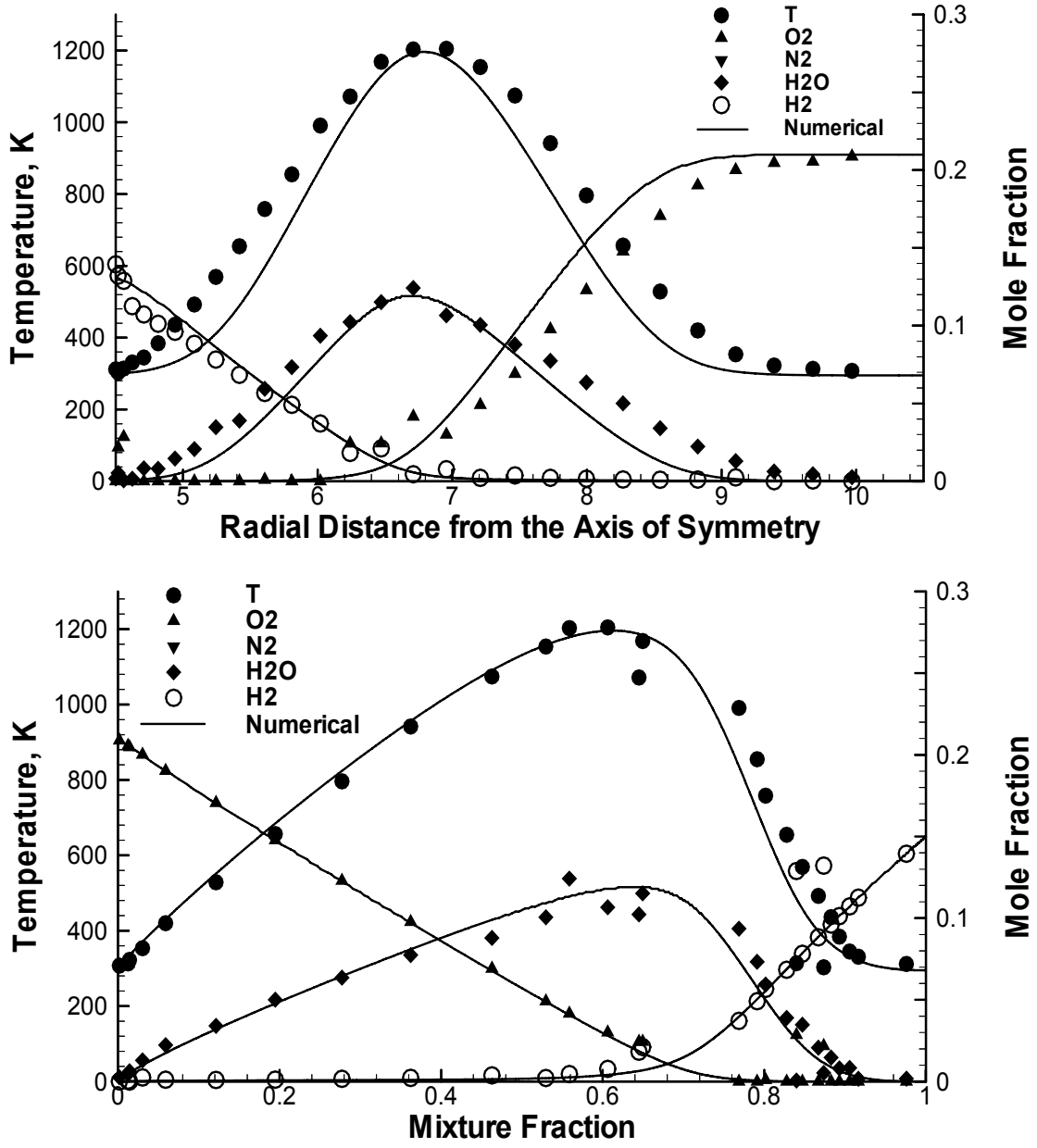

Figure 22 Measured and calculated temperature and major species profiles for a 15% H_2/N_2 vs. air non-premixed flame at k = 91 s^{-1} in both radial and mixture fraction coordinates

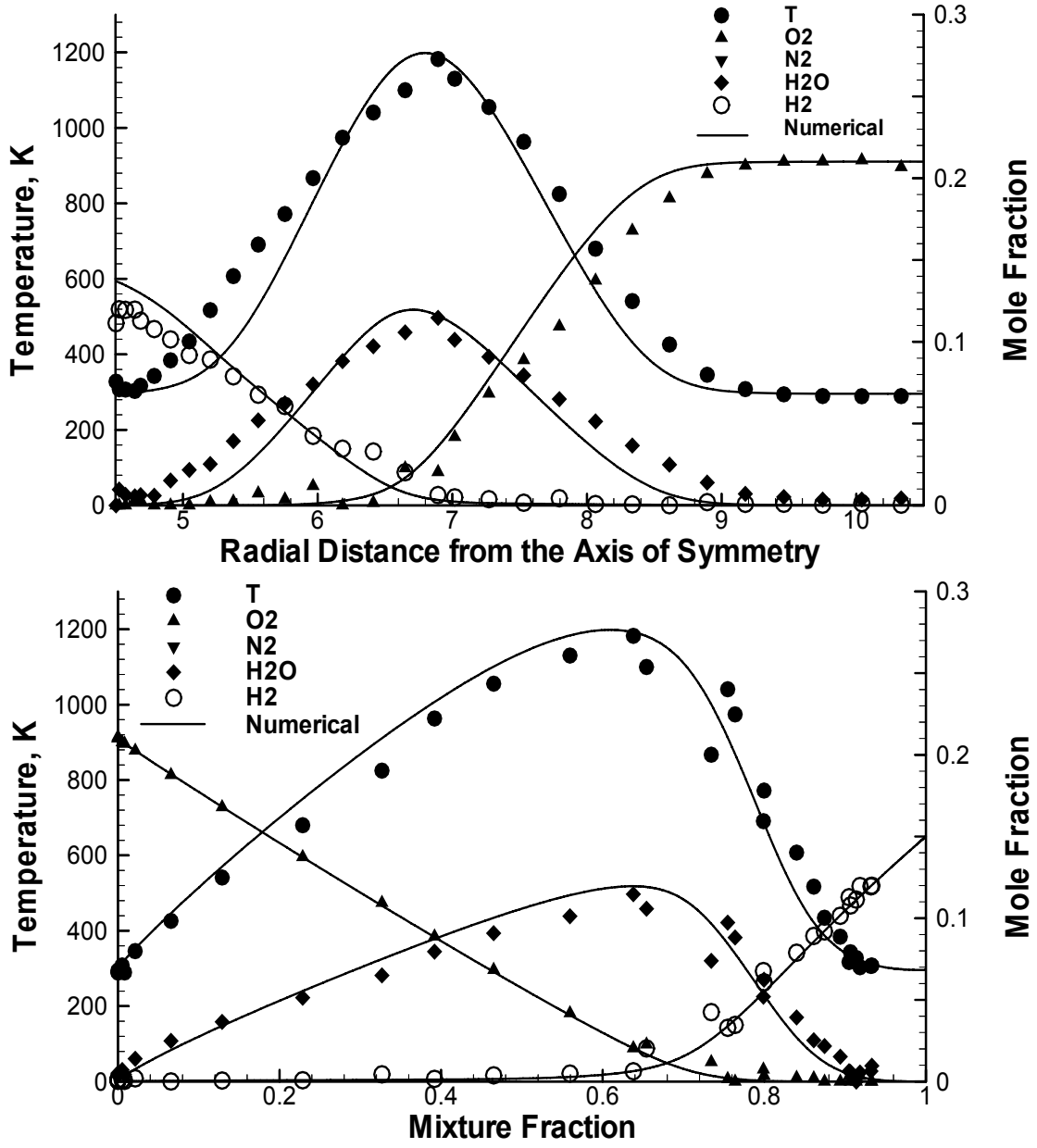

Figure 23 Measured and calculated temperature and major species profiles for a 15% H_2/N_2 vs. air non-premixed flame at k = 104 s^{-1} in both radial and mixture fraction coordinates

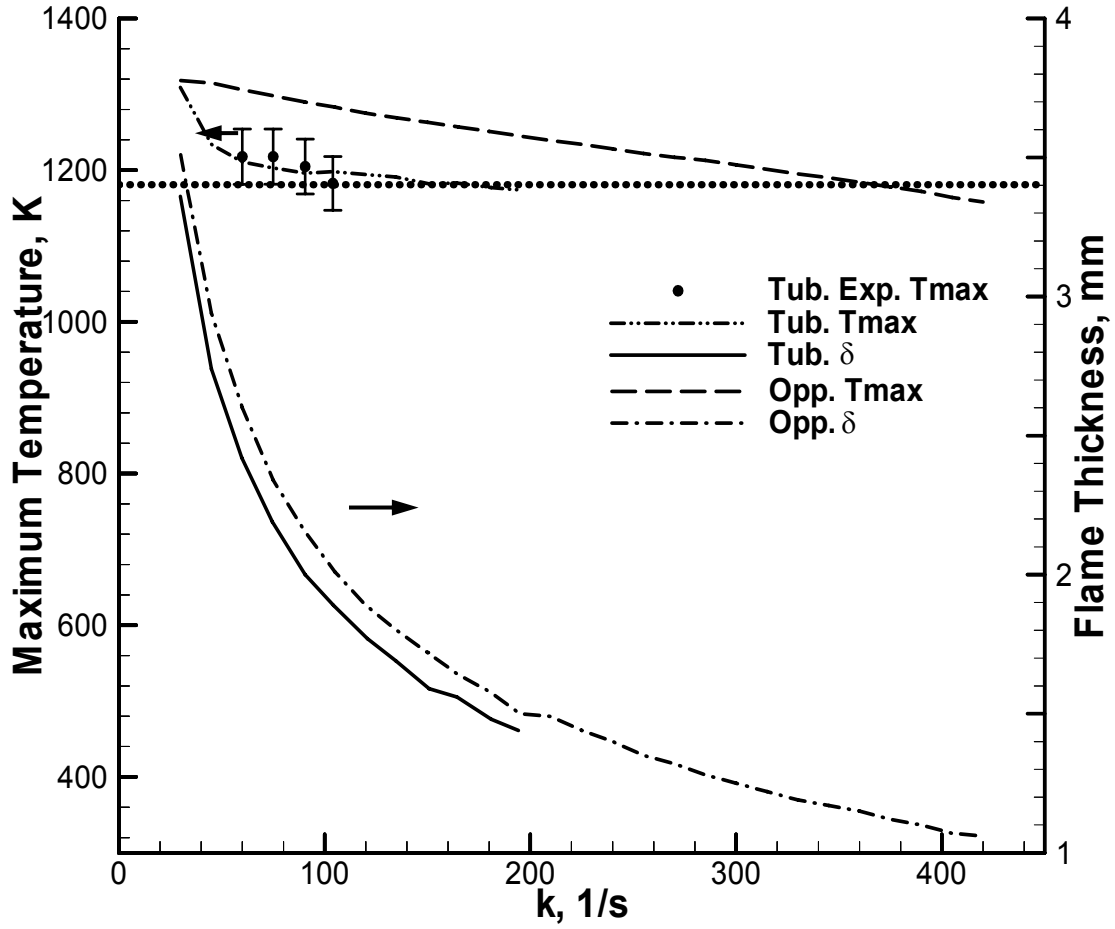

Figure 24 Comparison of the maximum flame temperature and flame thickness for 15% H2/N2 vs. air tubular and opposed-jet flames.

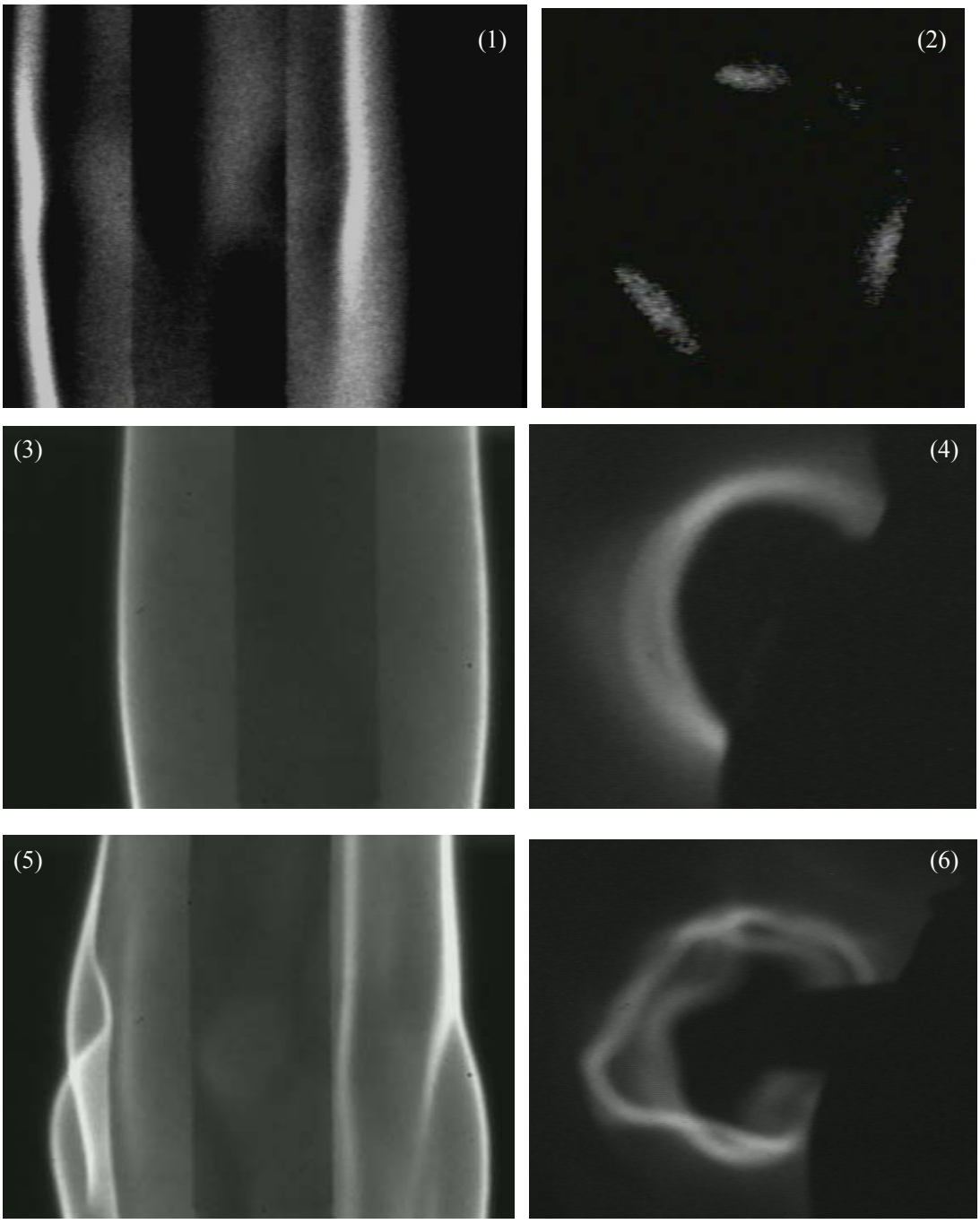

Figure 25 Images of non-premixed tubular flames (1) side view (2) top view of 15% H_2/N_2 vs. air flame at k = 210 s^{-1}; (3) side view (4) top view of 26% CH_4/N_2 vs. air flame at k = 166 s^{-1}; (5) side view (6) top view of 15% C_3H_8/N_2 vs. air flame at k = 161 s^{-1}. Top view images are partially blocked by the inner nozzle.

result, the 1-D tubular flame code developed previously (Dixon-Lewis et al. 1990; Mosbacher et al. 2002) is unable to give an accurate prediction of the extinction limit. Experimentally, 9.8% H_2/N_2 vs. air flame is extinguished at $k = 240\ s^{-1}$ and $R_s = 5.3$ mm. The calculated extinction fuel dilution ratio at this stretch rate is 15%, much higher than 9.8%. This, again, demonstrates that the convex curvature helps to stabilize the flame and therefore extends the extinction limit for hydrogen fuel ($L_e < 1$).

However, this observation does not apply to the near-extinction methane flames. The flame is fairly circular throughout the combustible region until extinction is reached. Figure 25-(3) shows an image of a non-premixed tubular flame of 26% CH_4/N_2 against air at $k = 166\ s^{-1}$ with the extinction stretch rate being ~205 s^{-1}. The Lewis number of the fuel stream is close to one, and yet no preferential curvature is observed. The flame is still circular as seen from the top view image in Figure 25-(4). The 1-D code is capable of predicting the structure of this flame. Two sets of extinction measurements with different curvatures (R_s) are conducted. The measured and predicted extinction stretch rates show very good agreement (Table 3).

Non-premixed C_3H_8/N_2 vs. air tubular flame also shows the preferential curvature property. Different from the hydrogen flame, the propane flame prefers concave curvature. Cellular structures are seen for all stretch rates throughout the combustible range. When viewed along the axial direction, the flame front appears to be wrinkled. Figure 25-(5) shows the image for a 15% C_3H_8/N_2 vs. air flame at $k = 161 s^{-1}$ and $R_s = 6.3$ mm. Figure 25-(6) shows the wrinkled flame front as viewed from the axial direction. The measured

extinction stretch rate is much higher than the calculated value due to the preferential curvature effects. One can conclude that the concave curvature promotes combustion and retards extinction for propane fuel ($L_e > 1$).

Table 3 Measured and calculated extinction limits

Fuel	X_{fuel}	R_s[a], mm	k, s^{-1}	
			Exp.	Comp.
CH_4	0.261	5.13	218	205
	0.258	5.18	214	203
	0.222	6.42	133	139
	0.220	6.45	132	132

a: Radius of the stagnation surface

Conclusion

Non-premixed tubular flames are established using a uniquely-designed opposed tubular burner for the first time. Concave flames using 15% H_2 diluted with N_2 against air are studied with laser-induced Raman scattering at stretch rates ranging from 30 to 242 s^{-1}. Due to the heat loss to the inner nozzle at low stretch rates and the appearance of cellular structures at high stretch rates, only data for moderate stretch rates are presented. The experimental data and numerical predictions agree very well. The numerical model is validated by such a comparison. The peak flame temperature of the non-premixed concave tubular flame is ~100 K lower than its opposed-jet counterpart due to the effects of concave curvature. This indicates that the curvature concave towards the fuel hinders combustion

when $L_e < 1$.

This conclusion is further proved by the flame behavior at near-extinction conditions. Cellular structures are observed for H_2/N_2 vs. air near-extinction tubular flames at large stretch rates. Near-extinction behavior of non-premixed nitrogen diluted methane and propane against air flames are compared with their hydrogen counterpart. Flames with unity Lewis number (CH_4) doesn't show the preferential curvature property. The 1-D tubular code is applicable to this flame, which gives an accurate prediction of the extinction limit. Flames with Lewis number larger than one (C_3H_8/N_2) prefer concave curvature, while flames with Lewis number less than one (H_2/N_2) prefer convex curvature. The fact that the hydrogen flames change their direction of curvature from concave to convex automatically confirms that convex curvature promotes combustion and therefore increases the flame temperature when $L_e < 1$. The fact that the propane flames decrease their radii of curvature automatically confirms that concave curvature promotes combustion and therefore increases the flame temperature when $L_e > 1$. As a result, the extinction of these flames ($L_e < 1$ or $L_e > 1$) is retarded to a much higher stretch rate. The 1-D tubular code cannot be applied to these flames due to the existence of the cellular structures near extinction. A more sophisticated 3-D code needs to be developed to study these flames.

CHAPTER IV

NON-PREMIXED TUBULAR FLAMES: HYDROCARBON

Introduction

The effects of stretch on premixed, non-premixed and partially-premixed laminar flames are well understood, based on many years of study (Seshadri et al. 1985; Law 1988a). However, studies on curvature effects are limited and the effects of curvature on flames are not fully understood. Tubular flames allow the investigation of curvature effects in addition to the flame stretch (Ishizuka 1993). There have been many works on premixed tubular flames, either experimental (Ishizuka 1993; Kobayashi and Kitano 1989; Ogawa et al. 1998; Mosbacher et al. 2002), numerical (Kitano et al. 1989; Dixon-Lewis et al. 1991; Nishioka et al. 1991) or theoretical (Libby et al. 1989; Wang et al. 2006b). However, reports on non-premixed tubular flames are extremely rare, primarily because of the difficulties in establishing such a flame (Hu et al. 2007a; Wang et al. 2007). By installing a nozzle along the symmetrical axis of the tubular burner as a second, radially-outwardly flowing reactant source, non-premixed and partially-premixed tubular flames subject to well-controlled aerodynamic straining and flame curvature can be created (Hu et al. 2007a)

As reviewed in detail earlier (Wang et al. 2007), studies of curvature effects on non-premixed laminar flames have been carried out on the flat opposed-jet flame perturbed by a vortex from a pulsed syringe tube (Katta et al. 1998; Lee et al. 2000), by a micro-jet

that is steady (Takagi et al. 1996b) or unsteady (Yoshida and Takagi 1998), by suction (Yoshida and Takagi 2003), and by a small bluff body (Finke and Grünefeld 2000). In addition, the curved flame tip of the Burke-Schumann flame has been investigated (Ishizuka 1982; Im et al. 1990; Takagi et al. 1996a). These flames all suffered from a non-constant curvature and were unsteady in some cases, which make the effects of curvature difficult to identify and structural study infeasible. An opposed tubular burner can circumvent these difficulties. The important features of the opposed tubular burner are: 1) Curvature and flame stretch can be varied independently because their directions are orthogonal to each other. 2) Curvature throughout the flame front is uniform because the diameter of the flame tube is constant at a given condition. 3) The flow field is simple and all quantities can be described as functions of radial location only (Dixon-Lewis et al. 1991; Wang et al. 2006b), which is preferred by both experimentalists and modelers. 4) Both concave and convex curvature can be easily established under well-controlled conditions. Due to these advantages, the opposed tubular burner deserves more attention as a useful tool for fundamental research in combustion science. This study is focused on the structural measurements of the opposed tubular non-premixed flames generated by hydrocarbon fuels as well as understanding the effects of curvature on flames.

Structural studies on hydrogen opposed tubular flames, where the fuel stream Lewis number (Lewis number, Le, is defined as the ratio between the mixture thermal diffusivity and the mass diffusivity of the reactant species) is less than one, have been reported previously (Hu 2007; Hu 2006a). Profiles of temperature and major species concentrations

were measured using laser-induced Raman spectroscopy. It was shown that the effects of curvature coupled with the Lewis number effects are affecting flame properties. It is natural to extend the work to opposed tubular non-premixed flames produced by hydrocarbon fuels (CH_4 or C_3H_8). Together with the previous studies, both the unity and non-unity Lewis number cases are completely covered. Numerical simulations with detailed chemistry carried out in this study are compared with the experimental data. In addition, cross-comparisons between the simulation results of the tubular curved flames and those of the opposed-jet planar flames help to reveal the effects of curvature on flame properties (mainly flame temperature).

Experimental Setup

Visible Raman spectroscopy is used to measure the temperature and concentrations of major species. The previous experimental system(Hu et al. 2006c) is used for this work with some minor upgrades. A detailed schematic diagram is shown in Figure 5. The laser beam (Continuum Powerlite 9010, frequency-doubled, pulsed Nd:YAG laser, ~355 mJ/pulse @10 Hz) passes through a rotatable zero order waveplate followed by a thin film plate polarizer mounted at its Brewster angle to enable continuous adjustment of the beam energy. The attenuated beam then goes through a pulse stretcher similar to that depicted by (Kojima and Nguyen 2002). The laser beam is split into 3 sets of beams that are trapped in 3 optical ring cavities. Each beam experiences a different time delay. A laser pulse of approximately 150 ns long is subsequently produced. This allows a pulsed laser with much

higher power to be used where laser-induced breakdown is avoided.

A small fraction of the laser beam is reflected by a plane window mounted at a small angle to monitor the laser pulse to pulse energy variation. A pyroelectric joulemeter (Coherent Molectron J50) with a ND filter and a quartz diffuser mounted in the front is utilized to detect this light. The pulse energy is used later on in the data reduction process. The main laser beam is focused by a 300 mm focal-length lens down to 150 μm in diameter at the focal point. The scattered Raman light is collected at 90º using a f/2 achromat (75 mm diameter) focused by a second achromat (f/7.5) onto the entrance slit of the spectrometer (Osborne et al. 2000). The light is then dispersed by a 600 groove/mm grating and focused to a liquid-nitrogen cooled, back-illuminated CCD camera (1024 × 1024 pixels) by a 0.65 m focusing mirror. The magnification ratio of the whole system is 3.08, which is determined by a 6 lines/mm Ronchi grating. The spatially resolved line imaging Raman signal is recorded by the camera. The sample volume (4.06 mm) is divided to 26 sections, which gives a spatial resolution of 156 μm. The ability of the system to resolve this spatial resolution is confirmed by back illuminating the 6 lines/mm Ronchi grating placed in the sample zone. The laser beam passes 4.7 mm away from the burner's axis of symmetry. The location of each data point in the radial direction is calculated based on the separation distance and its position along the laser beam from the point of symmetry.

The CCD camera is gated by a heated ferroelectric liquid crystal shutter (40 μs) and a mechanical shutter (4.0 ms) to reduce the background flame emission. The Rayleigh scattered light is blocked by an OG-550 filter (3 mm thickness). The flame illumination in

the infrared region is blocked by an infrared filter (750 nm cutoff, 3 mm thickness). 600 single-pulse Raman signals are integrated on the CCD chip to produce one Raman image. The tubular burner is translated several times along the laser beam direction to cover the entire flame. A set of representative Raman spectra at different radial locations is shown in Figure 26.

Hydrocarbon fuels are known to produce interferences mainly from C_2 LIF (Barlow et al. 2002). As shown in Figure 26-(b), (f) and (g), C_2 LIF interferes with N_2 signal, and this makes the data interpolation in the fuel rich regions difficult. All the flames studied here are blue indicating that no visible soot is present. In addition to the C_2 LIF, strong interference that comes from the scattering of the reflected laser light by the window of the burner exit port off the wall of the inner nozzle is observed at some locations, which is shown as a broadband feature in the spectra, e.g. Figure 26-(b). As a result, most of the data in the small radius regions are discarded with only two exceptions, which are shown later. The laser beam passes the flame front twice, so the two sets of identical Raman data are available for each experimental condition. In the results shown hereafter, the two data sets are shown in the same plot. This demonstrates the reliable performance of both the tubular burner and the measurement system.

Calibration flames of hydrogen-air, hydrogen-air-CO_2 and hydrogen-air-CO are produced using a Hencken burner (12.5 mm diameter multi-element matrix surrounded by a 4.3 mm wide N_2 co-flow annulus). Equilibrium conditions are assumed in the flame

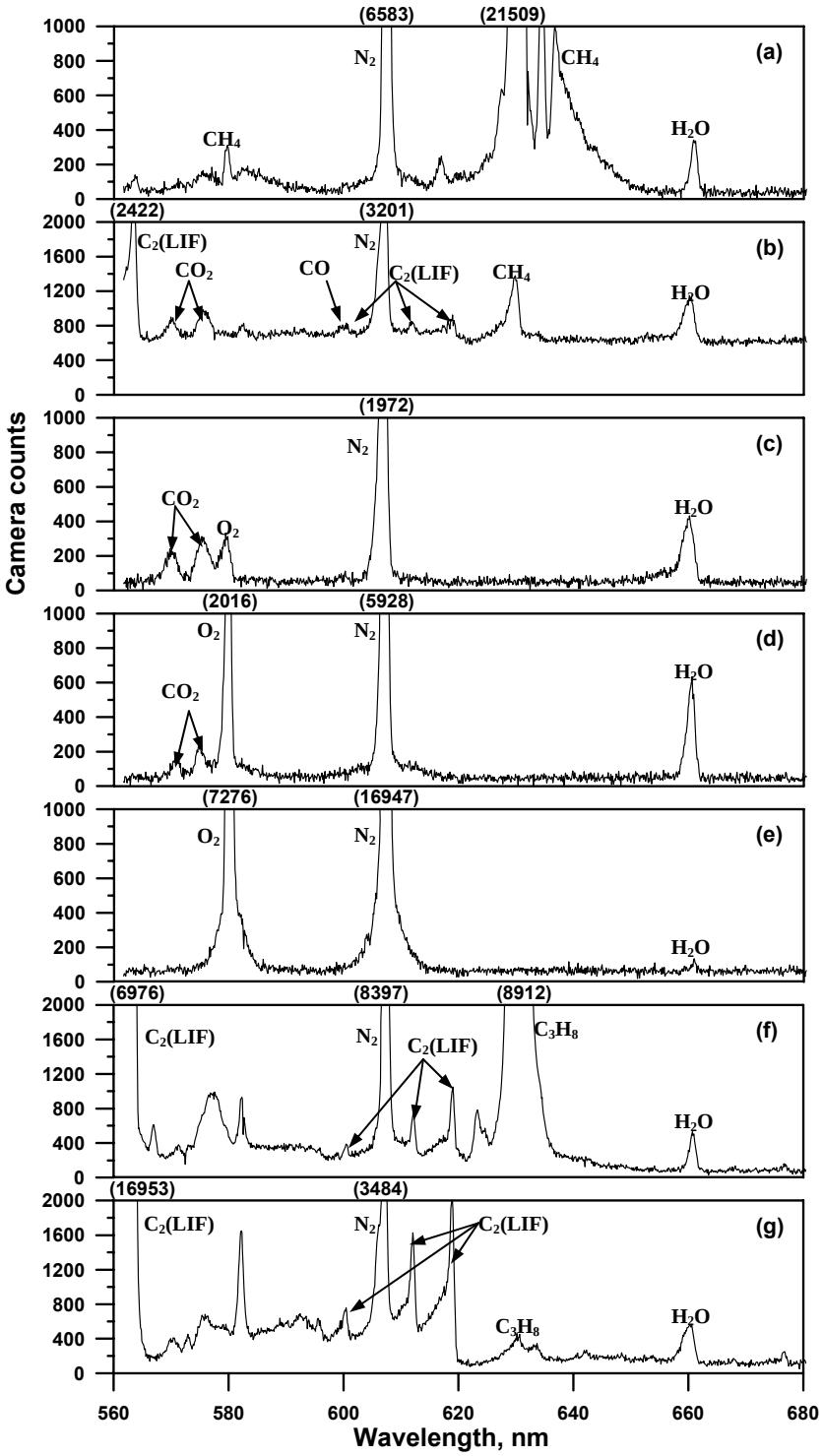

Figure 26 Raman spectra of the opposed tubular flame at different radial locations. (a) - (e) k=122 s^{-1}, R_s = 6.5 mm, 30% CH_4/N_2-air flame; (f) and (g) k=100 s^{-1}, R_s = 6.5 mm, 15% C_3H_8/N_2-air flame. (a) r = 5.2 mm, T = 563 K; (b) r = 7.0 mm, T = 1717 K; (c) r = 7.6 mm, T = 1731 K; (d) r = 8.6 mm, T = 844 K; (e) r = 10.5 mm, T = 300 K; (f) r = 5.2 mm; (g) r = 6.7 mm. (Note the different y scale in (b), (f), (g))

where the laser beam passes 18 mm downstream and the adiabatic flame temperature is used to correlate the calibration factors for each individual species. The uncertainties of the mass flow meters used in the calibration are ± 1% of full scale. The accuracy of the temperature measurement is estimated to be less than ± 5% by comparing the Raman derived temperature with the calculated adiabatic flame temperature of the calibration flames.

An opposed tubular burner with outer nozzle diameter of 30 mm and inner nozzle diameter of 6.4 mm is employed, where the heights of both nozzles are 20 mm (Figure 16). A detailed description of the opposed tubular burner can be found elsewhere (Mosbacher et al. 2002; Hu et al. 2007), but a short description is given here. The inner nozzle is porous metal (20 mm high, 6.4 mm dia.) and injects a reactant radially outward. The other reactant is injected radially inward from the outward contoured nozzles (20 mm high, 30 mm dia.). The two flows meet at a stagnation surface. As seen in Figure 16, two optical ports at 180° allow the laser beam to pass very near the inner porous cylinder. A third optical port at 90° to the laser beam enables the Raman scattered light to be collected.

The tubular flame conditions are determined by the flame stretch, k and the radius of curvature of the stagnation surface, R_s. In the flames studied here, the flame resides very close to the stagnation surface. The stretch rate, k, at the stagnation surface can be calculated using equation (3.2). Since air is the oxidizer and there is little preferential diffusion effect in the oxidizer side ($Le_o \approx 1$), we will use the stretch rate in the fuel side as the stretch rate for the opposed tubular flame. The curvature (flame radius) of the opposed tubular flame is very close to the curvature at the stagnation surface which is (Wang et al. 2006b;

Hu et al. 2006a):

$$R_s = R_2[1-(R_2/R_1 - R_1/R_2)/(R_2/R_1 - \sqrt{\rho_1/\rho_2}V_1/V_2)]^{0.5} \quad (4.1)$$

where the subscripts 1 and 2 refer to the inner and outer nozzles respectively.

Results and discussions

Two sets of experiments with different fuel type (CH_4 and C_3H_8) are conducted. Three parameters are used to describe each experimental case, which are 1) the stretch rate, k; 2) the fuel dilution ratio; 3) the radius of the stagnation surface, R_s. In the first set of experiments, flames that use 30% CH_4 diluted by 70% N_2 burning against air at various stretch rates are investigated. In the second set of experiments, flames that use 15% C_3H_8 diluted by 85% N_2 burning against air at various stretch rates are studied. For both cases, the exit velocities of the inner and outer nozzle are matched such that the calculated cold flow stagnation surface is located at R_s = 6.5 mm to produce a constant flame curvature. Concentrations of major species (CO_2, H_2O, N_2, O_2, CH_4 and C_3H_8) are derived from the Raman spectra. The temperature distribution is obtained by invoking the ideal gas law assuming constant pressure. The flames studied in this work are all concave towards the fuel stream, i.e. the fuel is issued from the burner's inner nozzle. Numerical simulations of the opposed tubular non-premixed flames are conducted using a modified Oppdif code (Mosbacher et al. 2002), where plug flow boundary conditions are assumed. Various reaction mechanisms are used which are detailed in the discussion below. All the calculation results shown hereafter have no heat transfer at the burner boundary. The experimental data

are shifted about 1.6 mm in the radial direction towards smaller values to match with the calculations. This difference in radial location is due to the difference in the boundary conditions between the experiments and simulations.

Methane Flames

Figure 27-31 show the Raman-derived profiles of temperature and major species concentrations for the non-premixed opposed tubular flames (30% CH_4/N_2 vs. air) with stretch rates ranging from $k = 41$ to 122 s^{-1}. The numerical simulated profiles are shown as solid lines in the figures. GRI 3.0 (Smith et al. 2000) mechanisms are used in the numerical simulations except in Figure 28 where simulated temperature profiles using the Kee (Kee et al. 1985), C1 (Peters and Rogg 1993), C2 (Peters and Rogg 1993) and GRI 3.0 mechanisms are shown. The Kee and C1 mechanisms model hydrocarbons with one carbon atom only; the C2 and GRI 3.0 mechanisms include up to two carbon atoms. Multicomponent formulation for transport properties is adopted. It is seen that the computed profiles agree well with the experimental measurements and the results are found to be independent of the specific chemical mechanisms as might be expected for non-premixed flames. The difference among the predicted temperature profiles is minimal.

As shown in Figure 27 and Figure 28, the flame thicknesses (FWHM) at relatively-high stretch rates ($k > 100$ s^{-1}) are small compared to other flames shown later. The regions where C_2 LIF interferes with the Raman signal are also small. As a result, temperature and species concentration data can be made available with reduced degree of

accuracy for locations where the radii are small as shown in Figure 27 and Figure 28 (see the increased scattering in the measurements for r < 7 mm). The regions where interferences become severe are marked as shadows and data are not shown due to the great uncertainty encountered in the attempt to reduce the data. As the stretch rate decreases, the flame becomes thicker as shown in Figure 29-31. Severe interferences are observed at small radial locations, and therefore the data are discarded.

Propane Flames

The Raman-derived profiles of temperature and major species concentrations for the non-premixed opposed tubular flames (15% C_3H_8/N_2 vs. air) with stretch rates ranging from k = 33 to 100 s^{-1} are shown in Figure 32-36. The numerical simulated profiles are shown as solid lines in the figures. The San Diego mechanism, which models up to three carbon atoms, is used in the simulations (http://maeweb.ucsd.edu/~combustion/cermech/). Mixing-average formulation is utilized for the C_3H_8 flames to reduce the computational cost. The experimental spectra of the propane flames suffer from C_2 LIF interferences more severely than the ones of the methane flames due to the higher concentrations of C_2 species in the fuel rich streams. A set of representative spectra are shown in Figure 26-(f) and (g). As a result, only data on the oxidizer stream side of the flame surface are made available, and the data at smaller radial locations on the fuel stream side are discarded. The computed profiles agree well with the experimental measurements. The difference between the measured and predicted temperature profiles is minimal.

Figure 37 shows the variations of the calculated maximum flame temperature of the tubular curved and opposed-jet planar flames as functions of stretch rate. The maximum flame temperatures decrease with increasing stretch rate as a result of increased degree of combustion incompleteness until the flame extinguishes (denoted by a vertical line). However, curvature shows different effects on the maximum temperatures of the hydrogen, methane and propane flames. For H_2 flame with low fuel Lewis number (Le_f <1), the opposed jet planar flame temperature is higher than that of the concave opposed tubular flame, and lower than that of the convex one. These results with H_2/N_2 fuels are consistent with previous studies in perturbed opposed jet flames and in the flame tip of the Burke-Schumann flame (Katta et al. 1998; Lee et al. 2000; Takagi et al. 1996b; Yoshida and Takagi 1998; Yoshida and Takagi 2003; Finke and Grünefeld 2000; Ishizuka 1982; Im et al. 1990; Takagi et al. 1996a). For example in numerical analysis of an opposed jet flame perturbed by suction, Yoshida and Takagi (2003) found that the flame temperature of 15% H_2/N_2 vs. air was lowest for the flame concave towards the fuel and highest for the flame convex towards the fuel. However, for C_3H_8 flame (Le_f >1), the opposite stands as the flame temperature is higher for the flame concave toward the fuel as shown in Figure 37. None of the previous studies of curvature in diffusion flames investigated fuels such as C_3H_8 with Le_f >1. The effects of Lewis number coupled with curvature are believed to be responsible for such a difference as suggested by earlier studies. The Lewis number of the oxidizer stream is close to unity and not varied in these experiments. The non-unity Lewis

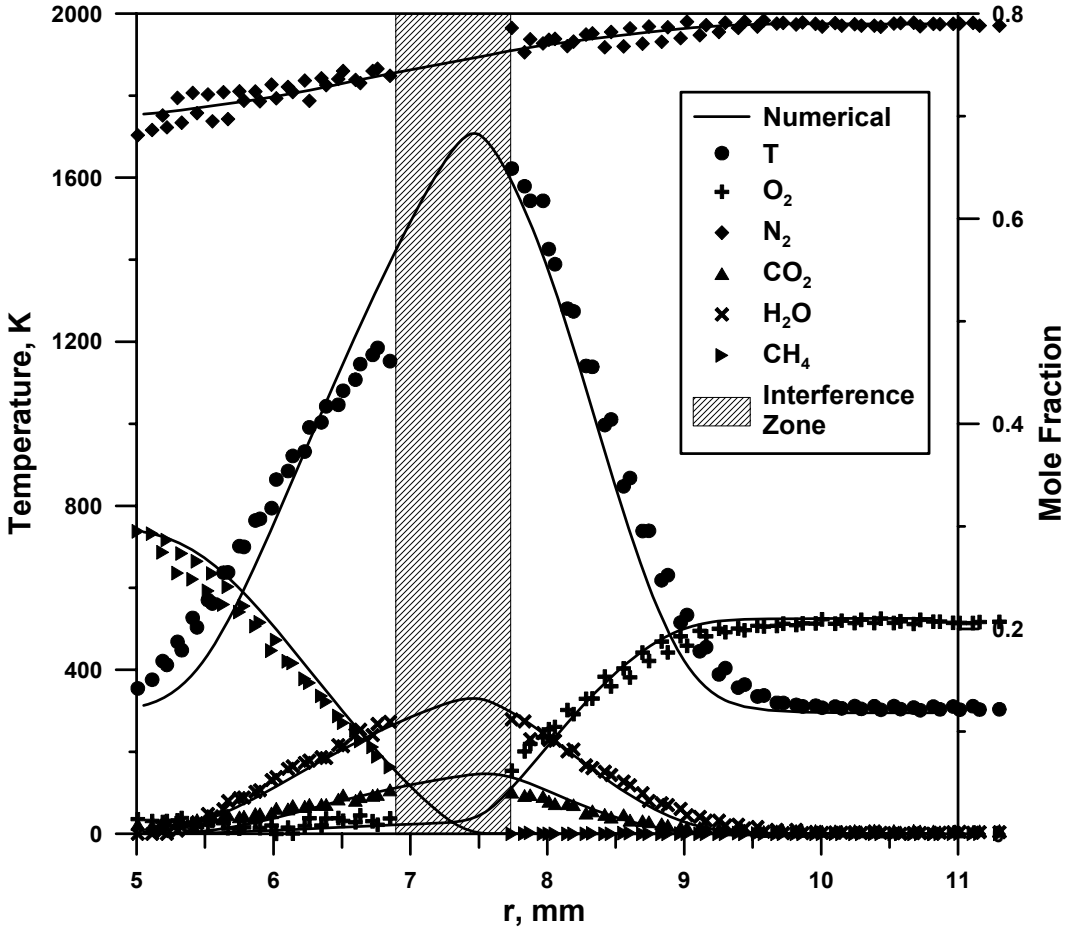

Figure 27 Measured and calculated temperature and major species mole fraction profiles as functions of radius for a 30% CH_4/N_2-air non-premixed tubular flame at k=122 s^{-1}, R_s =6.5 mm

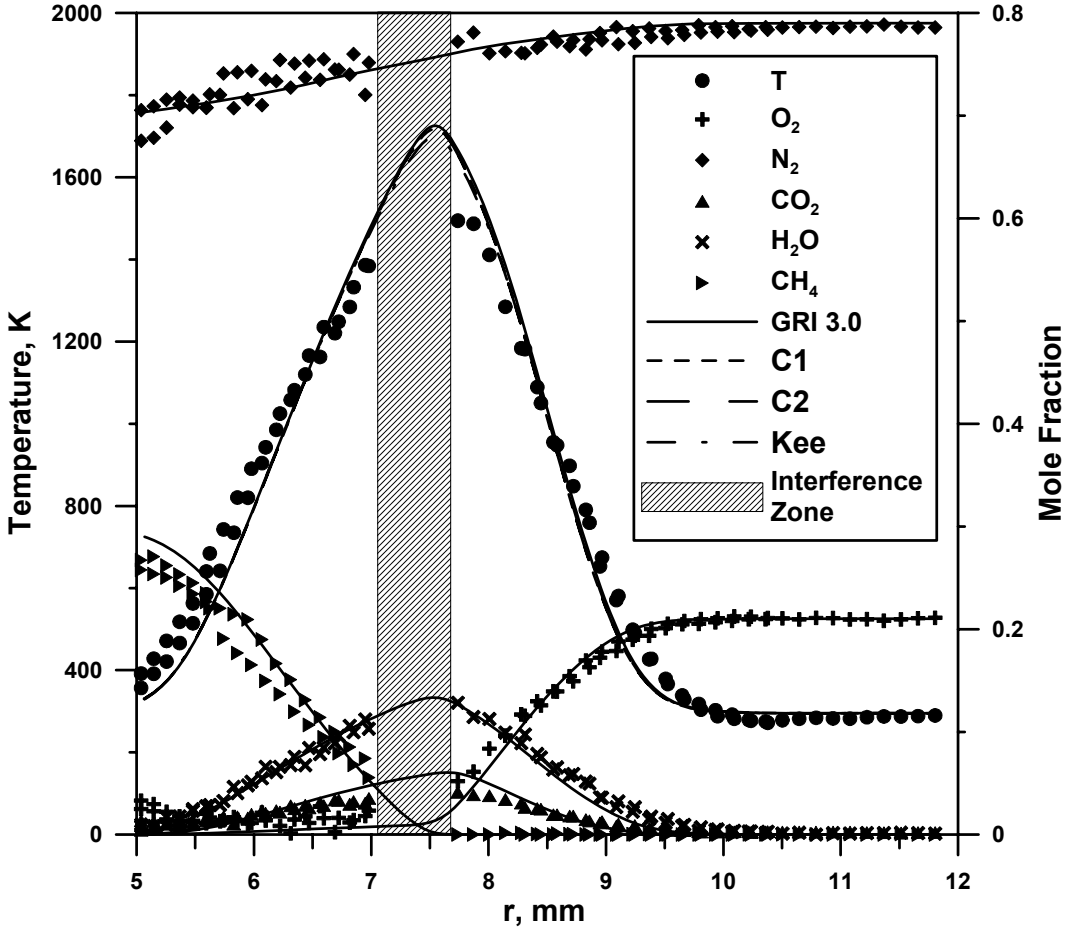

Figure 28 Measured and calculated temperature and major species mole fraction profiles as functions of radius for a 30% CH_4/N_2-air non-premixed tubular flame at k=102 s^{-1}, R_s = 6.5 mm

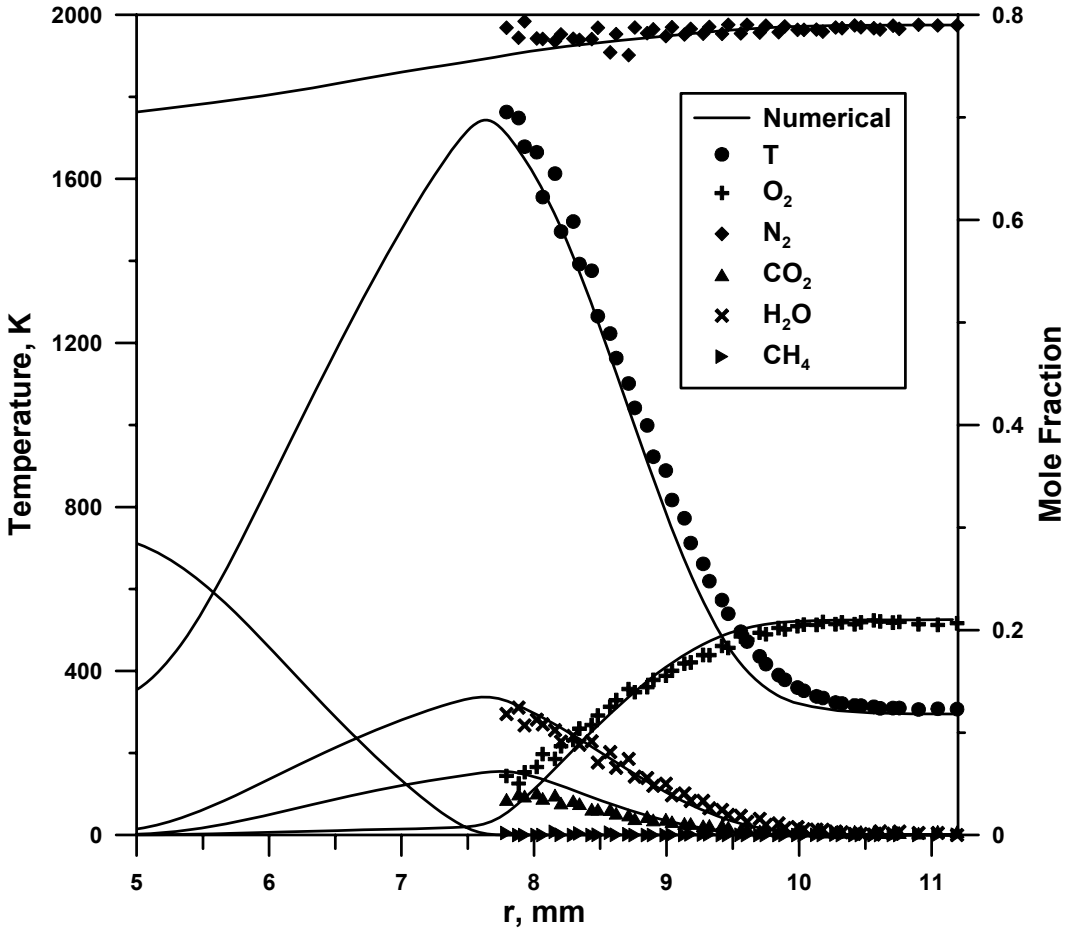

Figure 29 Measured and calculated temperature and major species mole fraction profiles as functions of radius for a 30% CH_4/N_2-air non-premixed tubular flame at k=81 s^{-1}, R_s = 6.5 mm

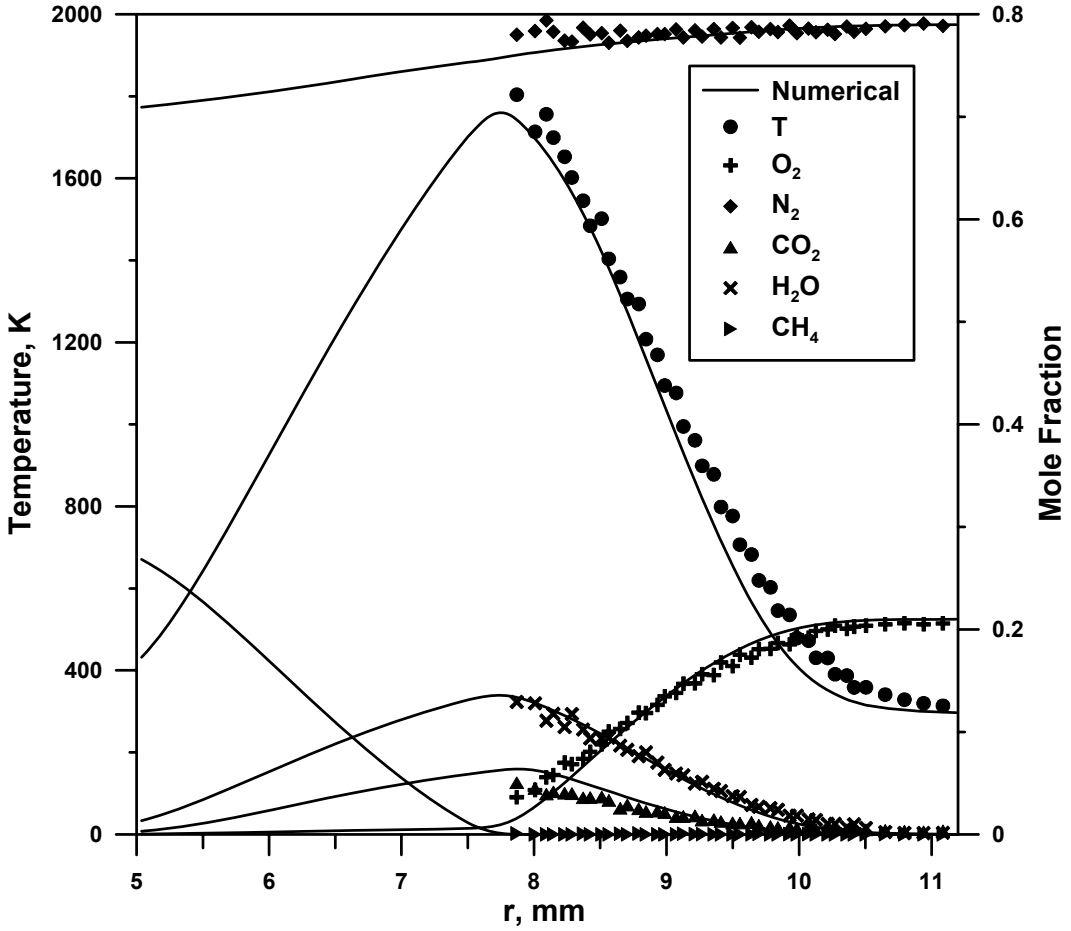

Figure 30 Measured and calculated temperature and major species mole fraction profiles as functions of radius for a 30% CH_4/N_2-air non-premixed tubular flame at k=61 s^{-1}, R_s = 6.5 mm

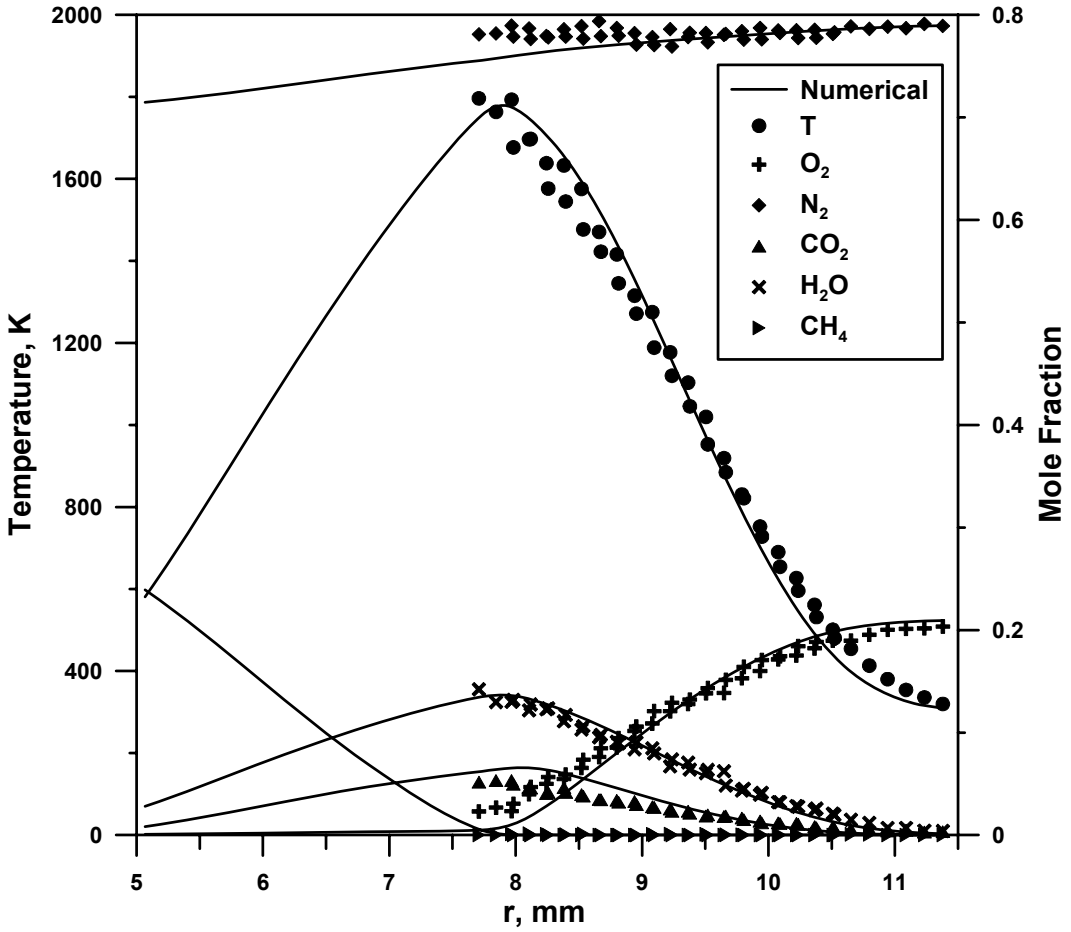

Figure 31 Measured and calculated temperature and major species mole fraction profiles as functions of radius for a 30% CH_4/N_2-air non-premixed tubular flame at k=41 s^{-1}, R_s = 6.5 mm

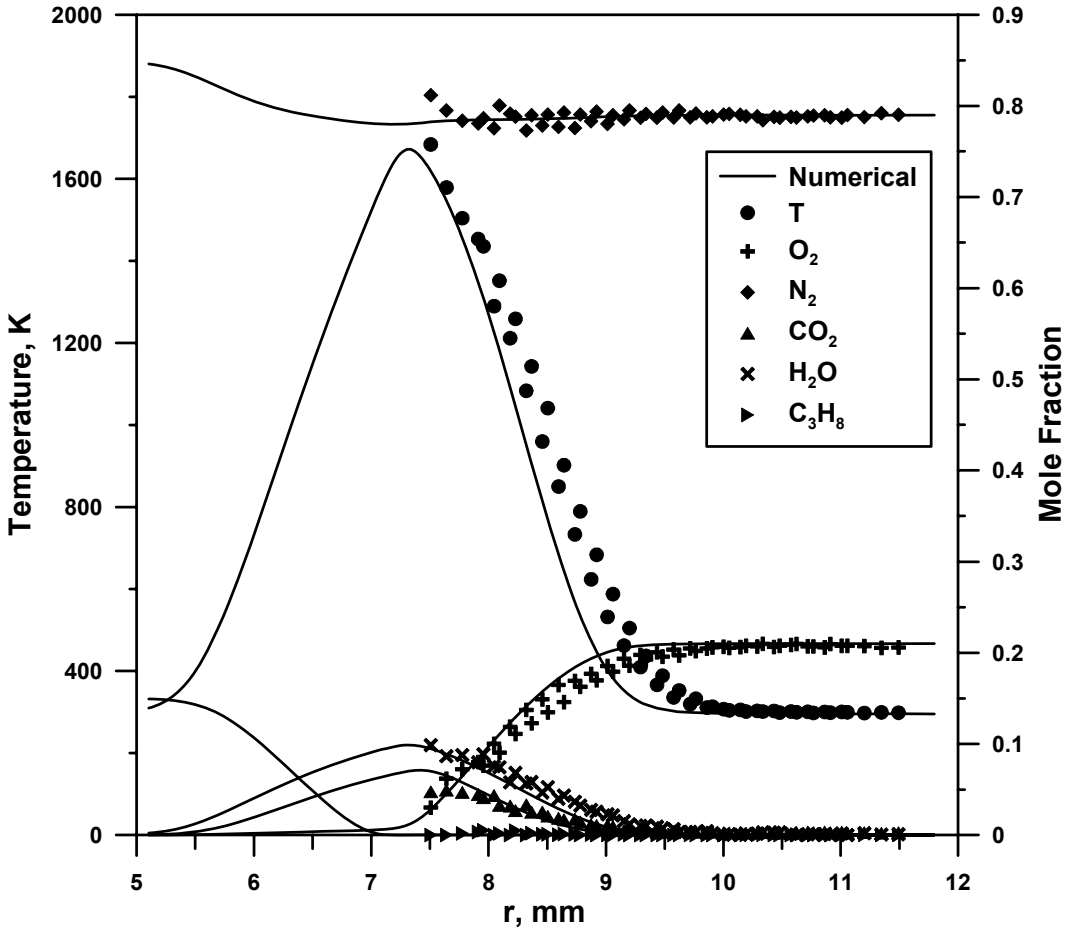

Figure 32 Measured and calculated temperature and major species mole fraction profiles as functions of radius for a 15% C_3H_8/N_2-air non-premixed tubular flame at k=100 s^{-1}, R_s =6.5 mm

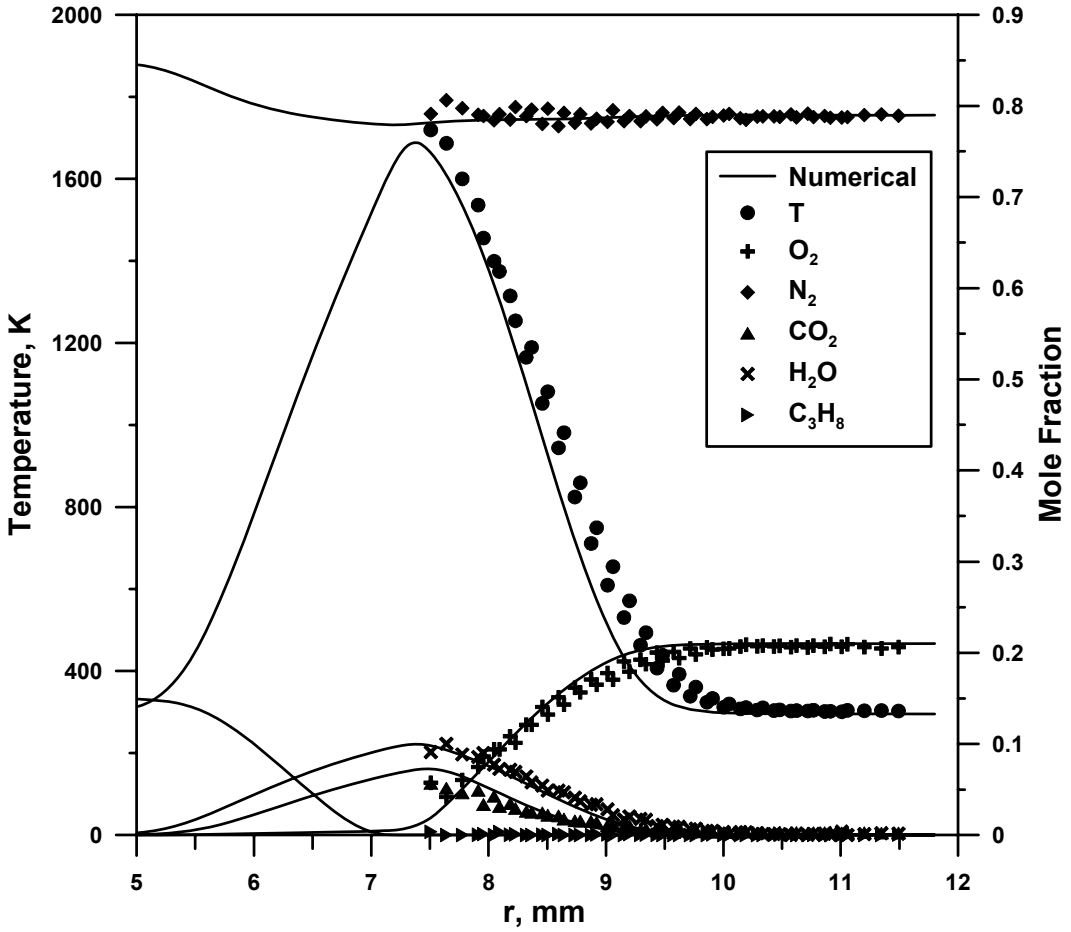

Figure 33 Measured and calculated temperature and major species mole fraction profiles as functions of radius for a 15% C_3H_8/N_2-air non-premixed tubular flame at k=84 s^{-1}, R_s =6.5 mm

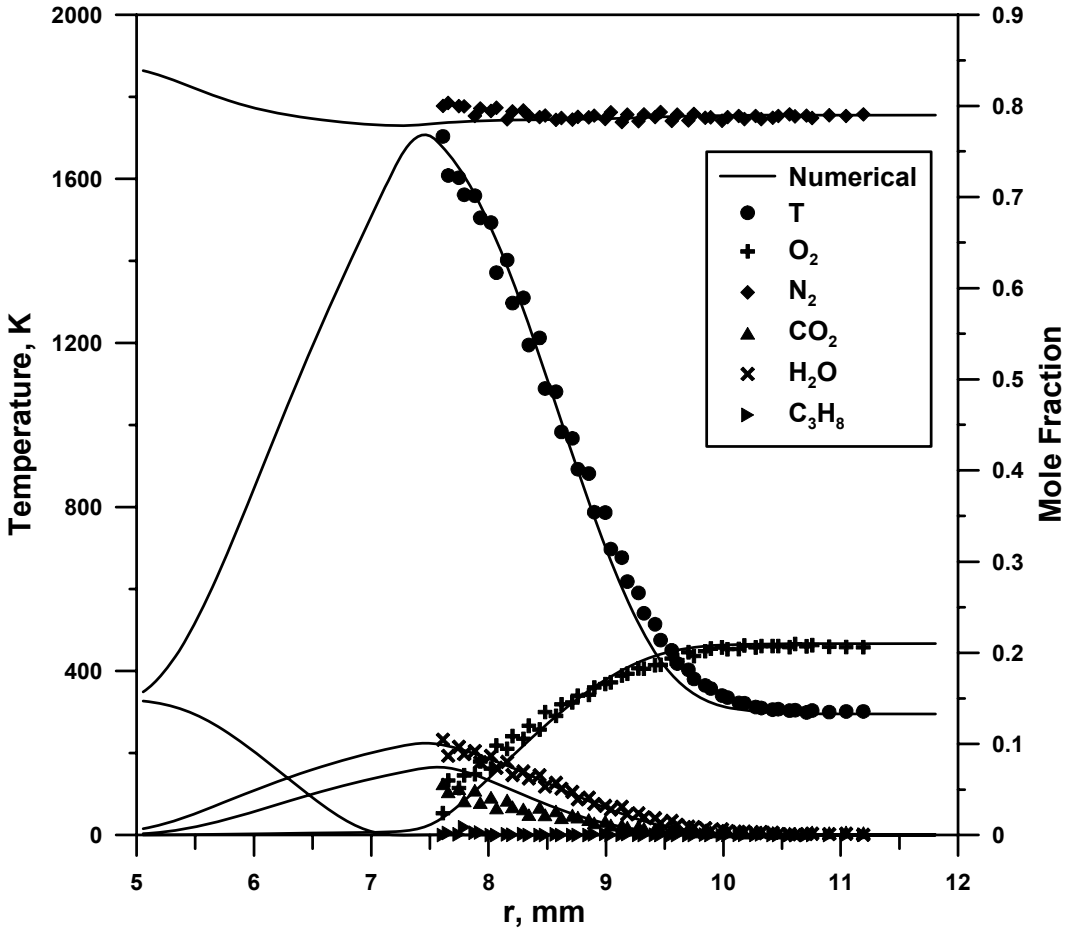

Figure 34 Measured and calculated temperature and major species mole fraction profiles as functions of radius for a 15% C_3H_8/N_2-air non-premixed tubular flame at k=67 s^{-1}, R_s =6.5 mm.

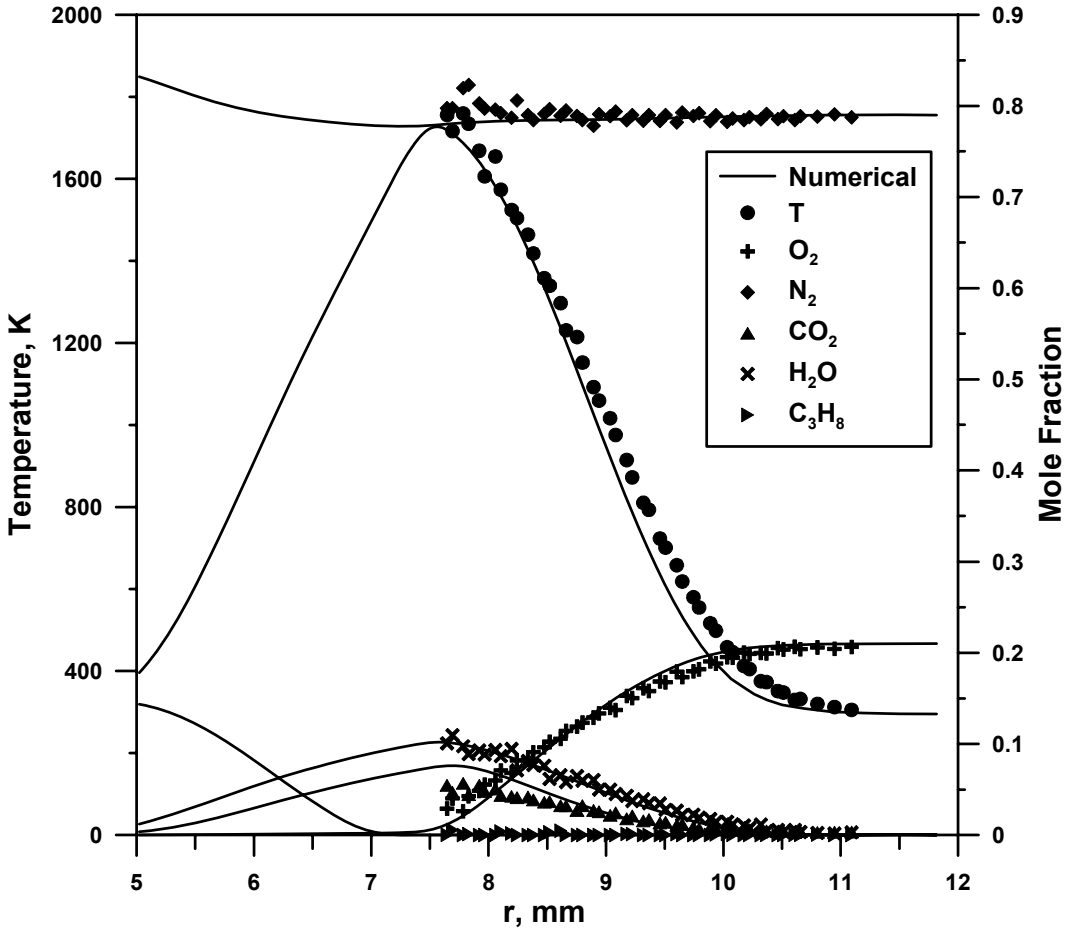

Figure 35 Measured and calculated temperature and major species mole fraction profiles as functions of radius for a 15% C_3H_8/N_2-air non-premixed tubular flame at k=50 s^{-1}, R_s =6.5 mm.

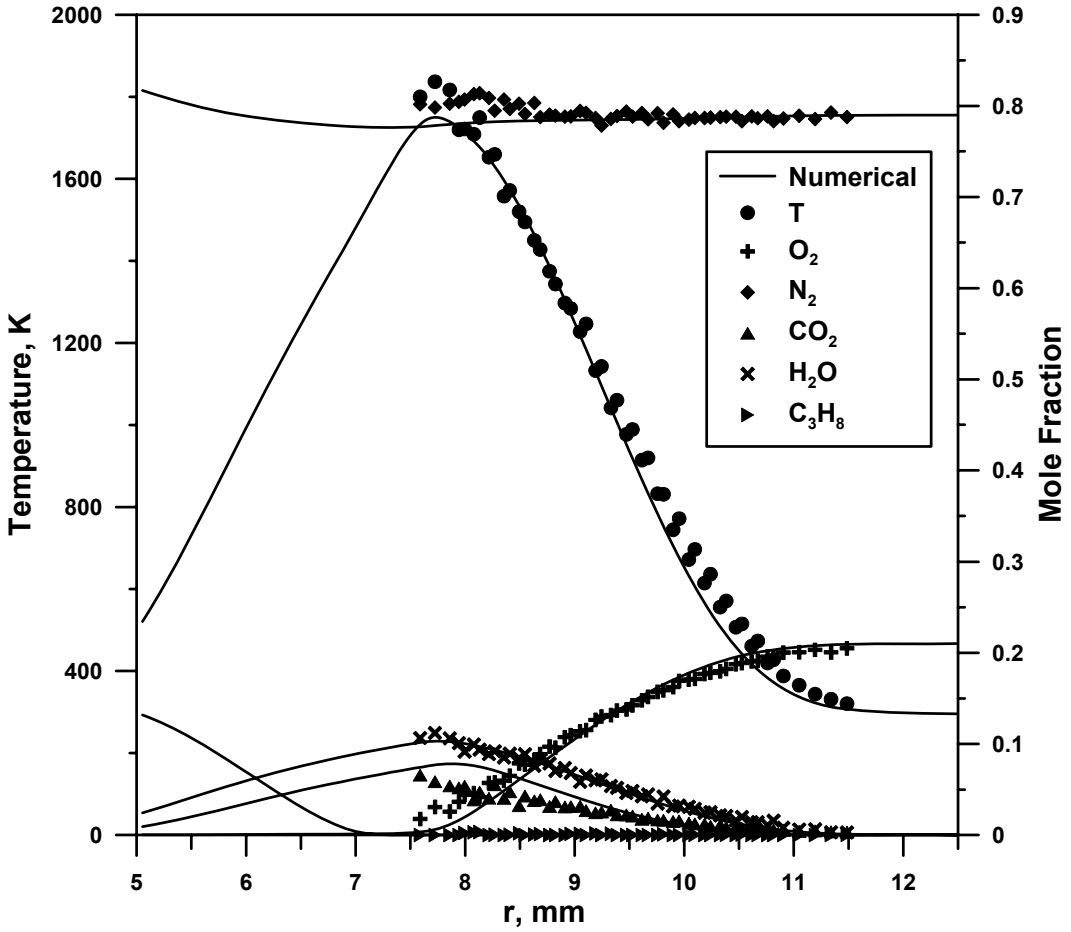

Figure 36 Measured and calculated temperature and major species mole fraction profiles as functions of radius for a 15% C_3H_8/N_2-air non-premixed tubular flame at k=33 s^{-1}, R_s =6.5 mm.

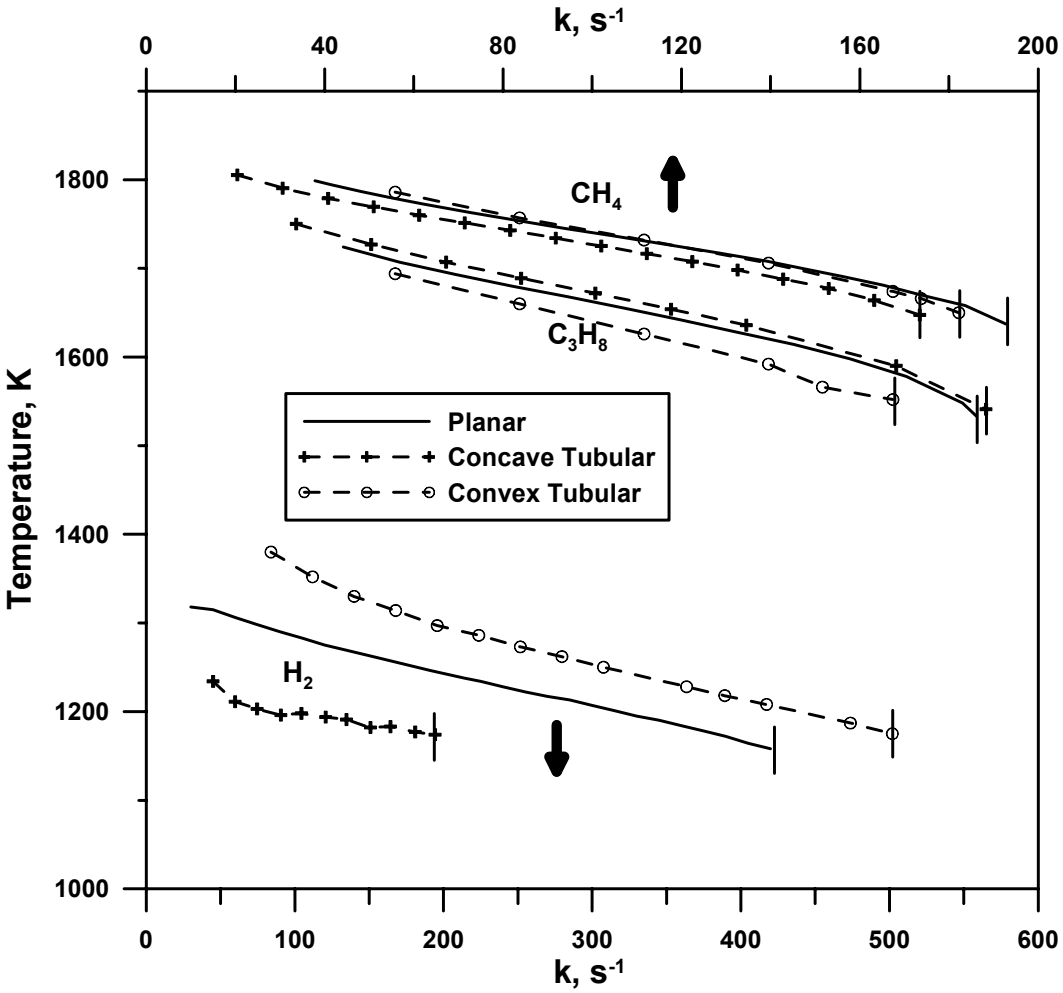

Figure 37 Calculated maximum flame temperature as functions of stretch rate of the opposed jet planar and tubular flames using 15% H_2/N_2, 30% CH_4/N_2 and 15% C_3H_8/N_2 showing the different effects of curvature (Note H_2 uses the lower x-axis and CH_4/C_3H_8 use the upper x-axis.)

number of the fuel mixture controls the diffusion of the fuel to the flame surface. When Lewis number of the fuel stream is greater than one (C_3H_8/N_2), curvature concave toward the fuel stream promotes combustion and flames exhibit higher peak temperature. Given the Lewis number of H_2/N_2 is much less than one, curvature concave toward the fuel stream retards combustion and flames exhibit lower peak temperature, while curvature convex toward the fuel stream promotes combustion and flames exhibit higher peak temperature. As shown in Figure 37, the effects of curvature on curved methane flames are ambiguous, because the Lewis number of CH_4/N_2 mixture is close to one. Although the peak flame temperature of concave methane flame is lower than that of the planar flame, which suggests that the methane flames act like flames with Lewis number less than one, the peak flame temperature of the convex methane flame is almost the same as that of the planar ones, which indicates the effects of curvature is not important. Interestingly, simulation shows that both curved flames demonstrated smaller extinction stretch rates than their planar counterpart. It is surprising to see from the numerical results of Figure 37 that the temperature difference between the propane flame curves is so small considering the Lewis number of the C_3H_8/N_2 mixture is much larger than one.

Conclusion

Non-premixed tubular hydrocarbon flames are established using a uniquely-designed opposed tubular burner. Laser-induced Raman spectroscopy is applied to both methane and propane flames. Temperature and major species concentrations (CO_2, H_2O, N_2, O_2, CH_4

and C_3H_8) are reported with good resolution. Due to the interferences from the C_2 LIF and the scattering of the inner wall, only data on the oxidizer side are made available in most cases. Numerical simulations of the measured flames using various reaction mechanisms are conducted. Shown in the methane flame simulation, the specific reaction mechanism has little effect on the simulation results of temperature and major species concentrations. The experimental data and numerical predictions agree well. Comparison of the peak flame temperatures from the simulation results of the opposed jet planar and those of the opposed tubular flames shows that flame curvature concave toward the fuel stream strengthens the flame when the Lewis number of the fuel mixture is greater than unity; vice versa when the fuel Lewis number is less than one. The results with are consistent with earlier studies.

CHAPTER V

EXTINCTION AND NEAR-EXTINCTION INSTABILITY OF NON-PREMIXED TUBULAR FLAMES

Introduction

Flame extinction is important for both turbulent combustion and fire safety (Williams 1981). Four types of extinction, namely extinction by stretch rate, extinction by dilution, extinction by convective heat transfer, and extinction by radiation (Williams 2000), are of interest to researchers with the first two attracting the most attention. First investigated by Spalding in the forward stagnation region of a porous sphere in a uniform air stream (Spalding 1953; Spalding 1954), extinction of counterflow diffusion flames has been examined with flames formed under various geometries including porous spheres (Spalding 1953; Spalding 1954; Simmons and Wolfhard 1957), opposed jet burners (Potter and Butler 1959; Potter et al. 1962; Pandya and Weinberg 1963; Puri and Seshadri 1986; Chen and Sohrab 1991; Pellett et al. 1998) and Tsuji burners where the flame is formed in the forward stagnation region of a porous cylinder immersed in a uniform air stream (Tsuji and Yamaoka 1967; Ishizuka and Tsuji 1981; Tsuji 1982; Riechelmann et al. 2002). Typically, extinction limits are measured at the limiting fuel and oxidizer concentrations using various diluents at the varying injection velocities (or stretch rates). Numerical investigation of the extinction of diffusion flames with detailed chemistry started in the 1980's. Extinction prediction on the Tsuji type burner using complex chemistry and detailed for-

mulation of the transport fluxes was performed as a collaborated effort by five research groups (Dixon-Lewis et al. 1984) and the results compared well with the measured values (Tsuji and Yamaoka 1969; Tsuji 1982). Similar numerical efforts on the opposed-jet burner can be found elsewhere (Seshadri et al. 1989; Chelliah et al. 1990; Darabiha and Candel 1992).

While research on extinction of the non-premixed flames subject to the effects of flame stretch and non-unity Lewis number abounds, experimental studies on the effects of curvature are less numerous. This is mainly because of the difficulties in establishing a simple geometry that will allow detailed investigations. Despite these difficulties, studies have been made to investigate the curvature effects on flame extinction (i.e., tip-opening) of Burke-Schumann flames (Ishizuka 1982; Ishizuka and Sakai 1986; Im et al. 1990; Takagi and Xu 1996; Takagi et al. 1996a) and perturbed opposed-jet flames (Rolon et al. 1995; Takagi et al. 1996b; Yoshida and Takagi 1998; Finke and Grünefeld 2000; Katta et al. 2003). In an enclosed axisymmetric diffusion flame where the flame curvature is concave to the fuel, Ishizuka finds the tip-opening can occur for H_2 fuel diluted with Ar, CO_2, or N_2 gas but not He gas and suggests that the Lewis number of the fuel is a controlling parameter (Ishizuka 1982). In detailed transport and complex chemistry calculations of usual and inverse H_2/N_2 axisymmetric jet diffusion flames, Takagi et. al. found that concave curvature towards the H_2/N_2 fuel decreases the flame temperature below the adiabatic flame temperature (vice-versa for convex curvature) and the effect is magnified as the flame curvature increases (Takagi et al. 1996a). Katta et al. numerically studied the interaction of

a small vortex with a H_2/N_2-air planar opposed jet flame and found that micro-vortex from the fuel side (concave curvature) more easily extinguished the flame than a vortex form the air side (Katta et al. 2003). Both the results from Burke-Schumann flames and perturbed opposed jet flames are consistent in that concave flame curvature towards H_2/N_2 fuel weakens the flame and leads to extinction.

Despite the rich discoveries in the previous experimental and numerical studies, the effects of curvature on extinction deserve more attention. By installing a nozzle along the center axis of the tubular burner as a second, radially-outwardly flowing reactant source, non-premixed and partially-premixed flames subject to well-controlled aerodynamic straining and flame curvature can be created (Hu 2007). This burner possesses the advantages over the above-mentioned methods in that it allows a more detailed quantitative study of the non-premixed flame subject to the influences of both uniform stretch and uniform curvature. It offers the capability of investigating the effects of curvature on the flame extinction, which constitutes the first objective of this study.

Flames near extinction conditions often exhibit instability, which leads to cellular structure and/or oscillation. Cellular instability of non-premixed flames has been reported by several researchers using various types of burners. One of the earliest studies was reported by Dongworth and Melvin (Dongworth and Melvin 1976), where a Wolfhard-Parker burner was used. Flames produced by hydrogen/nitrogen-air exhibited cellular structure at a certain fuel dilution ratio. The authors postulated that inter-lancing of the non-premixed stream and the premixed stream of fuel and oxidizer through inter-stream

diffusion at the flame base produced a non-uniform distribution of fuel at the flame base, and was therefore responsible for the occurrence of cellularity, although the factors determining the size of the cells was not clearly identified. Ishizuka and Tsuji observed a striped pattern for hydrogen-nitrogen/air flames established in the Tsuji-type burner, where the flame resided in the fuel side of the stagnation point (Ishizuka and Tsuji 1981). The authors attributed this phenomenon to the preferential diffusion of H_2 relative to N_2 in the fuel mixture and claimed that it closely resembled a similar discovery in premixed flames. Cellular instability and flame extinction using a slot-jet burner were systematically studied by Chen et al., where hydrogen, methane and propane diluted with a variety of inert diluents were used (Chen et al. 1992). Based on the experimental results, they proposed that near-extinction and sufficiently low Lewis number of the "deficient" (i.e., more completely consumed) reactant (Le $\leqslant$ 0.8) were the two requirements for flame to exhibit cellular instability. The Lewis number (diffusive-thermal) effect in a manner similar to that of premixed flames was argued to be the driving force instead of the effects of preferential diffusion. The diffusive-thermal instability of non-premixed flames was further investigated in a counterflow slot jet burner at low Lewis number (Kaiser et al. 2000). A tube-like flame generated by the balance between flame weakening due to strain and intensification due to curvature was reported for the H_2/N_2-air flames. Flame tubes of various states were observed under various flow configurations. In a recent study (Jacono et al. 2003), cell formation in non-premixed, axisymmetric jet flames near extinction was investigated in detail, where much attention was draw upon the influence of initial mixture strength $\boldsymbol{\phi}$ to

the selection criteria of cellular patterns. Most recently, scaling of cell size as functions of jet velocity and initial mixture strength was studied in detail using an axisymmetric jet burner and slot burner (Jacono 2007). On the other hand, theoretical study on the diffusional-thermal instability of diffusion flames using activation-energy asymptotics was first started by Kim, Williams and Ronney (Kim et al. 1996). Additional contributions can be found from several other researchers (Cheatham and Matalon 2000; Papas et al. 2003; Metzener and Matalon 2006) and a good review was given by Matalon (Matalon 2007).

Cellular structure in opposed tubular flames has been reported in previous studies (Hu et al. 2007) for flames produced by reactants with non-unity Lewis numbers. It was shown that the flame instability originated from the effects of curvature and Lewis number. However, a systematic investigation on the near-extinction behavior of non-premixed tubular flames was not conducted. The second objective of this study is to characterize the cellularity of the opposed tubular flames burning N_2, He, Ar or CO_2 diluted H_2, CH_4 or C_3H_8 against air. The initial mixture strength (calculated as the fuel-to-oxygen molar ratio normalized by the stoichiometric molar ratio) and stretch rate at the stagnation surface are used as parameters to describe the cellular instability.

Experimental Method

An opposed tubular burner with outer nozzle diameter of 30 mm and inner nozzle diameter of 6.4 mm is employed, where the heights of both nozzles are 20 mm (Figure 16). A detailed description of the burner can be found elsewhere (Mosbacher et al. 2002; Hu et

al. 2007). Fuel mixtures are formed by diluting H_2, CH_4 or C_3H_8 with N_2, He, Ar or CO_2. The fuel-diluent combinations attempted in this study are summarized in Table 4. The fuel + diluent mixture is sent through the inner nozzle flowing outward, and oxidizer, which is always air, is sent through the outer nozzle flowing inward. The only exception is a $H_2 + N_2$ case, where the fuel and oxidizer flows are switched in order to generate flames with opposite curvature as shown in Table 4.

A mirror with a slot-cutout is mounted underneath the tubular burner at 45 degrees to the axis of symmetry, which provides a view of the flame in the axial direction. An infrared sensitive ICCD video camera (Xybion ISG-250) mounted horizontally toward the mirror records the axially-integrated chemiluminescence emission from the flames to monitor the extinction and cellular structure. A typical picture of the flame is shown in Figure 38, where the upper part of the circle is missing due to the presence of the inner nozzle. The gas flows are controlled by mass flow controllers (Teledyne Hastings HFC-202/203) through a computer. During the experiment, a non-premixed tubular flame is ignited at a fuel concentration that is slightly higher than its corresponding extinction value, and then the fuel concentration is decreased in steps of 0.1-0.2% of the full scale of the flow controllers until extinction is reached. There are only a few cases where the flame is started at a lower diluent level and then the flow rate of the diluent is gradually increased until extinction is reached. All gas flows are supplied at room temperature 297 K.

The radius of curvature at the stagnation surface of the cold flow, R_s, given by Wang et al. (Wang et al. 2006b; Wang et al. 2007), is a function of the inlet radii, density, and

Table 4 Summary of experimental conditions and relevant parameters.

Fuel	Di	R_s[a]	X_F[b], %	K[c], s^{-1}	ϕ[d]	Le_F[e]	α[f]	CV[g]	CL[h]
CH_4	N_2	5.0	14.9 - 26.3	24.4 - 218	1.42 - 2.51	1.02 - 1.03	0.64 - 0.34	CA	N
		6.5	15.3 - 49.5*	16.7 - 172	1.46 - 4.71	1.02 - 1.05	0.62 - 0.16	CA	N
		8.0	15.6 - 21.0	18.2 - 89.2	1.49 - 2.00	1.02	0.61 - 0.44	CA	N
CH_4	He	5.0	15.8 - 37.2	107 - 270	1.50 - 3.55	1.72 - 1.09	0.14 - 0.08	CA	N
		6.5	20.8 - 34.0	47.1 - 193	1.98 - 3.24	1.54 - 1.16	0.11 - 0.09	CA	N
CH_4	Ar	5.0	10.1 - 18.6	35.2 - 163	0.96 - 1.78	0.96	1.35 - 0.69	CA	N
		6.5	10.2 - 19.5	24.6 - 150	0.97 - 1.86	0.96	1.34 - 0.66	CA	N
CH_4	CO_2	5.0	25.1 - 32.0	21.4 - 113	2.39 - 3.04	0.82 - 0.86	0.54 - 0.40	CA	N
		6.5	24.2 - 33.7	22.4 - 88.0	2.30 - 3.21	0.81 - 0.87	0.56 - 0.37	CA	N
		8.0	24.0 - 38.3	28.1 - 129	2.29 - 3.65	0.81 - 0.90	0.57 - 0.32	CA	N
C_3H_8	N_2	5.0	6.16 - 14.3	22.9 - 180	1.47 - 3.40	1.76 - 1.51	0.69 - 0.31	CA	N
		6.5	6.90 - 15.7	25.0 - 196	1.64 - 3.74	1.74 - 1.47	0.62 - 0.29	CA	N
		8.0	7.33 - 17.9*	20.0 - 142	1.75 - 4.27	1.72 - 1.41	0.58 - 0.25	CA	N
H_2	N_2	5.0	10.7 - 16.9*	25.2 - 172	0.25 - 0.40	0.37 - 0.42	3.46 - 2.03	CA	Y
		6.5	9.08 - 16.9*	19.4 - 214	0.22 - 0.40	0.35 - 0.42	4.12 - 2.03	CA	Y
		8.0	8.56 - 10.3	30.4 - 90.9	0.20 - 0.25	0.35 - 0.37	4.38 - 3.57	CA	Y
H_2	N_2	5.0	6.43 - 7.99	35.6 - 96.0	0.15 - 0.19	0.33 - 0.34	5.97 - 4.73	CX	Y
		6.5	7.35 - 8.61	26.4 - 106	0.18 - 0.21	0.34 - 0.35	5.17 - 4.36	CX	Y
H_2	He	5.0	10.3 - 13.1	154 - 465	0.25 - 0.31	1.10 - 1.09	0.54 - 0.42	CA	N
		6.5	10.5 - 13.1	71.0 - 380	0.25 - 0.31	1.10 - 1.09	0.52 - 0.42	CA	N
		8.0	11.2 - 12.5	56.6 - 227	0.27 - 0.30	1.10	0.49 - 0.44	CA	N
H_2	Ar	5.0	8.93 - 10.6	34.6 - 205	0.21 - 0.25	0.35 - 0.37	5.95 - 4.92	CA	Y
		6.5	7.29 - 9.19	23.9 - 216	0.17 - 0.22	0.33 - 0.35	7.41 - 5.77	CA	Y
H_2	CO_2	5.0	14.6 - 15.8	41.8 - 138	0.35 - 0.38	0.29	3.79 - 3.44	CA	Y
		6.5	12.1 - 20.6*	25.9 - 131	0.29 - 0.49	0.26 - 0.34	4.67 - 2.50	CA	Y

[a] Radius of the stagnation surface based on the cold flow condition; unit: mm

[b] Mole concentration of fuel at nozzle outlet

[c] Stretch rate at the fuel side of the stagnation surface

[d] Mole-based initial mixture strength, fuel-to-oxygen molar ratio normalized by the stoichiometric molar ratio

[e] Lewis number of the fuel stream

[f] Mass-based initial mixture strength, oxygen-to-fuel mass ratio normalized by the stoichiometric mass ratio

[g] Direction of curvature, CA: concave; CX: convex

[h] Cellularity, Y: yes; N: no

* Effects of heat losses at low stretch rates.

Figure 38 Axial integrated image of the concave H_2-N_2/air opposed tubular flame at ϕ = 0.448, *k*=53 s-1, R_s≈6.5 mm (the fuel mixture originates from the inner porous nozzle; the upper part of the image is blocked by the inner nozzle feed line).

velocity of the two opposing streams. As a result, the radius of curvature of the flame can be controlled by varying the velocity ratio of the two nozzles at given nozzle radii and the flow density ratio. In this study, R_s is used to describe the degree of curvature of each individual flame. Three R_s's are realized for different fuel/diluent mixtures as summarized in Table 4.

The influence of the flow rate of N_2 co-flow is evaluated and can be neglected. The mass flow controllers have an 1% full scale accuracy. For each extinction and instability onset data point presented hereafter, the experiments are repeated at least three times and the mean values are used. The uncertainties are estimated based on the standard deviation of the measured data and the accuracy of the mass flow controllers, i.e. the maximum of the above two values are used and shown as error bars on the subsequent figures. The difference between measurements is generally within ±3% of the average, although in some cases, somewhat larger variations can be observed.

Experimental Results and Discussion

Extinction data for different fuel-diluent combinations subject to various degrees of curvature are first presented and discussion is focused on extinction by stretch rate, which is represented by the upper branches of the extinction curves shown hereafter. This is followed by the experimental results for the onset of cellular structures. The stagnation stretch rate on the fuel side of the cold flow field is used as the characteristic stretch rate, and its expression can be found elsewhere (Wang et al. 2006b; Wang et al. 1007). In the

subsequent discussions, the term, concave or convex flame curvature is always with respect to the fuel stream.

Extinction

Figure 39 shows the extinction stretch rate versus the initial mixture strength for N_2 diluted CH_4 and C_3H_8 concave opposed tubular flames subject to various degrees of curvature. The upper branches of the curves show the effects of stretch rate on the flame, i.e. the fuel concentration needed to sustain the flame is higher as the flame is stretched more, while the lower branches show the extinction behavior due to heat losses to the inner nozzle as the reactant inlet velocities have dropped very low and flames become very thick. Numerical simulation of the flame structure shows that temperature gradient at the inner wall boundary only exists when the stretch rate is less than ~30 s^{-1}, which roughly corresponds to the turning point in Figure 39. The upper branches have similar slopes within each fuel group. The extinction curves of both the CH_4-N_2 and C_3H_8-N_2 mixtures subject to different degrees of curvature lie close to each other respectively, although the Lewis number for the CH_4-N_2 is less than that of the C_3H_8-N_2 mixture (Table 4). The mass based initial mixture strength α, which is calculated as oxygen-to-fuel mass ratio normalized by the stoichiometric mass ratio (Liñán 1974), for both mixtures are less than 1 and fall within a similar range. This suggests that the non-premixed flame is oxidizer deficient and flame resides on the oxidizer side of the stagnation surface. The effects of curvature are such that the flames are more resistant to extinction as they are curved more (smaller radii of cur-

vature) as shown in Figure 39. This has two implications: 1) the concave curvature strengthens the non-premixed flame, which leads to higher extinction stretch rates; 2) the critical Lewis number where the opposite curvature effects occur (i.e. concave curvature weakens the flame), Le_{cr}, is less than 1.

Figure 40 shows the extinction stretch rate as function of the initial mixture strength for He, Ar or CO_2 diluted CH_4 flames subject to various degrees of curvature. Although the Lewis number goes from above one to less than one (Table 4), the extinction stretch rates for smaller R_s are always higher than that for larger R_s at a given initial mixture strength, i.e. extinction curves with smaller R_s are always to the left of the ones with higher R_s values. Similar phenomena can also be observed in Figure 39. This again confirms that the concave curvature strengthens these non-premixed flames. The α value of both the CH_4-He and CH_4-CO_2 mixtures are less than unity, which means the flame is on the oxidizer side of the stagnation surface. Although the α value of the CH_4-Ar mixture goes from above one to below it, the Lewis numbers in both streams of this flame are close to unity. As a result the extinction curves lie close to each other.

It can be seen in Figure 40 that the gap between the helium-diluted extinction curves subject to different radii of curvature is wider than that of the argon or carbon dioxide diluted ones. In addition, Figure 39 shows that at Lewis numbers close to that of the CH_4-He mixture, the extinction curves of the C_3H_8-N_2 mixture lies close to each other. One possible explanation is based on the mass-based initial mixture strength and the effects of curvature. The α value for CH_4-He mixture is very small comparing to the others, which indicates

that this flame is extremely oxidizer deficient. This means the opposed tubular flame would reside deep in the oxidizer stream and difference between the flame radii are magnified. This will lead to the widened gap between the two curves shown in Figure 40. Greater difficulties are encountered when trying to ignite this flame due to the increased flame instabilities, which could also contribute to this observation. Indeed, the measured results show greater variations as the initial mixture strength is increased.

The measured extinction stretch rates versus the initial mixture strength for N_2 diluted H_2 opposed tubular flames for both concave and convex curved cases are shown in Figure 41. Concave H_2-N_2/air flames with smaller radii are prone to extinction, i.e. flames extinguish at higher fuel concentrations; convex H_2-N_2/air flames with smaller radii are more resistant to extinction, i.e. flames can exist under lower fuel concentrations. It is also shown in Figure 41 that the convex opposed tubular flames are more resistant to extinction than the concave ones. The α value of the H_2-N_2 mixture is greater than unity, so the flame resides on the fuel side. Based on the above observations, given that the Lewis number of the H_2-N_2 mixture falls in the range of 0.33 - 0.42 (Table 4), which is much less than unity, two conclusions can be drawn: 1) concave (convex) curvature retards (promotes) combustion, and therefore leads to early (late) extinction; 2) Le_{cr} is greater than 0.4.

For hydrogen flames using helium as diluent, the fuel Lewis number is greater than unity and the flame resides in the oxidizer stream. Based on the argument above, flames with smaller radii of curvature will be more resistant to extinction. This is confirmed by the data shown in Figure 42, where the flames are always concave. Also shown in Figure 42 is

the extinction data for H_2-Ar/air flames. The H_2-Ar mixture has a fuel Lewis number much less than one, so again, the flames with bigger radii of curvature demonstrate higher extinction stretch rate at a given initial mixture strength.

Cellular Instability

Cellular structures in the opposed tubular non-premixed flames have been reported previously (Hu et al. 2007). However, no effort was made to quantify the onset conditions of the cellularity in the previous study. Following the same experimental procedure, these onset conditions are carefully recorded in this study. Extinction behavior is different for flames that demonstrate cellular instability. In most cases, local extinction at one angular location starts to develop and a stripped pattern is formed when the onset condition for cellularity is reached. As the initial mixture strength is decreased further, local extinction occurs at more than one angular location and flames with cell numbers vary from 1 to 4 are observed as shown in Figure 43. In Figure 43 (a) - (d), the top part of the flame viewed in the axial direction is partially blocked by the inner nozzle, so not all cellular structures are readily seen. The stripped patterns that shown in Figure 43 (e) and (f) are taken with the CCD video camera looking in the radial direction. The strips are steady at the given experimental conditions.

Only the onset conditions of cellularity are recorded, while no data was made available to relate the cell numbers to the flow conditions as great uncertainty has been experienced in the attempt to do so. The flame with only one cell is not stable and the flame

cell is always rotating. Both clockwise and counter-clockwise rotations are observed, which indicates the direction of rotation is random. Flames with 1, 3 and 4 cells show the preferred curvature property discovered previously (Hu et al. 2007), but not the flames with 2 cells.

Shown in Figure 44 are the onset boundaries of cellular structures and the regions where cellularity exists in the H_2-N_2/air opposed tubular flames with both concave and convex curvature. For ease of discussion, the initial mixture strength is plotted as functions of the stretch rate. Consistent with previous findings (Chen et al. 1992; Jacono et al. 2003), cellularity is only observed in flames close to extinction and with sufficiently low fuel stream Lewis numbers. At stretch rates not lying in the regions of extinction due to heat loss, regions of cellularity are becoming narrower as the stretch rates are raised higher. The cellularity region becomes wider as the radius of curvature is increased for the concave cases, which indicates that the concave curvature is suppressing cellularity. As discussed earlier, the concave curvature retards combustion process, and the flame exhibits lower flame temperature. Flames with smaller radii of curvature extinguish earlier if the initial mixture strength is decreased gradually, so the region that favors cellularity becomes smaller. The H_2-Ar/air and H_2-CO_2/air flame data shown in Figure 45 confirm this postulate by showing similar trends. This can also be verified by studying flames with opposite curvature. However, there are not enough data available for the convex cases due to experimental difficulties. More efforts are needed in the future.

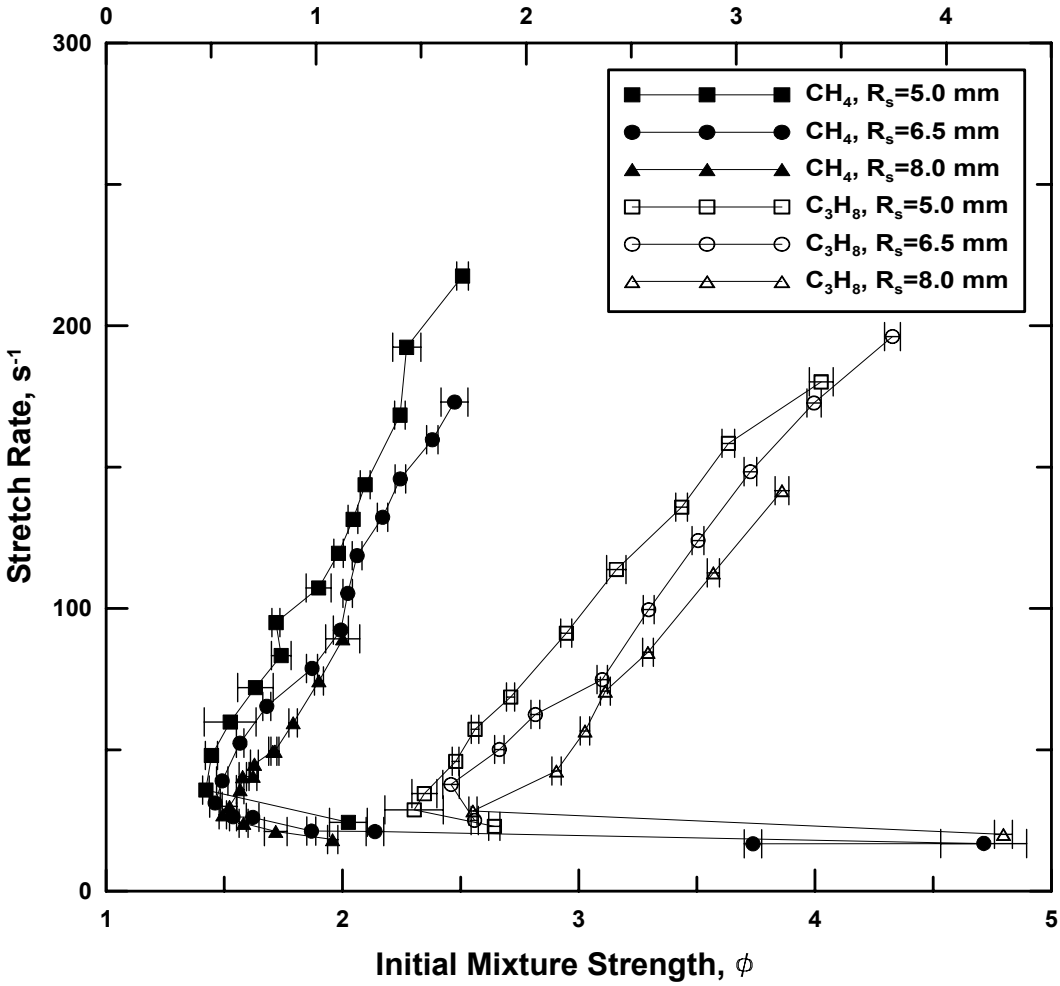

Figure 39 The extinction stretch rate of the opposed tubular flame as function of the initial mixture strength for various radii of the stagnation surface. Fuel: CH_4/C_3H_8; diluent: N_2; oxidizer: air. Note: CH_4 uses lower X-axis, C_3H_8 uses upper one

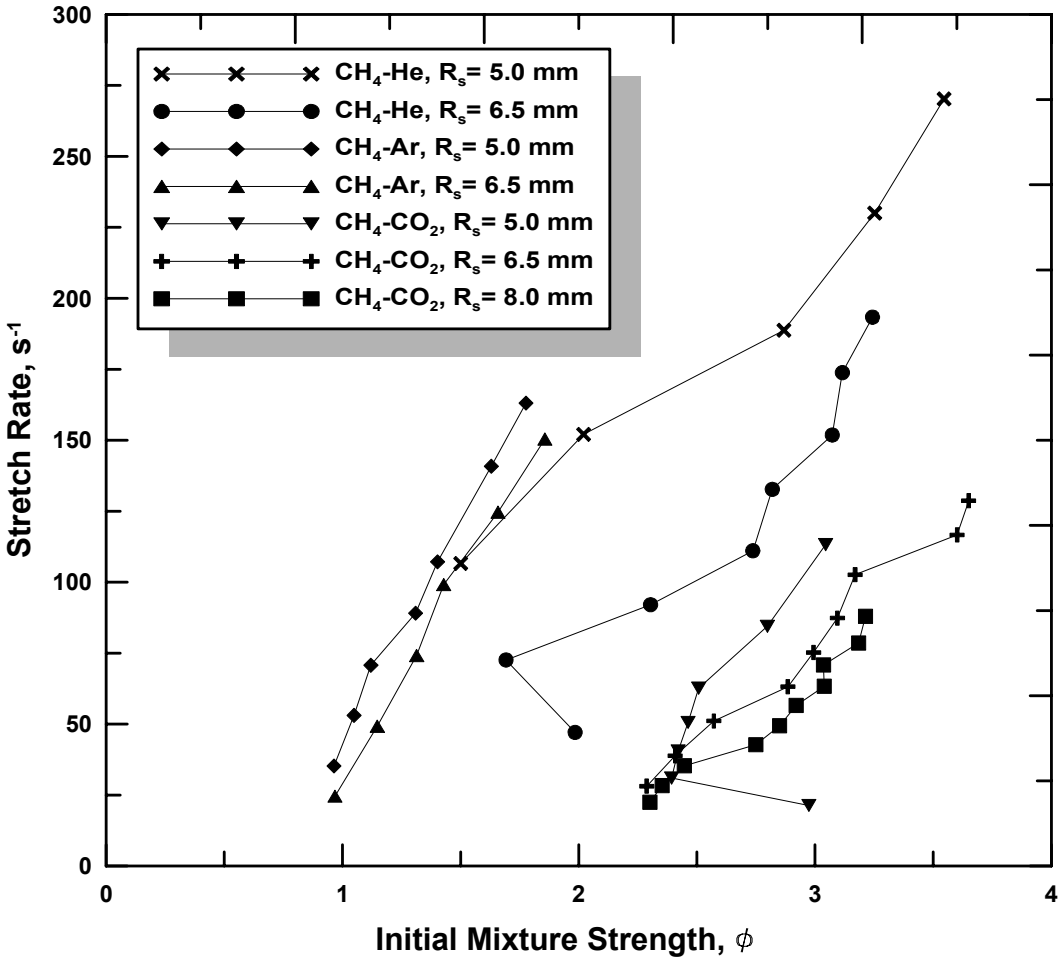

Figure 40 The extinction stretch rate of the opposed tubular flame as function of the initial mixture strength for two different radii of the stagnation surface and two different diluents. Fuel: CH_4; diluent: He/Ar/CO_2; oxidizer: air

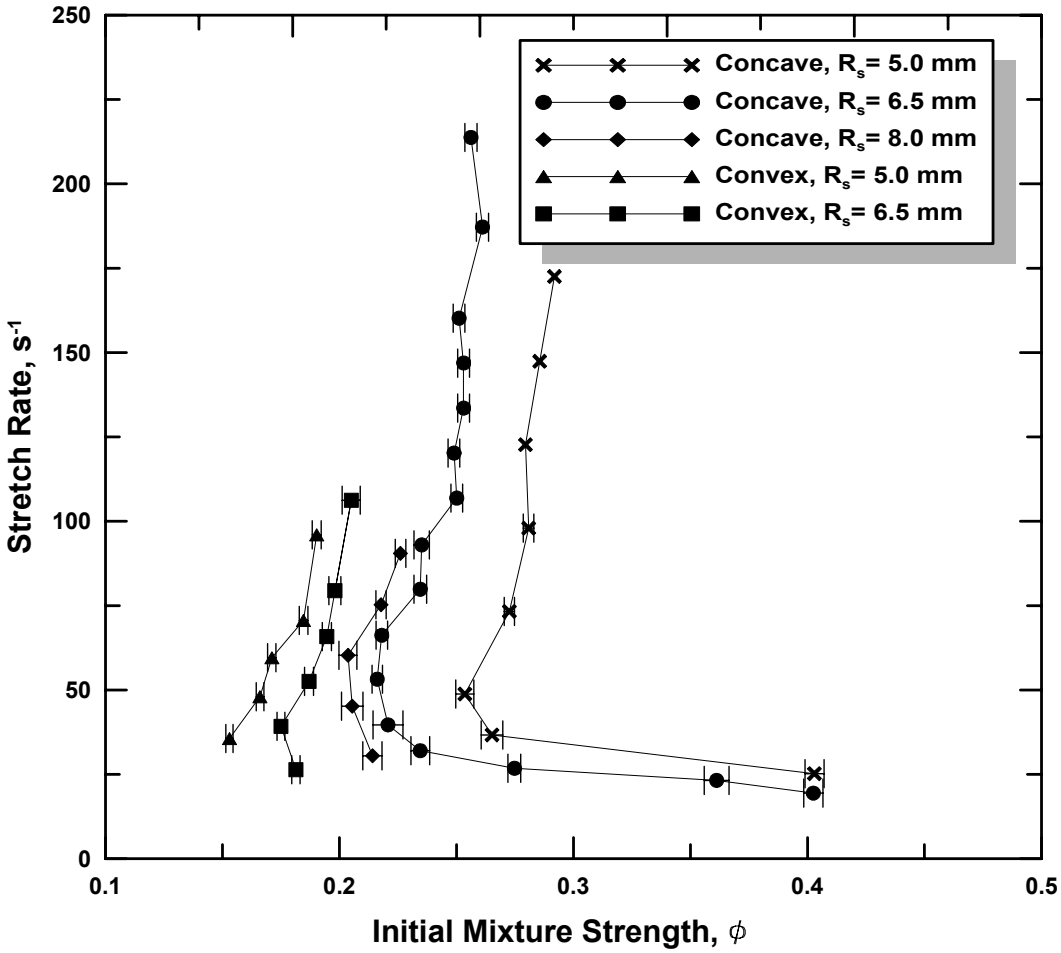

Figure 41 The extinction stretch rate of the opposed tubular flame as function of the initial mixture strength for various radii of the stagnation surface and different directions of curvature. Fuel: H_2; diluent: N_2; oxidizer: air

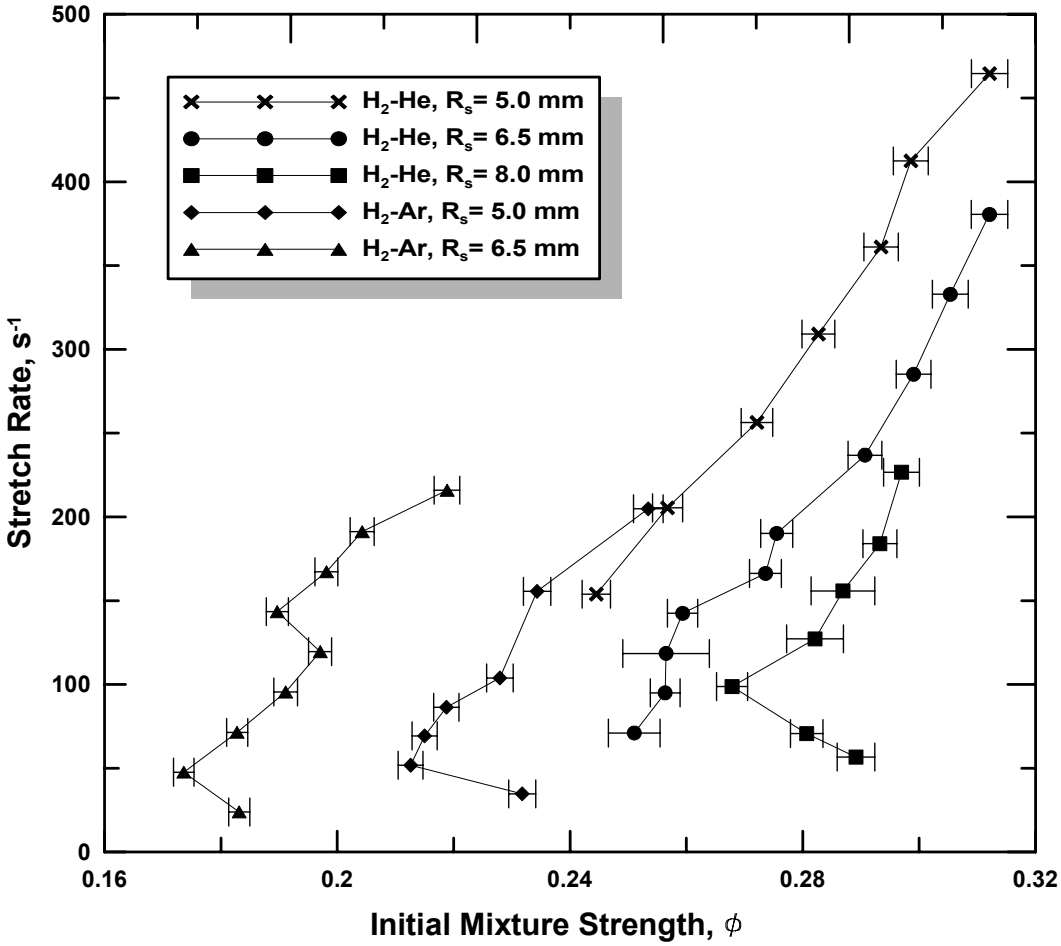

Figure 42 The extinction stretch rate of the opposed concave tubular flame as function of the initial mixture strength for various radii of the stagnation surface and two different diluents. Fuel: H_2; diluent: He/Ar; oxidizer: air

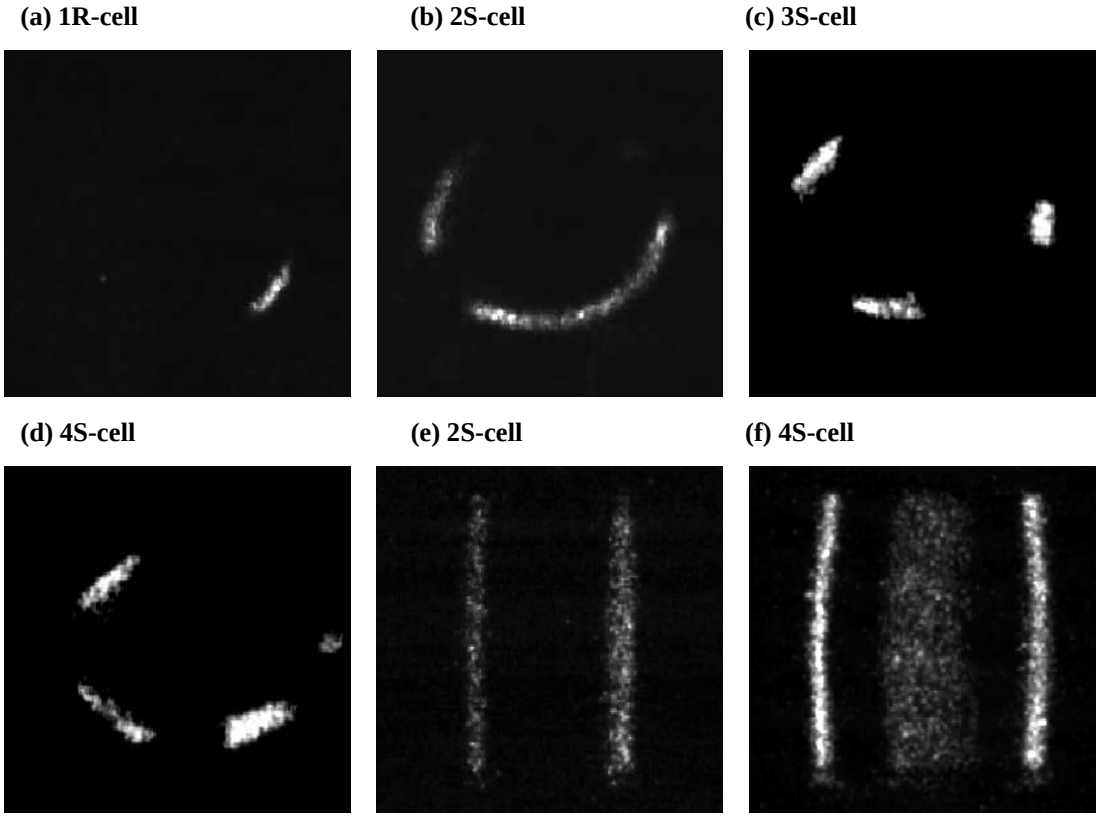

Figure 43 Images of the cellular structure of the diluted-H_2/air opposed tubular concave flame. (a) - (d): H_2-N_2 viewed in the axial direction; (e) and (f): H_2-CO_2 viewed in the radial direction. (a) ϕ = 0.271, K≈73 s-1, R_s≈5.0 mm; (b) ϕ = 0.281, K≈30 s-1, R_s≈8.0 mm; (c) ϕ = 0.217, K≈45 s-1, R_s≈8.0 mm; (d) ϕ = 0.236, K≈45 s-1, R_s≈8.0 mm; (e) ϕ = 0.410, K≈64 s-1, R_s≈5.0 mm; (f) ϕ = 0.398, K≈42 s-1, R_s≈6.5 mm. “R” represents rotating cells and “S” stationary ones.

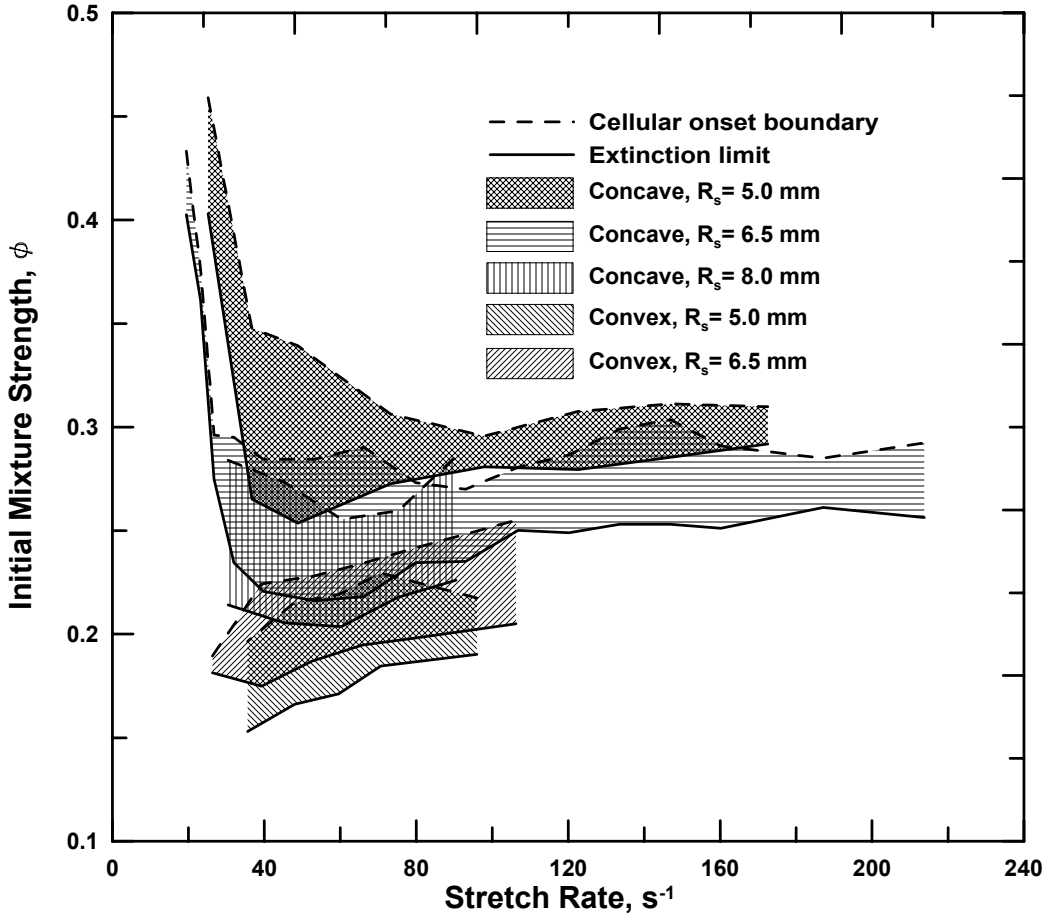

Figure 44 The onset initial mixture strength of cellular structures and the regions where cellularity exists for opposed tubular flames plotted as functions of stretch rate with both concave and convex curvature. Fuel: H_2; diluent: N_2; oxidizer: air

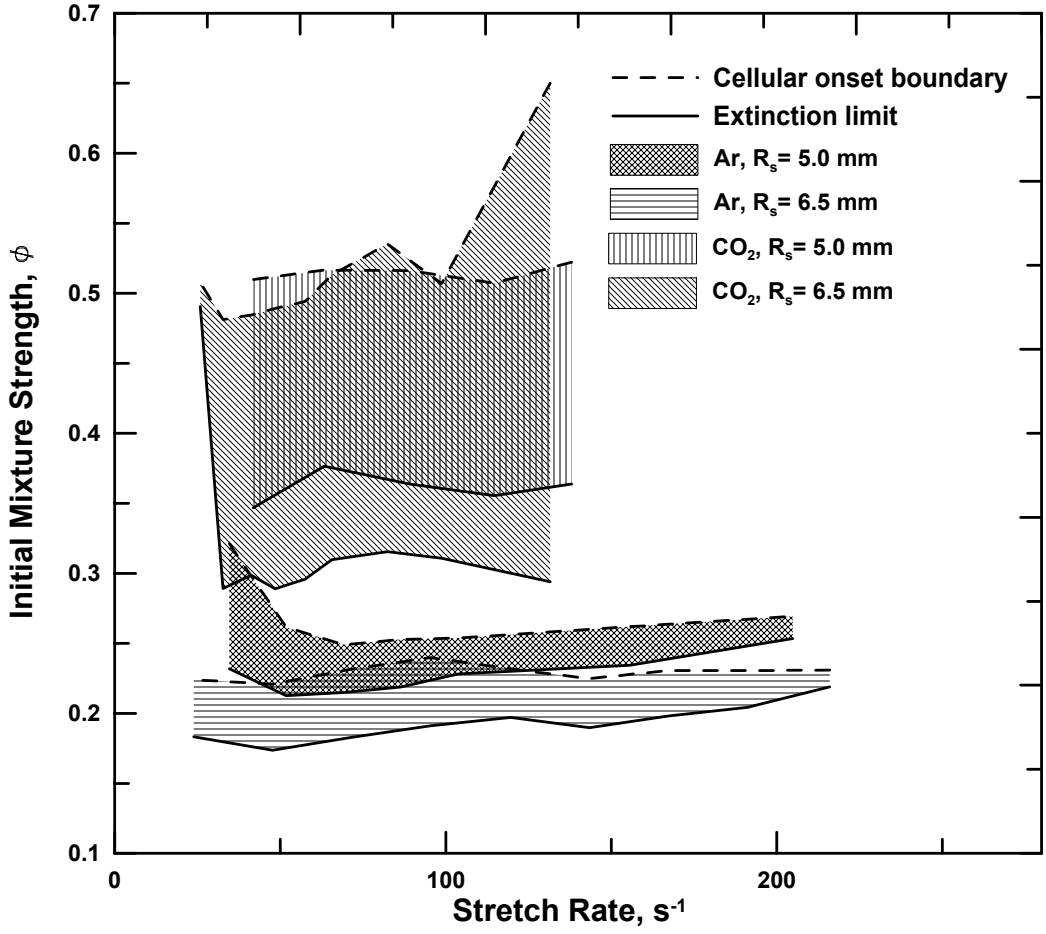

Figure 45 The onset initial mixture strength of cellular structures and the regions where cellularity exists for opposed concave tubular flames plotted as functions of stretch rate subject to different effects of curvature. Fuel: H_2; diluent: Ar/CO_2; oxidizer: air

Conclusion

A novel opposed tubular burner is used to study the curvature effects on extinction and cellularity of non-premixed flames. The extinction limits of opposed tubular flames burning various fuel (H_2, CH_4 or C_3H_8)/inert gases (N_2, He, Ar or CO_2) mixture with air are measured in terms of the initial mixture strength versus the stretch rate. The effects of curvature are studied by varying the radii of the flame curvature. From the data, it is discovered that the curvature effects are always coupled with the effects of the Lewis number. There exists a critical Lewis number Le_{cr}, which is less than unity such that when $Le < (>)$ Le_{cr}, the concave curvature retards (promotes) combustion and weakens (strengthens) the non-premixed flame; vise versa for the convex curvature. The value of Le_{cr} is between 0.4 and 1.

Cellular structures with 1 to 4 cells are observed in this study for flames with sufficiently-low fuel Lewis number. Quantitative onset conditions for cellularity in non-premixed tubular flames are measured. Regions of the observed cellular instability are mapped out in the initial mixture strength - stretch rate diagram. The effects of the concave curvature are to suppress the cellular instability as shown by comparing the maps of cellularity with different radii of curvature.

CHAPTER VI

CONCLUSIONS AND FUTURE EFFORTS

Summary and Conclusions

Non-premixed tubular flames are established using a uniquely-designed opposed tubular burner for the first time. Tubular hydrogen/, methane/ or propane/nitrogen-air non-premixed flames which are concave towards the fuel stream are established. A laser-induced Raman experimental system is developed and improved for diagnostics purposes. Visible laser-induced Raman spectroscopy is applied to all three kinds of flames to obtain temperature and major species concentration profiles. The flames studied include 15% H_2 diluted with N_2 against air with stretch rates ranging from 30 to 242 s^{-1}, 30% CH_4 diluted with N_2 against air with stretch rates ranging from 41 to 120 s^{-1}, and 15% C_3H_8 diluted with N_2 against air with stretch rates ranging from 33 to 100 s^{-1}. Due to the heat loss to the inner nozzle at low stretch rates and the flow unsteadiness introduced by turbulence at high stretch rates, only data for moderate stretch rates are presented. Temperature and species concentrations (H_2O, N_2, O_2, and H_2 for hydrogen flames; CO_2, H_2O, N_2, O_2, and CH_4 for methane flames; CO_2, H_2O, N_2, O_2, and C_3H_8 for propane flames) of these flames are obtained with good spatial resolution. In some of the methane and propane flames, only data on the oxidizer side are made available due to the interferences from the C_2 LIF and the scattering of the inner wall. This non-intrusive Raman system is also successfully ap-

plied to other types of flames by the author, such as tubular premixed (Hu et al. 2006b) and partially-premixed opposed-jet flames (Katta et al. 2007).

Numerical simulations of the non-premixed tubular flames corresponding to the experimental conditions are carried out using a modified Chemkin code written with FORTRAN. Detailed chemical reaction mechanisms are utilized for each individual fuel, which are Mueller (Mueller et al. 1999), Peters (Peters and Rogg 1993), and GRI 3.0 (Smith et al. 2000) mechanisms for hydrogen flames, Kee (Kee et al. 1985), C1 (Peters and Rogg 1993), C2 (Peters and Rogg 1993) and GRI 3.0 mechanisms for methane flames, and San Diego mechanism for propane flames. Complex molecular models of using either the multi-component or mixture-average formulation are incorporated in the simulation code together with detailed thermodynamic databases.

The experimental data and simulation results of each flame are compared with each other. The agreement is generally very good. The numerical models and the reaction mechanisms are validated by such a comparison. The peak flame temperature comparison between curved and planar flames (Figure 37) reveals the effects of curvature on non-premixed flames. Given the unity Lewis number of the air stream, the non-unity Lewis number of the fuel mixture controls the diffusion of the fuel to the flame surface. When Lewis number of the fuel stream is greater than one (C_3H_8/N_2), curvature concave toward the fuel stream promotes combustion (higher peak temperature) and convex curvature retards combustion (lower peak temperature); when the Lewis number of the fuel stream is much less than one (H_2/N_2), curvature concave toward the fuel stream retards combustion

(lower peak temperature) and convex curvature promotes combustion (higher peak temperature). The effects of curvature on curved methane flames are ambiguous, because the Lewis number of CH_4/N_2 mixture is close to one. Although the peak flame temperature of concave methane flame is lower than that of the planar flame, which indicates that the methane flames act like flames with Lewis number less than one, the peak flame temperature of the convex methane flame is almost the same as that of the planar ones, which indicates the effects of curvature is not important.

To further elaborate the above conclusion about flame curvature, extinction and cellular instability of the non-premixed tubular flames are studied. The extinction limits of opposed tubular flames burning various fuel (H_2, CH_4 or C_3H_8)/inert gases (N_2, He, Ar or CO_2) mixture against air are measured in terms of the initial mixture strength versus the stretch rate. The effects of curvature are studied by varying the radii of the flame curvature. From the data, it is discovered that the curvature effects are always coupled with the effects of the Lewis number. There exists a critical Lewis number Le_{cr}, which is less than unity such that when $Le < (>) Le_{cr}$, the concave curvature retards (promotes) combustion and weakens (strengthens) the non-premixed flame; vice versa for the convex curvature. The value of Le_{cr} is between 0.4 and 1.

Cellular structures with 1 to 4 cells are observed in non-premixed tubular flames with sufficiently-low fuel Lewis number. Quantitative onset conditions for cellularity in non-premixed tubular flames are measured. Regions of the observed cellular instability are mapped out in the initial mixture strength - stretch rate diagram. The effects of the concave

curvature are to suppress the cellular instability as shown by comparing the maps of flames with different radii of curvature.

The Effects of Curvature

To discuss the physical process on how curvature affects the non-premixed flames, one needs to start with the effects of stretch and preferential diffusion. The term preferential diffusion encompasses two meanings: the effects of Lewis number, that is, the changes in flame characteristics caused by difference in thermal diffusivity and molecular diffusivity, and the effects of differential diffusion, that is, the changes in flame characteristics caused by difference in the diffusivity of different molecules of the mixture. Considering a stretched planar flame, i.e. that of the opposed jet flame, as an example, if the Lewis numbers of both the fuel and oxidizer streams are equal to one and the diffusivities of different molecules of interest are equal, changes in the aerodynamic stretch do not affect the flame properties as long as the reactions are complete. However, continuous increase in stretch rate causes the residence time to decrease to a point where the rate of reaction can not keep up with the rate of the supply of the fresh reactants and the depletion of the reaction produces. Therefore, complete reaction does not hold and the flame temperature decreases as a result of this. Further decrease in stretch causes the flame to extinguish eventually. In the case of non-unity Lewis number and unequal molecular diffusivity, taking the H_2/N_2-air flame as an example where the Lewis number of fuel mixture is less than one and the hydrogen molecules diffuse faster than the nitrogen molecules, as the

flame stretch the effects of Lewis number is to increase the flame temperature is increased because the increase in hydrogen mass diffusion outpaces the increase in heat loss ($\alpha < D$); as the flame stretch is increased the effects of differential diffusion is also to increase the flame temperature because the higher concentration gradient of hydrogen than that of nitrogen provides a driving force to diffuse hydrogen at a higher rate to the flame zone, which in turn generates a locally under-diluted region. However, as the stretch rate is increased to a point where reaction incompleteness starts to take effects, the flame temperature decreases according to the process described in the unity Lewis number and equal mass diffusivity case. The question now is how curvature plays a role in affecting the flame properties.

Considering again a H_2/N_2-air flame, if the flame front is curved, the part that is concave toward the fuel stream has a focusing/defocusing effect on both the molecular diffusion and heat transfer. On one hand, the fuel is diffusing into a larger area, and therefore it's defocusing. The local hydrogen concentration is lower than that of the corresponding planar flame, or in other words, the flame front is over-diluted, so the flame temperature drops. On the other hand, the heat transfer is toward a smaller area, and therefore it's focusing. Due to the smaller heat capacity in the focused region, the temperature gradient is less than that of the corresponding planar flame, so the heat loss is reduced, which caused the temperature to increase. However, because the Lewis number is less than one, the defocusing of the reactant dominates. The overall effect of curvature in the concave case is to decrease the flame temperature. Similar argument shows that flame

temperature increases in the convex case. The extinction behavior of non-premixed curved flames can be explained by the temperature considerations based on the Lewis number, the different mass diffusivities, and the direction of curvature.

In the case of near-extinction curved flames, the flame has a tendency to sustain itself by deforming the flame front to generate high temperature regions. Taking H_2/N_2 concave tubular flame as an example, the near extinction flame breaks itself to form locally convex-curved flame stripes with higher temperature than that of the corresponding concave flames (See for example Figure 43-D). As a result, one observes the cellular instability in the curved flames reported in Chapter V.

Future Work

A new improved tubular burner has been designed and manufactured, which is detailed in Appendix A. With the improved burner, flames that are previously unstable and hard to generate using the old burner will be easily established, and thereby expand the operating range of the tubular burner. The new burner is compact, requires less gas flow and has Brewster-angle windows, which makes it more ideal for optical diagnostics. Further more, the flow field generated with this new burner will be more uniform and much easier to manipulate.

In combustion simulations, the concentrations of radicals and intermediate products are difficult to predict and yet their importance can not be underestimated. In most cases, it is the radicals who control the characteristics of the flame. In a recent study (Kortschik et al.

2005), laser-induced fluorescence (LIF) images in a corrugated counter flow mixing field using n-heptane versus air revealed that elevated concentrations of formaldehyde (CH_2O) concave toward the air side were in favor of autoignition, which is also confirmed by the numerical calculations. Another study (Nandula 2003) shown that the turbulent flamelet model over-predicted the hydroxyl concentrations in the shear layer upstream of a turbulent, lean, premixed combustor. In these regions, the curvature effects, which are not captured by flamelet model, might be important. A proposal for applying the OH LIF measurement to the opposed tubular flame is detailed in Appendix B along with a brief review of the LIF process and calibration procedure. The simultaneous measurement of temperature and major species concentrations using Raman spectroscopy and OH radical distribution using LIF technique will help to gain a better understanding of the curvature effects on flame structure. In addition to the experiments, numerical study can also be carried out, and the experimental data can be used to validate the numerical models.

The study of the extinction and cellular instability of the opposed-tubular flames in this work has revealed some very interesting phenomena. However, there are still many aspects in this area that deserve further investigation. Flame extinction and cellularity data with varying oxygen concentration can be obtained without any technical difficulties to study the effects of oxidizer Lewis number and curvature. With more carefully selected fuel and diluent combinations, experiments can be carried out to determine the critical Lewis number where the opposite curvature effects start to act on a curved flame. The effects of curvature on cellular instability can be further studied by taking more meas-

urements in both convex and concave flame cases. Numerical simulation of the cellular instability poses a great challenge, due to the intrinsic 2-D or even 3-D nature of the cellular structure. Some effort in this regards can be carried out to assist experiments and eventually obtain full understanding of the effects of curvature on flame extinction and cellular instability.

Partially premixed flames closely resemble the condition inside a direct-inject stratified charge (DISI) engine. Some interesting behavior of this types of flames at near-extinction conditions has been discovered (Katta et al. 2007). The effects of curvature on partially-premixed tubular flames have yet to be defined and deserve some attention.

APPENDIX

A. Design of a New Tubular Burner

Design Criteria

In the opposed tubular burner, one of the reactants is introduced radially inward through the outer nozzle and the other reactant is issued radially outward through the inner nozzle (Figure 3). By installing a porous nozzle assembly, an existing tubular burner (Mosbacher et al. 2002) was modified to generate non-premixed tubular flame presented in Chapter IV. However, some limitations of this burner, including non-uniform flow, fixed outer nozzle size and height, etc., made the proposed investigation of the tubular flames difficult to implement. To overcome the shortcomings of the previous burner, a new opposed tubular burner was designed, fabricated and tested. Similar to the previous one, the new burner has three optical ports around the peripheral of the burner to allow optical access, two of which are aligned along a straight line perpendicular to the third (Figure 46). In order to maintain a simple flow field, certain design criteria have to be met and these are discussed below.

The gas flow velocities at the exits of both the outer and inner nozzles need to be uniform in order for the one-dimensional simplification described in a later section to be valid (Dixon-Lewis et al. 1990). The boundary condition under this situation is termed plug-flow boundary condition. In the design of wind tunnel contraction section, research-

ers have found that the area contraction ratio (CR) needs to be greater than 10 to produce a uniform flow (Tsien 1943; Morel 1975). This criterion was followed in the design of the tubular burner here. Simulations (2-D) using the commercial software Fluent have shown that as long as this criterion is satisfied, the velocity distribution at the nozzle exit is not very sensitive to the shape of the nozzle surface. As a result, a 3rd order polynomial was conveniently chosen to describe the surface contour.

On the other hand, the diameter-height ratio of the nozzle has been found to be important in determining the shape of the velocity distribution at the nozzle exit. Large ratios favor uniform flow. However, if this ratio is too large, the scattered light from the sample volume, which originates from the burner center, will be partially blocked by the nozzle. As a result, the diameter-height ratio was chosen to be 3 for optimal performance.

The desired exit velocity from the experimental points of view falls between 0.2 - 5 m/s with the maximum corresponds to the typical extinction velocity. The flow rate capacity of the flow meters commercially available is 0.1 - 500 SLPM. Due to practical considerations, the desired flow rate should be in the range of 30 - 300 SLPM. As a result, the area of the nozzle exit should be less than 0.001 m^2. Given the diameter-height ratio of 3, the outer nozzle radius R_2 needs to satisfy $R_2 < 15.5$ mm.

The Reynolds number for the tubular burner configuration can be defined as $\mathrm{Re} = VD_h/\upsilon$, where D_h equals $H/2$ in this case and υ is approximately 0.16 cm^2/s for air at 300 K, 1 atm. From a previous study, the maximum allowable Reynolds number for the tubular burner configuration before the appearance of flow turbulence is ~4000 (Hu et

al. 2006b). Given the diameter-height ratio of 3, one can infer that the nozzle radius R needs to meet this requirement: $R_2 < 96/V_{\max} = 19.2$ mm.

For premixed tubular flame, the measured extinction stretch rates, k_{ext}, for stoichiometric methane-air and propane-air flames are close to 2400 s^{-1} (Kobayashi and Kitano 1993). This can be deemed as the maximum stretch rate the tubular burner needs to produce. Given the definition of stretch rate for tubular burner, $k = \pi V / R_2$, one could establish a relationship for the nozzle radius, $R_2 > \pi V_{\max} / 2400 = 6.5$ mm.

Based on the above analysis, $R_2 = 12$ mm was chosen in the design process. This value can be changed, because the newly designed burner has exchangeable nozzles, which will be discussed later. The outer radius of the contoured nozzle is 76 mm with a height of 72 mm. The area contraction ratio, 57, is well above the minimum requirement. The design parameters and their corresponding criteria are summarized in Table 5.

Table 5 Tubular burner design parameters and their corresponding criteria

Parameter	**Value**	**Criteria**
CR	57	>10
Diameter-height ratio	3	Velocity uniformity and optical accessibility
R_2	12 mm	$6.5 < R_2 < 15.5$
R_1	3.2, 4.8 mm	Prominent curvature effects and reactant delivery

The inner nozzle is made of sintered metal porous tubes, which ensure flow uniformity. Three sections are welded together. Main reactant flow is through the middle section and inert gas co-flows are through the two end sections. The co-flows are necessary to avoid preheating of the reactant delivery tube to the middle section, as well as shield the

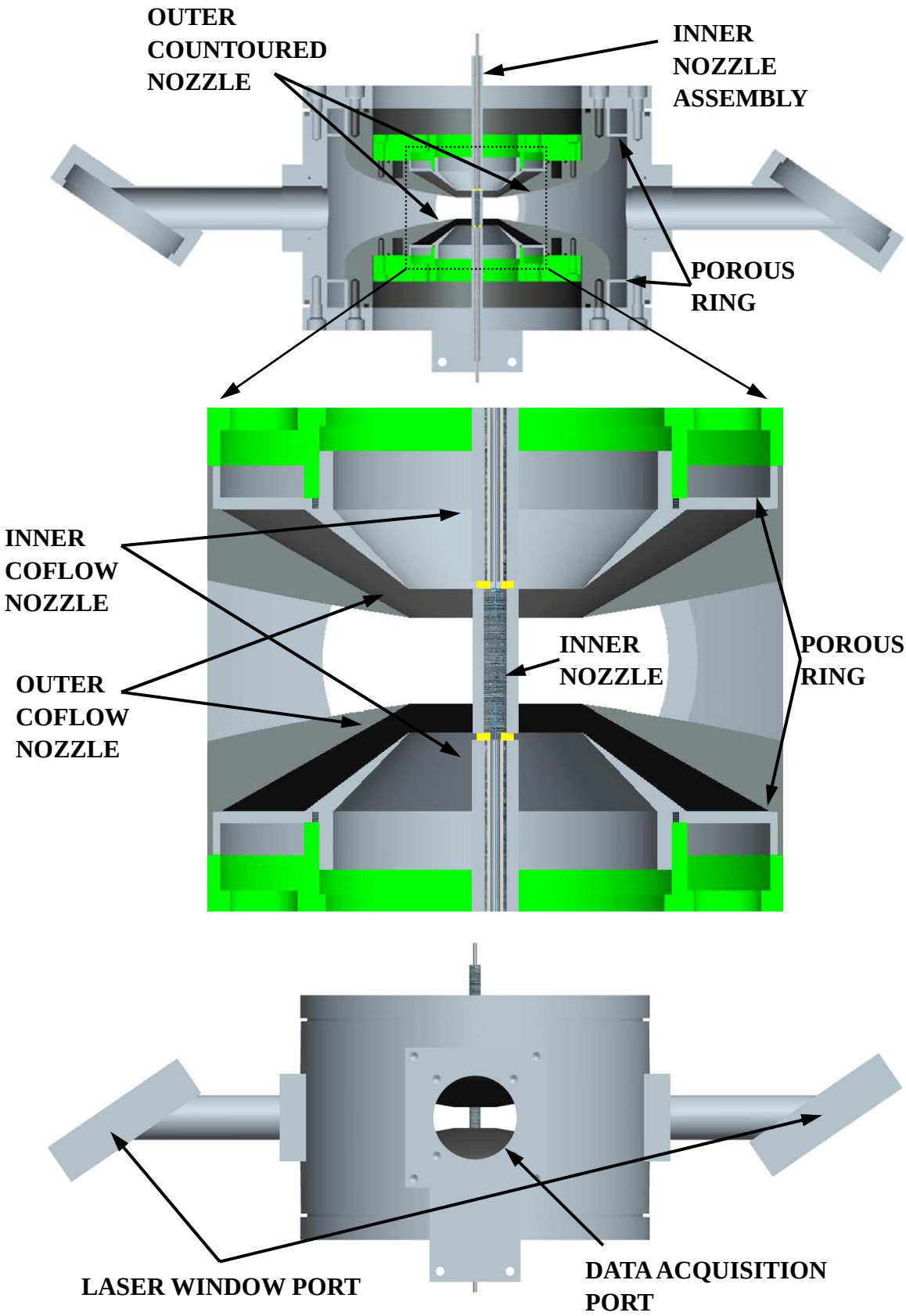

Figure 46 Assembly drawing of the opposed tubular burner

flame from surrounding environment to minimize disturbance. Laser welding is used to minimize the gap between each section. The curvature effects on flames are more prominent when the radius of curvature is smaller. This necessitates tubes with diameters as small as possible to be employed. On the other hand, to maintain a substantial amount of gas flow through the middle section of the inner nozzle, the diameter of the delivery tubes cannot be too small. This puts a lower limit on the size of the sintered metal tubes, which is around 3 mm. In this study, tubes with $R_1 = 3.2$ mm are used in most cases.

The outer nozzle of the burner is also accompanied with inert gas co-flows for the same reason mentioned above. In non-premixed flames, the flame thickness could vary substantially depending on the flow field, types of reactants and flame temperature, the later of which is in turn affected by the reactant dilution ratio. In order to avoid temperature and species gradient at both the outer and inner boundaries, one needs to use an outer nozzle with an appropriate diameter for each characteristic flame. In order to meet this requirement, the outer nozzle of the tubular burner is designed to be exchangeable. Two porous metal rings are installed to maintain a favorable pressure drop across the gas inlets and the chamber (Figure 46). This ensures the gas flow into the burner chamber is uniform. Similar measure is adopted for the outer coflow nozzles.

Windows for the two laser ports are mounted at their Brewster angle (Figure 46) to maximize the throughput of the vertically polarized laser light and at the same time minimize reflection inside the burner chamber. As a result, the stray light picked by the camera is minimized, which improves the accuracy of the measurement.

Flow Field Simulation

To assess the performance of the tubular burner, the CFD software Fluent is utilized to simulate the non-reacting flow fields for both the non-premixed and premixed configurations. In the simulation, the effects of optical ports on the flow field are believed to be minimal. This simplifies the problem to a 2-D axisymmetric one. The mesh used in the calculation is shown in Figure 47. The pressure outlet is set to be far away from the actual location in order to avoid any outlet effects (Poinsot and Veynante 2001). The black line and curves in the figure designate the actual walls of the burner. The burner is divided into 160 grid points along the symmetry plane and 180 grid points along the axis of symmetry. The grid density is increased at the vicinity around the nozzle exits to improve the accuracy of the simulation. The segregated, steady solver is used and the momentum equation is differentiated using a first order upwind scheme. In the subsequent simulations, the burner outer and inner radii are chosen to be 12 and 3 mm, respectively.

The velocity distributions at various radial locations of the opposed tubular burner with $V_2 = 1$ m/s, $V_1 = 2$ m/s and no coflow as an example are shown in Figure 48. Although velocity is not quite uniform at the exit of the outer nozzle (r = 12 mm), it demonstrates very good uniformity at reduced radial locations. In addition, a central region with flat velocity distribution for all radii is observed from the simulation as shown in Figure 48. In laser-induced Raman scattering and LIF measurements, the laser beam is passing through the symmetry plane (axial location z = 0 mm). The existence of such a uniform

central region validates the measurement as well as the 1-D assumption described in the next section for the numerical simulation of non-premixed flames with detailed chemistry and transport formulation.

Results from the 2-D flow field simulations is further compared to the analytical solution using the 1-D assumption (Wang et al. 2006b) in Figure 49, where the stretch rate profile is described by the following expressions (assuming equal density in the two nozzles):

for $R_s < r < R_2$

$$k = -V_2/R_2\sqrt{Q}\cos\left[\sqrt{Q}(r/R_2)^2/2 + \pi/2 - \sqrt{Q}/2\right] \quad \text{(A.1)}$$

for $R_1 < r < R_s$

$$k = -V_2/R_2\sqrt{Q}\cos\left[\sqrt{Q}(r/R_2)^2 V_2R_2/(2V_1R_1) + \pi/2 - \sqrt{Q}V_2R_1/(2V_1R_2)\right] \quad \text{(A.2)}$$

where $\sqrt{Q}$ is given by:

$$\sqrt{Q} = \pi\left[(R_2/R_1 - V_1/V_2)/(R_2/R_1 - R_1/R_2)\right] \quad \text{(A.3)}$$

and R_s is calculated by:

$$R_s = \left[1 - (R_2/R_1 - R_1/R_2)/(R_2/R_1 - V_1/V_2)\right]^{1/2} \quad \text{(A.4)}$$

The comparison demonstrates approximately 10% difference in maximum stretch rates between the theoretical and simulation profiles. From the simulation, an effective nozzle radius equal to 15 mm is directly obtained from the interception point between the stretch rate curve and the radial location axis. The effective exit velocity is calculated to be 1.25 m/s based on the change in areas. The theoretical stretch rate profile based on the effective values is shown as dashed line in Figure 49. Very good agreement has been found

between the simulation and theory on the maximum stretch rate. The better agreement of the stretch rate curves on the inner nozzle side is not surprising as the plug flow description is believed to be exact here. This effective radius will be used in future data reductions. The influence of coflow is also studied by varying their exit velocities. The result shown in Figure 49 demonstrates a negligible influence from the coflow.

Comparison of the theoretical and 2-D simulated flow fields for the premixed burner configuration is also carried out and shown in Figure 50. The inner nozzle is removed and gas is introduced from the outer nozzle only. The stretch rate in this case is given by:

$$k = -\pi V_2 / R_2 \cos\left[\pi (r/R_2)^2\right] \tag{A.5}$$

Strong influence from the coflow is observed and a matching coflow velocity provides the best agreement between the theoretical and simulated results. It is therefore recommended in both premixed and non-premixed cases that one should operate the burner with coflow velocity matching its corresponding nozzle velocity.

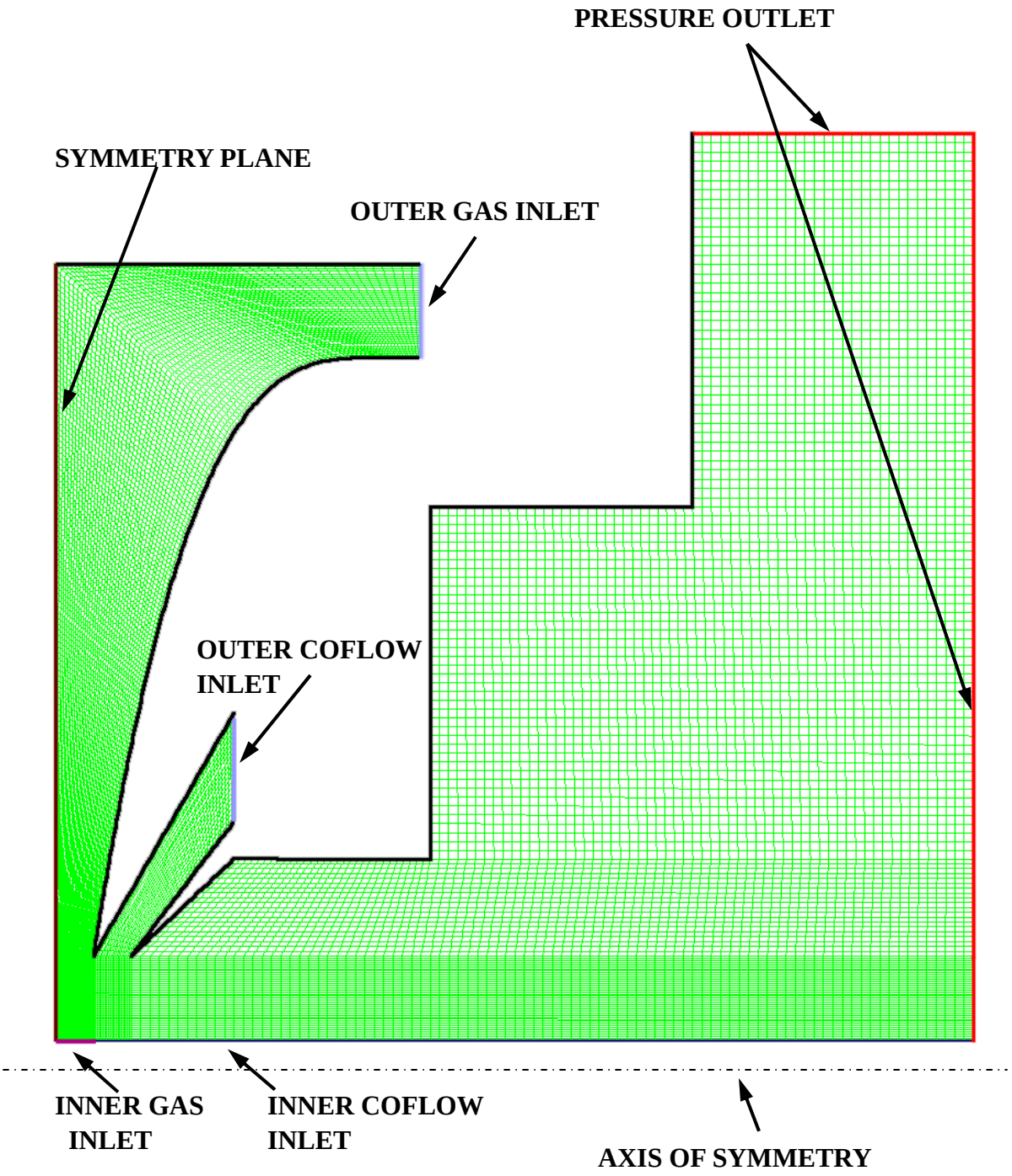

Figure 47 Mesh for the 2-D flow field simulation

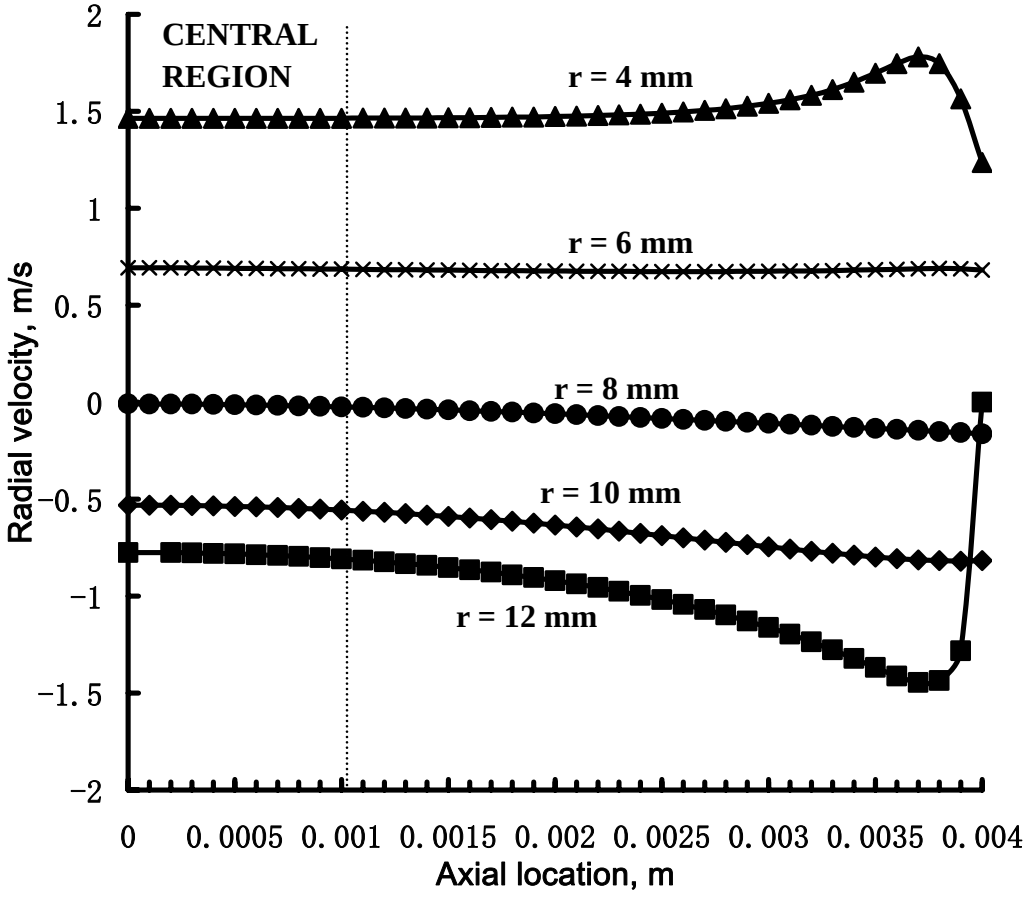

Figure 48 Velocity distributions at various radial locations of the opposed tubular burner for $V_2 = 1$ m/s, $V_1 = 2$ m/s and no coflow

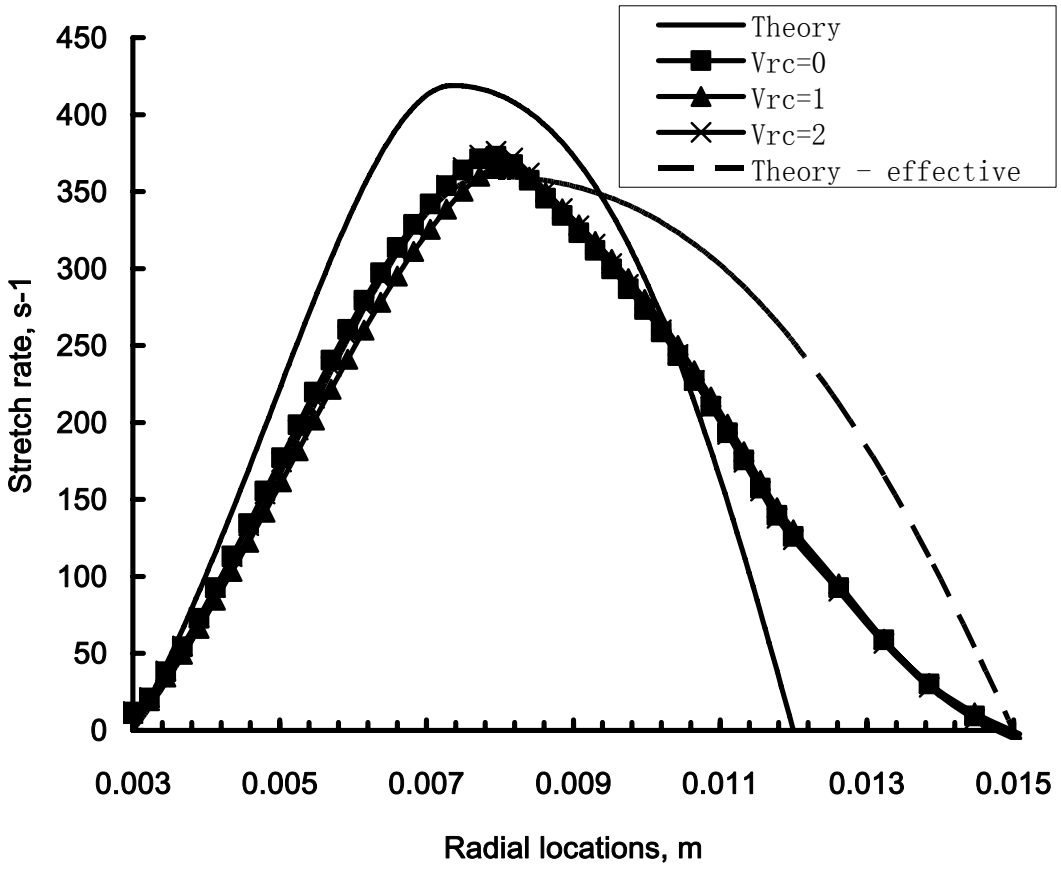

Figure 49 Comparison of the stretch rate profiles of the opposed tubular burner between theoretical and calculated results for $V_2 = 1$ m/s, $V_1 = 2$ m/s and various coflow velocities. Vrc represents the velocity ratio between the coflow and its accompanying nozzle.

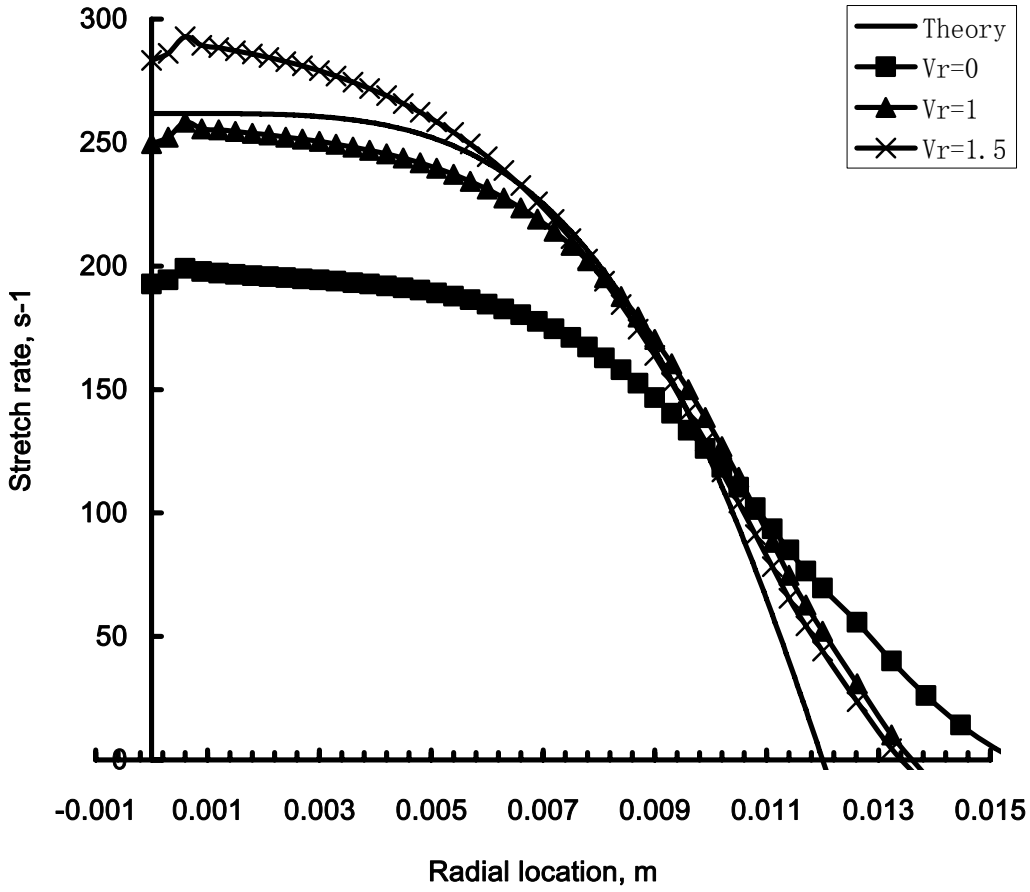

Figure 50 Comparison of the stretch rate profiles of the tubular burner between theoretical and calculated results for $V_2 = 1$ m/s and various coflow velocities. Vr represents the ratio between the coflow and the nozzle velocities.

B. OH LIF System

Background Theory

Fluorescence is the spontaneous emission of light from an excited atom or molecule. In laser-induced fluorescence (LIF), an atom or molecule reaches the excited state through photon absorption. This technique is typically utilized for the detection of chemically reactive intermediates and radicals (Eckbreth 1996). It is possible to get two- and three-dimensional images since fluorescence takes place in all directions (i.e. the fluorescence signal is isotropic). The signal-to-noise ratio of the fluorescence signal is very high, providing a good sensitivity to the process. It is also possible to distinguish between many species, since the lasing wavelength can be tuned to a particular excitation of a given species, which is not shared by other species. All these advantages make LIF ideal for detection of intermediate species at low concentration levels, e.g. ppm or even sub-ppm level.

Unfortunately, molecules at the excited states are subject to other losses, such as collisional quenching, photoionization and/or predissociation. To obtain quantitatively accurate concentration, all the losses need to be accounted accurately. While photoionization and predissociation can be avoided by picking an appropriate laser wavelength that corresponds to a non-dissociating excited state, collisional quenching is much more difficult to estimate due to its dependence on the temperature and all species present. In this study, the temperature and major species concentration are well determined by Raman scattering.

As a result, the quenching corrections can be calculated based on the Raman data.

If a two-level model is employed with photoionization and predissociation neglected, assuming the spontaneous emission is much slower than the collisional quenching the following expression is obtained for the power of the fluorescence signal, F, at low laser excitation irradiances (Eckbreth 1996):

$$F = \frac{h\nu}{c}\frac{\Omega}{4\pi} LAN_1^0 B_{12} I_\nu \frac{A_{21}}{Q_{21}} \tag{B.1}$$

The fluorescence is linearly proportional to the input laser irradiance in the so-called linear regime. The collisional quenching rate constant can be calculated from:

$$Q_{21} = \sum_i k_{Q_i} n_i \tag{B.2}$$

The quenching rate coefficient, K_{Q_i}, can be evaluated by

$$K_{Q_i} = \sigma_{Q_i} \left[8kT/(\pi\mu)\right]^{1/2} \tag{B.3}$$

where μ is the reduced mass of the colliding species.

To calculate the absolute number density of OH radicals directly, all the coefficients involved in Eq. B.1-3 need to be accurately determined, which is proven to be not feasible. An alternative approach is to use a calibration flame, similar to the Raman scattering method. Details is covered in the later sections.

Experimental Setup

The OH LIF technique is used to measure the OH concentration. A schematic of the OH LIF system is shown in Figure 51. A Nd:YAG pumped dye laser is used as the laser

source. The dye laser beam is frequency-doubled by a UV tracker (UVT) to produce laser beam in the UV range that accesses one of the excitation band of OH radical. For this work, the $O_{12}(8)$ transition in the $A^2\Sigma^+ \leftarrow X^2\Pi(1,0)$ band of OH ($\lambda = 287.9nm$) is picked to minimize the absorption of the laser beam propagating through the flame (Carter and Barlow 1994). The laser light is attenuated by a neutral density filter to ensure the LIF process is within the linear regime. The same focusing lens (300 mm focal length) as that used in Raman system is used to focus the beam into the tubular burner. For the OH fluorescence detection, light from the sample volume is collected at 90 degrees by an ICCD camera. Two filters: a Scott bandpass UG-5 (passes $250 < \lambda < 400nm$) and longpass WG305 filters (passes $\lambda > 305nm$) are placed in front of the camera to reject the scattered radiation and transmit fluorescence from the dominant (1,1), (1,0) and (0,0) bands. The whole system is gated by a DG535 gate/delay generator.

Calibration

To obtain absolute species concentrations without evaluating all the coefficients in Eq. B.1, the OH LIF system is calibrated using flames with known species concentrations. The Hencken burner is employed to replace the tubular burner in the test section. A single near-stoichiometric CH_4-air flame is produced by the burner and used in calibration.

The OH calibration factor, which is assumed to be independent of temperature, is obtained through the calibration procedure and defined as:

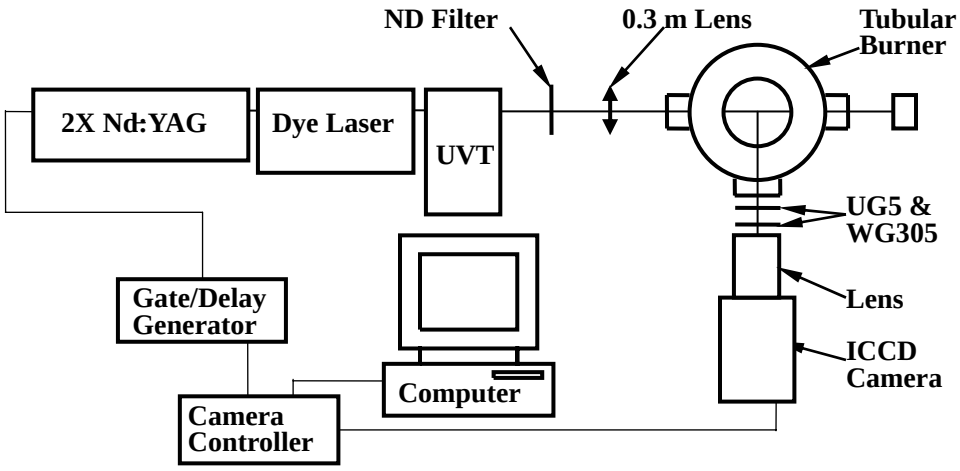

Figure 51 Schematic of the OH LIF system

$$C_{OH} = N_{1,cal}^{0} E_l \big/ \xi_{OH,cal} \tag{B.4}$$

where ξ_{OH} is the camera counts for OH signal, which is proportional to the fluorescence signal power F. Subscript cal denotes the calibration flame. The ground state population, N_1^0, is evaluated from Boltzmann statistics and depends on the OH number density and temperature. Since the tubular flame is very small and the (1,0) excitation is selected, radiation trapping of the signal is negligible (Eckbreth 1996).

The absolute OH concentration from the experimental data can be evaluated from:

$$n_{OH} = C_{OH} C_Q \xi_{OH} \big/ f_1^0 E_l \tag{B.5}$$

where f_1^0 is the ground-state population fraction calculated from the Raman-reduced temperature and $C_Q = Q_{21} / Q_{21,cal}$ is the correlation factor accounting for variation of the local collisional quenching from that at the calibration condition. The quenching correlation factor can be evaluated using Eq. B.2 and B.3, where the quenching cross section is calculated by $\sigma_Q = P_A C_0 \left[(1+h_c) \exp(-h_c) + C_1 h_c^{2/\alpha} \gamma(2-2/\alpha, h_c) \right]$ (Paul 1994), where $h_c = C_2 T_{cal} / T$, and $\gamma(a,x)$ is the incomplete gamma function. The coefficients defined in Eq. B.6 are listed in Table 6.

Table 6 Quenching coefficient of OH $A^2\Sigma^+(v'=0)$ (Paul 1994)

Molecule	P_A	C_0 (Å)	C_1	C_2	α
H	1.038	13.763	1.347	1.399	4.00
O	1.000	13.959	1.452	2.067	5.20
H_2	0.330	12.848	1.360	3.079	3.50
O_2	0.537	14.892	1.327	3.866	3.95
CO	0.846	14.536	1.664	6.206	4.60
CO_2	0.770	15.418	1.391	8.205	3.22
H_2O	1.120	15.955	2.251	4.302	3.12

CH_4	0.826	16.561	1.109	3.591	3.050
N_2	0				

REFERENCES

Barlow, R. S., C. D. Carter and R. W. Pitz (2002). Multiscalar Diagnostics in Turbulent Flames, New York, Taylor & Francis.

Bilger, R. W. (2000). "Future Progress in Turbulent Combustion Research." Progress in Energy and Combustion Science 26: 367-380.

Brown, T. M., M. A. Tanoff, R. J. Osborne, R. W. Pitz and M. D. Smooke (1997). "Experimental and Numerical Investigation of Laminar Hydrogen-Air Counterflow Diffusion Flames." Combustion Science and Technology 129: 71-88.

Bundy, M., A. Hamins and K. Y. Lee (2003). "Suppression Limits of Low Strain Rate Non-Premixed Methane Flames." Combustion and Flame 133: 299-310.

Carter, C. D. and R. S. Barlow (1994). "Simultaneous Measurements of No, Oh, and the Major Species in Turbulent Flames." Optics Letters 19(4): 299-301.

Cheatham, S. and M. Matalon (2000). "A General Asymptotic Theory of Diffusion Flames with Application to Cellular Instability." Journal of Fluid Mechanics 414: 105-144.

Chelliah, H. K., C. K. Law, T. Ueda, M. D. Smooke and F. A. Williams (1990). "An Experimental and Theoretical Investigation of the Dilution, Pressure and Flow-Field Effects on the Extinction Condition of Methane-Air-Nitrogen Diffusion Flames." Proceedings of the Combustion Institute 23: 503-511.

Chen, C. L. and S. H. Sohrab (1991). "Simultaneous Effects of Fuel/Oxidizer Concentrations on the Extinction of Counterflow Diffusion Flames." Combustion and Flame 86: 383-393.

Chen, R.-H., G. B. Mitchell and P. D. Ronney (1992). Diffusive-Thermal Instability and Flame Extinction in Nonpremixed Combustion. Proceedings of the Combustion Institute, 24: 213-221.

Chung, S. H. and C. K. Law (1983). "Structure and Extinction of Convective Diffusion Flames with General Lewis Numbers." COMBUSTION AND FLAME 52: 59-79.

Coelho, P. J. and N. Peters (2001). "Unsteady Modelling of a Piloted Methane/Air Jet

Flame Based on the Eulerian Particle Flamelet Model." Combustion and Flame 124(3): 444-465.

Coelho, P. J., O. J. Teerling and D. Roekaerts (2003). "Spectral Radiative Effects and Turbulence/Radiation Interaction in a Non-Luminous Turbulent Jet Diffusion Flame." Combustion and Flame 133(1-2): 75-91.

Cuenot, B. and T. Poinsot (1996). "Asymptotic and Numerical Study of Diffusion Flames with Variable Lewis Number and Finite Rate Chemistry." Combustion and Flame 104: 111-137.

Darabiha, N. and S. Candel (1992). "The Influence of the Temperature on Extinction and Ignition Limits of Strained Hydrogen-Air Diffusion Flames." Combustion Science and Technology 86: 67-85.

Dixon-Lewis, G., T. David, P. H. Gaskell, S. Fukutani, H. Jinno, J. A. Miller, R. J. Kee, M. D. Smooke, N. Peters, E. Effelsberg, J. Warnatz and F. Behrendt (1984). Calculation Fo the Structure and Extinction Limit of a Methane-Air Counterflow Diffusion Flame in the Forward Stagnation Region of a Porous Cylinder. Proceedings of the Combustion Institute, 20: 1893-1904.

Dixon-Lewis, G., V. Giovangigli, R. J. Kee, J. A. Miller, B. Rogg, M. D. Smooke, G. Stahl and J. Warnatz (1990). "Numerical Modeling of the Structure and Properties of Tubular Strained Laminar Premixed Flames." Progress in Astronautics and Aeronautics 131: 125-144.

Dongworth, M. and A. Melvin (1976). "Transition to Instability in a Steady Hydrogen-Oxygen Diffusion Flame." Combustion Science and Technology 14: 177-182.

Eckbreth, A. C. (1996). Laser Diagnostics for Combustion Temperature and Species. 2nd ed., Gordon and Breach Science Publishers.

Finke, H. and G. Grünefeld (2000). An Experimental Investigation of Extinction of Curved Laminar Hydrogen Diffusion Flames. Proceedings of the Combustion Institute, 28: 2133-2140.

Fristrom, R. M. and A. A. Westenberg (1965). Flame Structure, McGraw-Hill.

Glassman, I. (1996). Combustion. 3rd ed., Academic Press.

Greenberg, J. B. and F. Grodek (2003). "Curvature Effects in Burke-Schumann Spray

Flame Extinction." AIAA Journal 41(8): 1507-1513.

Hasse, C. and N. Peters (2005). A Two Mixture Fraction Flamelet Model Applied to Split Injections in a Di Diesel Engine. Proceedings of the Combustion Institute, 30: 2755-2762.

Haworth, D. C., M. C. Drake and R. J. Blint (1988). "Stretched Laminar Flamelet Modeling of a Turbulent Jet Diffusion Flame." Combustion Science and Technology 60(4-6): 287-318.

Heyl, A. and H. Bockhorn (2001). "Flamelet Modeling of No Formation in Laminar and Turbulent Diffusion Flames." Chemosphere 42(5-7): 449-462.

Hilbert, R., F. Tap, H. El-Rabii and D. Thévenin (2004). "Impact of Detailed Chemistry and Transport Models on Turbulent Combustion Simulations." Progress in Energy and Combustion Science 30: 61-117.

Http://maeweb.ucsd.edu/~combustion/cermech/ (2005/06/15).

Hu, S., P. Wang and R. W. Pitz (2006a). Curvature Effects in Non-Premixed Tubular Flames. 44th AIAA Aerospace Sciences Meeting and Exhibit, AIAA-2006-1133, Reno, NV.

Hu, S., P. Wang and R. W. Pitz (2006b). A Structural Study of Premixed Tubular Flames. 44th AIAA Aerospace Sciences Meeting and Exhibit, AIAA-2006-0160, Reno, NV.

Hu, S., P. Wang, R. W. Pitz and M. D. Smooke (2006c). Experimental and Numerical Investigation of Non-Premixed Tubular Flames. Proceedings of the Combustion Institute, 31, in press.

Hu, S., P. Wang, R. W. Pitz and M. D. Smooke (2007). "Experimental and Numerical Investigation of Non-Premixed Tubular Flames." Proceedings of the Combustion Institute 31: 1093-1099.

Im, H. G., C. K. Law and R. L. Axelbaum (1990). Opening of the Burke-Schumann Flame Tip and the Effects of Curvature on Diffusion Flame Extinction. Proceedings of the Combustion Institute, 23: 551-558.

Ishizuka, S. (1982). An Experimental Study on the Opening of Laminar Diffusion Flame Tips. Proceedings of the Combustion Institute, 19: 319-326.

Ishizuka, S. (1984). On the Behavior of Premixed Flames in a Rotating Flow Field: Establishment of Tubular Flames. Proceeding of the Combustion Institute, 20: 287-294.

Ishizuka, S. (1989). "An Experimental Study on Extinction and Stability of Tubular Flames." Combustion and Flame 75: 367-379.

Ishizuka, S. (1993). "Characteristics of Tubular Flames." Progress in Energy and Combustion Science 19: 187-226.

Ishizuka, S. and Y. Sakai (1986). Structure and Tip-Opening of Laminar Diffusion Flames. Proceedings of the Combustion Institute, 21: 1821-1828.

Ishizuka, S. and H. Tsuji (1981). An Experimental Study of Effect of Inert Gases on Extinction of Laminar Diffusion Flames. Proceedings of the Combustion Institute, 18: 695-703.

Jacono, D. L., P. Papas and P. A. Monkewitz (2003). "Cell Formation in Non-Premixed, Axisymmetric Jet Flames near Extinction." Combustion Theory and Modelling 7(4): 635-644.

Jacono, D. L. and P. A. Monkewitz (2007). " Scaling of Cell Size in Cellular Instabilities of Nonpremixed Jet Flames." Combustion and Flame 151: 321-332.

Ju, Y., H. Matsumi, K. Takita and G. Masuya (1998). "Combined Effects of Radiation, Flame Curvature, and Stretch on the Extinction and Bifurcations of Cylindrical Ch4/Air Premixed Flame." Combustion and Flame 116: 580-592.

Kaiser, C., J.-B. Liu and P. D. Ronney (2000). Diffusive-Thermal Instability of Counterflow Flames at Low Lewis Number. 38th Aerospace Sciences Meeting and Exhibit: AIAA-2000-0576, Reno, NV.

Katta, V. R., Meyer, T. R., Gord, J. R. and Roquemore, W. M. (2003). " Insights into Non-Adiabatic-Equilibrium Flame Temperatures During Millimeter-Size Vortex/Flame Interactions". Combustion and Flame 132: 639-651.

Katta, V. R., C. D. Carter, G. J. Fiechtner, W. M. Roquemore, J. R. Gord and J. C. Rolon (1998). Interaction of a Vortex with a Flat Flame Formed between Opposing Jets of Hydrogen and Air. Proceedings of the Combustion Institute, 27: 587-594.

Katta, V. R., L. P. Goss and W. M. Roquemore (1994). "Effect of Nonunity Lewis Number and Finite-Rate Chemistry on the Dynamics of a Hydrogen-Air Jet Diffusion Flame." Combustion and Flame 96: 60-74.

Katta, V. R., S. Hu, P. Wang, R. W. Pitz and W. M. Roquemore (2007). Investigations on Double-State Behavior of Counterflow Premixed Flame System. Proceedings of the Combustion Institute, 31: 1055-1066, Heidelberg, Germany.

Katta, V. R. and W. M. Roquemore (1995). "On the Structure of a Stretched/Compressed Laminar Flamelet - Influence of Preferential Diffusion." Combustion and Flame 100: 61-70.

Kee, R. J., J. F. Grcar, M. D. Smooke and J. A. Miller (1985). Sandia Report 85-8240, Sandia National Laboratories.

Kim, H. J., S. M. Kang, Y. M. Kim, J. H. Lee and J. K. Lee (2006). "Transient Flamelet Modeling for Combustion Processes of Hsdi Diesel Engines." International Journal of Automotive Technology 7(2): 129-137.

Kim, J. S. (1997). "Linear Analysis of Diffusioinal-Thermal Instability in Diffusion Flames with Lewis Numbers Close to Unity." Combustion Theory and Modelling 1(1): 13-40.

Kim, J. S. and S. R. Lee (1999). "Diffusional-Thermal Instability in Strained Diffusion Flames with Unequal Lewis Numbers." Combustion Theory and Modelling 3(1): 123-146.

Kim, J. S. and F. A. Williams (1997). "Extinction of Diffusion Flames with Nonunity Lewis Numbers." Journal of Engineering Mathematics 31: 101-118.

Kim, J. S., F. A. Williams and P. D. Ronney (1996). "Diffusional-Thermal Instability of Diffusion Flames." Journal of Fluid Mechanics 327: 273-301.

Kitano, M., H. Kobayashi and Y. Otsuka (1989). "A Study of Cylindrical Premixed Flames with Heat Loss." Combustion and Flame 76: 89-105.

Kobayashi, H. and M. Kitano (1989). "Extinction Charateristecs of a Stretched Cylindrical Premixed Flame." Combustion and Flame 76: 285-295.

Kobayashi, H. and M. Kitano (1991). "Flow Fields and Extinction of Stretched Cylindrical Premixed Flames." Combustion Science and Technology 75: 227-239.

Kobayashi, H. and M. Kitano (1993). "Effects of Equivalence Ratio on the Extinction Stretch Rate of Cylindrical Premixed Flames." Combustion Science and Technology 89: 253-263.

Kojima, J. and Q. V. Nguyen (2002). "Laser Pulse-Stretching with Multiple Optical Ring Cavities." Applied Optics 41(30): 6360-6370.

Kortschik, C., S. Honnet and N. Peters (2005). "Influence of Curvature on the Onset of Autoignition in a Corrugated Counterflow Mixing Field." Combustion and Flame 142: 140-152.

Krishnamurthy, L., F. A. Williams and K. Seshadri (1976). "Asymptotic Theory of Diffusion-Flame Extinction in Stagnation-Point Boundary-Layer." COMBUSTION AND FLAME 26: 363-377.

Law, C. K. (1988a). Dynamics of Stretched Flames. Proceedings of the Combustion Institute, 22: 1381-1402.

Law, C. K. (1988b). Extinction of Couterflow Diffusion Flames with Branching-Termination Chain Mechanisms: Theory and Experiment. Mathematical Modeling in Combustion Science. J. D. Buckmaster and T. Takeno. New York, Springer-Verlag: 147.

Law, C. K. and S. H. Chung (1982). "Steady State Diffusion Flame Structure with Lewis Number Variations." Combustion Science and Technology 29: 129-145.

Lee, J. C., C. E. Frouzakis and K. Boulouchos (2000). "Numerical Study of Opposed-Jet H2/Air Diffusion Flame - Vortex Interactions." Combustion Science and Technology 158: 365-388.

Lee, S. R. and J. S. Kim (2000). "Nonlinear Dynamic Characteristics of Flame Stripes Formed in Strained Diffusion Flames by Diffusional-Thermal Instability." Combustion Theory and Modelling 4(1): 29-46.

Lee, S. R. and J. S. Kim (2002). "On the Sublimit Solution Branches of the Stripe Patterns Formed in Counterflow Diffusion Flames by Diffusional-Thermal Instability." Combustion Theory and Modelling 6(2): 263-278.

Li, J., Z. Zhao, A. Kazakov and F. L. Dryer (2003). An Updated Comprehensive Kinetic Model for H2 Combustion. Fall Technical Meeting of the Eastern States Section

of the Combustion Institute, Penn State University, University Park, PA.

Libby, P. A., N. Peters and F. A. Williams (1989). "Cylindrical Premixed Laminar Flames." Combustion and Flame 75: 265-280.

Liñán, A. (1974). "The Asymptotic Structure of Counterflow Diffusion Flames for Large Activation Energies." Acta Astronautica 1: 1007-1039.

Marracino, B. and D. Lentini (1997). "Radiation Modelling in Non-Luminous Nonpremixed Turbulent Flames." Combustion Science and Technology 128: 23-48.

Maruta, K., M. Yoshida, H. Guo, Y. Ju and T. Niioka (1998). "Extinction of Low-Stretched Diffusion Flames in Microgravity." Combustion and Flame 112: 181-187.

Matalon, M. (2007). "Intrinsic Flame Instabilities in Premixed and Nonpremixed Combustion." Annual Revew of Fluid Mechanics 39: 163-191.

Metzener, P. and M. Matalon (2006). "Diffusive-Thermal Instabilities of Diffusion Flames: Onset of Cells and Oscillations." Combustion Theory and Modelling 10(4): 701-725.

Meyer, T. R., G. J. Fiechtner, S. P. Gogineni, J. C. Rolon, C. D. Carter and J. R. Gord (2004). "Simultaneous Plif/Piv Investigation of Vortex-Induced Annular Extinction in H2-Air Counterflow Diffusion Flames." Experiments in Fluids 36: 259-267.

Mikolaitis, D. W. (1984a). "The Interation of Flame Curvature and Stretch, Part 1: The Concave Premixed Flame." Combustion and Flame 57: 25-31.

Mikolaitis, D. W. (1984b). "The Interation of Flame Curvature and Stretch, Part 2: The Convex Premixed Flame." Combustion and Flame 58: 23-29.

Morel, T. (1975). "Comprehensive Design of Axisymmetric Wind Tunnel Contractions." Journal of Fluids Engineering 97(2): 225-233.

Mosbacher, D. M., J. A. Wehrmeyer, R. W. Pitz, C. J. Sung and J. L. Byrd (2002). Experimental and Numerical Investigation of Premixed Tubular Flames. Proceedings of the Combustion Institute, 29: 1479-1486.

Mueller, M. A., T. J. Kim, R. A. Yetter and F. L. Dryer (1999). "Flow Reactor Studies and

Kinetic Modeling of the H-2/O-2 Reaction." International Journal of Chemical Kinetics 31(2): 113-125.

Nandula, S. P. (2003). Lean Premixed Flame Structure under Intense Turbulence: Rayleigh/Raman/Lif Measurements and Modeling. Department of Mechanical Engineering. Nashville, TN, Vanderbilt University. Ph.D.

Nishioka, M., K. Inagaki, S. Ishizuka and T. Takeno (1991). "Effects of Pressure on Structure and Extinction of Tubular Flame." Combustion and Flame 86(1-2): 90-100.

Nishioka, M. and T. Takeno (1988). "Effects of Variable Density on a Tubular Flame." Combustion and Flame 73: 287-301.

Norton, T. S., K. C. Smyth, J. H. Miller and M. D. Smooke (1993). "Comparison of Experimental and Computed Species Concentration and Temperature Profiles in Laminar, Two-Dimensional Methane/Air Diffusion Flames." Combustion Science and Technology 90: 1-34.

Ogawa, Y., N. Saito and C. Liao (1998). Burner Diameter and Flammability Limit Measured by Tubular Flame Burner. Proceedings of the Combustion Institute, 27: 3221–3227.

Osborne, R. J., J. A. Wehrmeyer and R. W. Pitz (2000). A Comparison of Uv Raman and Visible Raman Techniques for Measuring Non-Sooting Partially Premixed Hydrocarbon Flames. 38th AIAA Aerospace Sciences Meeting and Exhibit, AIAA-2000-0776, Reno, NV.

Papas, P., R. M. Rais, P. A. Monkewitz and A. G. Tomboulides (2003). "Instabilities of Diffusion Flames near Extinction." Combustion Theory and Modelling 7(4): 603-633.

Paul, P. H. (1994). "A Model for Temprature-Dependent Collisional Quenching of Oh A2 $\sum$ +." Journal of Quantitative Spectroscopy and Radiative Transfer 51(3): 511-524.

Pellett, G. L., K. M. Isaac, W. M. Humphreys, L. R. Gartrell, W. L. Roberts, C. L. Dancey and G. B. Northam (1998). "Velocity and Thermal Structure, and Strain-Induced Extinction of 14 to 100% Hydrogen-Air Counterflow Diffusion Flames." Combustion and Flame 112: 575-592.

Peters, N. (1984). "Laminar Diffusion Flamelet Models in Non-Premixed Turbulent Combustion." Progress in Energy and Combustion Science 10(3): 319-339.

Peters, N. and B. Rogg (1993). Reduced Kinetic Mechanisms for Applications in Combustion Systems, Berlin, Springer-Verlag.

Pitsch, H. (2000). "Unsteady Flamelet Modeling of Differential Diffusion in Turbulent Jet Diffusion Flames." Combustion and Flame 123(3): 358-374.

Pitsch, H., C. M. Cha and S. Fedotov (2003). "Flamelet Modelling of Non-Premixed Turbulent Combustion with Local Extinction and Re-Ignition." Combustion Theory and Modelling 7(2): 317-332.

Pitsch, H. and N. Peters (1998). "A Consistent Flamelet Formulation for Non-Premixed Combustion Considering Differential Diffusion Effects." Combustion and Flame 114(1-2): 26-40.

Pitsch, H., E. Riesmeier and N. Peters (2000). "Unsteady Flamelet Modeling of Soot Formation in Turbulent Diffusion Flames." Combustion Science and Technology 158: 389-406.

Potter Jr., A. E., Buttler, J. N. (1959). "A Novel Combustion Measurements Based on the Extinguishment of Diffusion Flames". ARS Journal 29: 54-56.

Poinsot, T. and D. Veynante (2001). Theoretical and Numerical Combustion, R.T. Edwards, Inc.

Puri, I. K. and K. Seshadri (1986). "Extinction of Diffusion Flames Burning Diluted Methane and Diluted Propane in Diluted Air." Combustion and Flame 65: 137-150.

Qian, J. and C. K. Law (1997). "On the Spreading of Unsteady Cylindrical Diffusion Flames." Combustion and Flame 110(1-2): 152-162.

Riechelmann, D., T. Fujimori and J. Sato (2002). "Effect of Dilution on Extinction of Methane Diffusion Flame in High Temperature Air up to 1500 K." Combustion Science and Technology 174: 23-46.

Riesmeier, E., S. Honnet and N. Peters (2004). "Flamelet Modeling of Pollutant Formation in a Gas Turbine Combustion Chamber Using Detailed Chemistry for a Kerosene Model Fuel." Journal of Engineering for Gas Turbines and

Power-Transactions of the ASME 126(4): 899-905.

Rolon, J. C., F. Aguerre and S. Candel (1995). "Experiments on the Interaction between a Vortex and a Strained Diffusion Flame." Combustion and Flame 100: 422-429.

Sakai, Y. and S. Ishizuka (1991). "Structure of Tubular Flames: Structures of the Tubular Flames of Lean Methane/Air Mixtures in Rotating Stretched Flow Field." JSME International Journal 34: 234-241.

Sanders, J. P. H., J. Y. Chen and I. Gökalp (2000). "Flamelet-Based Modeling of No Formation in Turbulent Hydrogen Jet Diffusion Flames." combustion and Flame 111: 1-15.

Sanders, J. P. H. and A. P. G. G. Lamers (1994). "Modeling and Calculation of Turbulent Lifted Diffusion Flames." Combustion and Flame 96(1-2): 22-33.

Santoro, V. S. and A. Gomez (2002). Extinction and Reignition in Counterflow Spray Diffusion Flames Interacting with Laminar Vortices. Proceedings of the Combustion Institute, 29: 585-592.

Sato, J. (1991). "Extinction of Counterflow Diffusion Flame in High Pressures." Combustion Science and Technology 75: 103-133.

Seshadri, K., I. Puri and N. Peters (1985). "Experimental and Theoretical Investigation of Partially Premixed Diffusion Flames at Extinction." Combustion and Flame 61: 237-249.

Seshadri, K., C. Trevino and M. D. Smooke (1989). "Analysis of the Structure and Mechanisms of Extinction of a Counterflow Methanol-Air Diffusion Flame." Combustion and Flame 76: 111-132.

Seshadri, K. and F. A. Williams (1978). "Laminar Flow between Parallel Plates with Injection of a Reactant at High Reynolds Number." Int. J. Heat Mass Transfer 21: 251-253.

Simmons, R. F. and Wolfhard, H. G. (1957). "Some Limiting Oxygen Concentrations for Diffusion Flames in Air Diluted with Nitrogen," Combustion and Flame 1: 155-161.

Smith, G. P., D. M. Golden, M. Frenklach, N. W. Moriarty, B. Eiteneer, M. Goldenberg, C. T. Bowman, R. K. Hanson, S. Song, W. C. G. Jr., V. V. Lissianski and Z. Qin

(2000). http://www.me.Berkeley.edu/gri_mech/, Gas Research Institute, Chicago, Illinois.

Smooke, M. D. and V. Giovangigli (1990). Extinction of Tubular Premixed Laminar Flames with Complex Chemistry. 23rd Symposium (International) on Combustion: 447-454.

Smooke, M. D., P. Lin, J. K. Lam and M. B. Long (1990). Computational and Experimental Study of a Laminar Axisymmetric Methane-Air Diffusion Flame. 23rd Symposium (International) on Combustion: 575-582.

Sohrab, S. H., A. Liñán and F. A. Williams (1982). "Asymptotic Theory of Diffusion-Flame Extinction with Radiant Loss from the Flame Zone." Combustion Science and Technology 27: 143-154.

Spalding, D. B. (1953). "The Combustion of Liquid Fuels." Proceeding of the Combustion Institute 4: 847-864.

Spalding, D. B. (1954). "A Theory of Extinction of Diffusion Flames." Fuel 33: 255-273.

Sung, C. J., J. B. Liu and C. K. Law (1995). "Structural Response of Counterflow Diffusion Flames to Strain Rate Variations." Combustion and Flame 102: 481-492.

Takagi, T. and Z. Xu (1994). "Numerical Analysis of Laminar Diffusion Flames - Effects of Preferential Diffusion of Heat and Species". Combustion and Flame 96: 50-59

Takagi, T. and Z. Xu (1996). "Numerical Analysis of Laminar Diffusion Flames - Effects of Preferential Diffusion of Heat and Species." Combustion and Flame 96: 50-59.

Takagi, T., Z. Xu and M. Komiyama (1996a). "Preferential Diffusion Effects on the Temperature in Usual and Inverse Diffusion Flames." Combustion and Flame 106: 252-260.

Takagi, T., Y. Yoshikawa, K. Yoshida, M. Komiyama and S. Kinoshita (1996b). Studies on Strained Non-Premixed Flames Affected by Flame Curvature and Preferential Diffusion. Proceedings of the Combustion Institute, 26: 1103-1110.

Takeno, T., M. Nishioka and S. Ishizuka (1986). "A Theorectical Study of Extinction of a Tubular Flame." Combustion and Flame 66: 271-283.

Thevenin, D., P. H. Renard, G. J. Fiechtner, J. R. Gord and J. C. Rolon (2000). Regimes

of Non-Premixed Flame-Vortex Interactions, 28: 2101-2108.

Trees, D., T. M. Brown, K. Seshadri, M. D. Smooke, G. Balakrishnan, R. W. Pitz, V. Giovangigli and S. P. Nandula (1995). "The Structure of Nonpremixed Hydrogen-Air Flames." Combustion Science and Technology 104: 427-439.

Tsien, H. S. (1943). "On the Design of a Contraction Cone for Wind Tunnel." Journal of the Aeronautical Sciences 10: 68-70.

Tsuji, H. (1982). "Counterflow Diffusion Flames." Progress in Energy and Combustion Science 8: 93-119.

Tsuji, H. and I. Yamaoka (1966). The Counterflow Diffusion Flame in the Forward Stagnation Region of a Porous Cylinder. Proceedings of the Combustion Institute, 11: 979-984, Berkeley.

Tsuji, H. and I. Yamaoka (1967). The Counterflow Diffusion Flame in the Forward Stagnation Region of a Porous Cylinder. Proceedings of the Combustion Institute, 11: 979-984, Berkeley.

Tsuji, H. and I. Yamaoka (1969). The Structure of Counterflow Diffusion Flames in the Forward Stagnation Region of a Porous Cylinder. Proceedings of the Combustion Institute, 12: 997-1005.

Tsuji, H. and I. Yamaoka (1971). Structure Analysis of Counterflow Diffusion Flames in the Forward Stagnation Region of a Porous Cylinder. 13th Symposium (International) on Combustion: 723-731.

Tsuji, H. and I. Yamaoka (1982). Structure and Extinction of near-Limit Flames in a Stagnation Flow. 19th Symposium (International) on Combustion: 1533-1540.

Wang, H. F. and Y. L. Chen (2005). "Steady Flamelet Modelling of a Turbulent Non-Premixed Flame Considering Scalar Dissipation Rate Fluctuations." Fluid Dynamics Research 37(3): 133-153.

Wang, P., S. Hu and R. W. Pitz (2006a). Numerical Investigation of the Curvature Effects on Diffusion Flames. 44th AIAA Aerospace Sciences Meeting and Exhibit: AIAA-2006-0159, Reno, NV.

Wang, P., S. Hu and R. W. Pitz (2007). Numerical Investigation of the Curvature Effects on Diffusion Flames. Proceedings of the Combustion Institute, 31: 989-996, Hei-

delberg, Germany.

Wang, P., J. A. Wehrmeyer and R. W. Pitz (2006b). "Stretch Rate of Tubular Premixed Flames." Combustion and Flame 145: 401-414.

Wehrmeyer, J. A., S. Yeralan and K. S. Tecu (1996). "Influence of Strain Rate and Fuel Dilution on Laminar Nonpremixed Hydrogen-Air Flame Structure: An Experimental Investigation." Combustion and Flame 107: 125-140.

Williams, F. A. (1981). "A Review of Flame Extinction." Fire Safety Journal 3: 163-175.

Williams, F. A. (1985). Combustion Theory. 2nd ed., Redwood City, CA, Addison-Wesley.

Williams, F. A. (2000). "Progress in Knowledge of Flamelet Structure and Extinction." Progress in Energy and Combustion Science 26: 657-682.

Yamamoto, K., T. Hirano and S. Ishizuka (1996). Effects of Pressure Diffusion on the Characteristics of Tubular Flames. 26th Symposium (International) on Combustion: 1129-1135.

Yamamoto, K., S. Ishizuka and T. Hirano (1994). Effects of Rotation on the Stability and Structure of Tubular Flame. 25th Symposium (International) on Combustion: 1399-1406.

Yamaoka, I. and H. Tsuji (1977). Structure Analysis of Rich Fuel-Air Flames in the Forward Stagnation Region of a Porous Cylinder. 16th Symposium (International) on Combustion: 1145-1154.

Yetter, R. A., F. L. Dryer and H. Rabitz (1991). "A Comprehensive Reaction-Mechanism for Carbon-Monoxide Hydrogen Oxygen Kinetics." Combustion Science and Technology 79(1-3): 97-128.

Yoshida, K. and T. Takagi (1998). Transient Local Extinction and Reignition Behavior of Diffusion Flames Affected by Flame Curvature and Preferential Diffusion. Proceedings of the Combustion Institute, 27: 685-692.

Yoshida, K. and T. Takagi (2003). "Structural Studies of Locally Strained Diffusion Flames." JSME International Journal 46(1): 190-197.